UNIVERSITÀ DEGLI STUDI DI PADOVA

Department of Agronomy, Food, Natural resources, Animals and Environment

Department of Land, Environment, Agriculture and Forestry

Second cycle degree in

SUSTAINABLE AGRICULTURE

El Niño Impact on Agriculture in the Chorotega region of Costa Rica

Supervisor: *Prof. Paolo Tarolli*

Co-supervisors: *Dott. Junliang Qiu;*

Prof. Ana María Durán-Quesada

Student:

Irene Dell'Olio

Student ID: 124248

ACCADEMIC YEAR: 2021/2022

Index

Abstract

El Niño-Southern Oscillation (ENSO) is the main driver of the interannual variability of drought affecting the Chorotega region in Costa Rica facing the Pacific Ocean waters. It is a periodic alteration of Pacific Ocean surface temperature close to equatorial longitudes, which consists in an anomalous increase or diminution of Sea Surface Temperatures (SST) above or below average for a prolonged period, causing important changes in global patterns of climatic variables. Its warm phase "El Niño" is known to cause severe drought conditions in the with severe impact on natural resources, human health, water availability and more than any other fields, impact negatively agriculture which is one of the main economic activities in the region. This study aims to evaluate the impacts of the last two strongest El Niño events on agriculture with the help of remote sensing data from Landsat from 1990 to 2021, and modern cloud computing platforms such as Google Earth Engine. These technologies allow us to develop an improved outlook of historical patterns of key parameters correlated with ENSO. Landsat collection dataset was used to analyse the Normalized Difference Vegetation Index (NDVI) trends in the region from 1990 to 2021 and its response in cropland area after strongest El Niño events of the last 30 years, which happened in 1997-1998 and 2015-2016. Previous studies have widely investigated El Niño event and its impact in the Chorotega region, but analysis of the impact on agriculture through a long time NDVI change in cropland area to understand continuous effects of El Niño have not been reported in literature. Results showed that cropland area for both events was negatively affected during El Niño events, and that 2015-2016 event had more severe impact on agriculture than the 1997-1998 event. The two events had different temporal development and intensity, also the severity in which they hit the region is different, underlying the unpredictability of El Niño at the local scale. It is crucial to have a better understanding of the impact of this phenomenon on agriculture, leveraging current knowledge of past events is key to better identify most affected areas, specific impacts, and find solutions to support resilience and adaptation. Albeit national environmental protection policies to improve resilience exists, more specific interventions for agriculture and water resources management, based on scientific evidence, are needed to advance the response to upcoming events.

Riassunto

El Niño-Southern Oscillation (ENSO) è il principale responsabile della variabilità interannuale della siccità che colpisce la regione Chorotega in Costa Rica, affacciata sull'Oceano Pacifico. Si tratta di un'alterazione periodica della temperatura superficiale dell'Oceano Pacifico vicino alle longitudini equatoriali, che consiste in un aumento o in una diminuzione anomala delle temperature della superficie del mare (SST) al di sopra o al di sotto della media per un periodo prolungato, causando importanti cambiamenti negli andamenti globali delle variabili climatiche. La sua fase calda, "El Niño", è nota per causare gravi condizioni di siccità nella regione, con un forte impatto sulle risorse naturali, sulla salute umana, sulla disponibilità di acqua e, più di ogni altro campo, sull'agricoltura, che è una delle principali attività economiche della regione. Questo studio si propone di valutare l'impatto degli ultimi due eventi El Niño più forti sull'agricoltura con l'aiuto di dati di telerilevamento presi dalla raccolta Landsat dal 1990 al 2021 e di moderne piattaforme di cloud computing come Google Earth Engine. Queste tecnologie ci permettono di sviluppare una migliore visione dei modelli storici dei parametri chiave correlati all'ENSO. Il set di dati della raccolta Landsat è stato utilizzato per analizzare le tendenze dell'indice di vegetazione normalizzato (NDVI) nella regione dal 1990 al 2021 e la sua risposta nelle aree coltivate dopo gli eventi El Niño più forti degli ultimi 30 anni, verificatisi nel 1997-1998 e nel 2015-2016. Studi precedenti hanno ampiamente analizzato l'evento El Niño e il suo impatto nella regione di Chorotega, ma non è stata riportata in letteratura un'analisi dell'impatto sull'agricoltura attraverso la variazione dell'NDVI nel lungo periodo nelle aree coltivate per comprendere gli effetti continui di El Niño. I risultati hanno mostrato che l'area coltivata per entrambi gli eventi è stata colpita negativamente da El Niño, e che l'evento 2015-2016 ha avuto un impatto più grave rispetto a quello del 1997-1998. I due eventi hanno avuto uno sviluppo temporale e un'intensità diversi, anche la gravità con cui hanno colpito la regione è diversa, evidenziando l'imprevedibilità di El Niño a scala locale. È fondamentale avere una migliore comprensione dell'impatto di questo fenomeno sull'agricoltura, sfruttando le conoscenze attuali degli eventi passati per identificare meglio le aree più colpite, gli impatti specifici e trovare soluzioni per sostenere la resilienza e l'adattamento. Sebbene esistano politiche nazionali di protezione ambientale per migliorare la resilienza, sono necessari interventi più specifici per l'agricoltura e la gestione delle risorse idriche, basati su evidenze scientifiche, per migliorare la risposta ai prossimi eventi.

1. Introduction

The El Niño-Southern Oscillation (ENSO) is the most relevant climate variability mode and one of the most broadly studied climatic phenomenon because its impact on global climate, particularly its effect on changes in precipitation patterns worldwide (Slyunyaev et al., 2021; Yang et al., 2018). ENSO is divided in an oceanic component (El Niño) and an atmospheric component (Southern Oscillation) (McGregor & Ebi, 2018). The oceanic component consists of an anomalous change in Sea Surface Temperature (SST) in the central and eastern tropical Pacific, with two opposite events which often but not always are consecutive, El Niño, also referred to as "warm event" because of the positive SST anomalies and the opposite "cool event" is called La Niña and it is characterized by negative SST anomalies (Hoell & Funk, 2013; McGregor & Ebi, 2018; Yang et al., 2018).

Length, entity, and characteristics of SST anomalies are driven by a wide range of climatic factors and depend on their location and the month in which they occur. ENSO plays a relevant role in determining the interannual SST pattern near the equator, changes in the the Mixed Layer Depth (MLD) cycles are also modulated in the process in which ENSO develops (P. Q. Huang et al., 2018; Slyunyaev et al., 2021). MLD is the thickness of the upper-ocean Mixed Layer (ML) which by the alteration of its components (temperature, salinity, and density) caused by processes like wind, turbulence and waves, couples with the atmosphere weather and climate patterns (P. Q. Huang et al., 2018; Slyunyaev et al., 2021). Prolonged SST anomalies occur mainly during the boreal winter particularly in eastern and central Pacific, influencing, among others, phytoplankton bloom, cyclone formation and, climate variability (Bulgin et al., 2020). Equatorial SST anomalies related to ENSO are studied by zones (Figure 1.1) (McGregor & Ebi, 2018). Starting from the coasts of South America and moving westward, there is the El Niño 1+2 zone, characterized as the smallest area compared to the other three but the highest anomalies followed by El Niño 3 zone (Bulgin et al., 2020). El Niño 3.4 zone, placed between 5S – 5N latitudes and 120 – 170 W longitudes (around the dateline), is the most important, its anomalies are broadly used to estimate different ENSO indices because the trend of SST anomalies is more significant for this zone (Bulgin et al., 2020; McGregor & Ebi, 2018). Finally, Niño 4 region, placed in central Pacific, shows few SST anomalies than other areas and so it is not utilized in the calculation of the most famous SST anomalies indices (McGregor & Ebi, 2018).

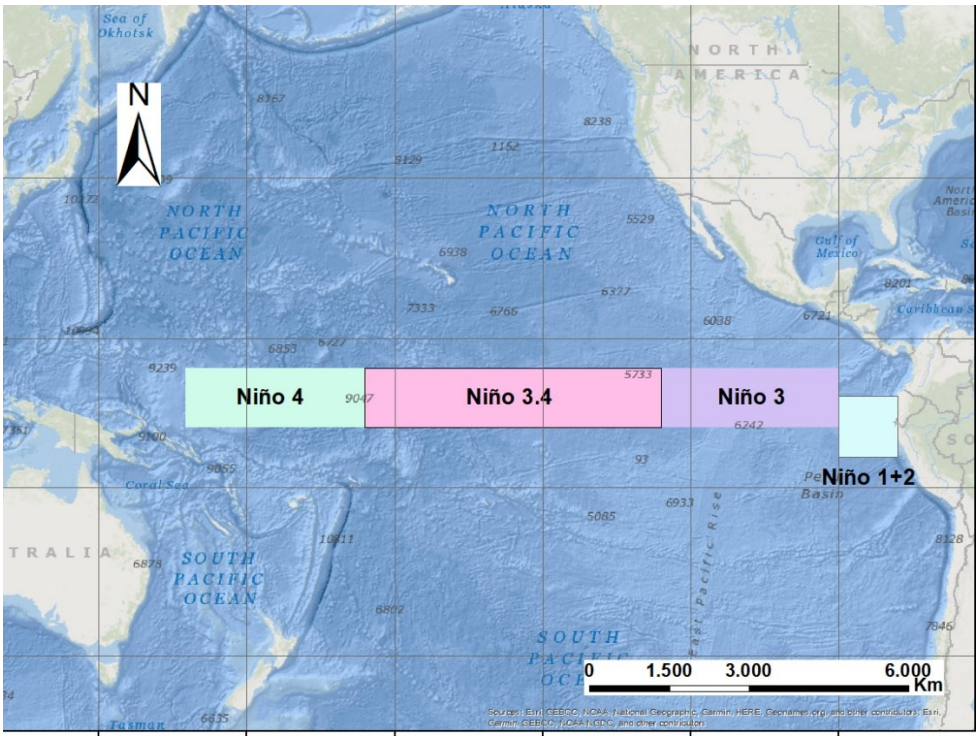

Figure 1.1. Regions in which Pacific Ocean is divided based on SST anomalies dynamic during ENSO

The Southern Oscillation component is represented by the surface atmospheric pressure "seesaw" between Eastern and Western hemispheres, or the barometric seesaw between eastern and western Pacific which determines trade winds strength (Hoell & Funk, 2013). Trade winds are weakened during El Niño, this allows the migration of warm waters towards the east (Hoell & Funk, 2013; McPhaden et al., 2020). Both El Niño and La Niña events are part of the ENSO phenomenon, which duration varies between 12 and 24 with the two events typically (but not always) succeeding one another (Hoell & Funk, 2013).

By interacting with other climatic factors and variability modes, ENSO impacts are not limited to temperatures and precipitation patterns, as it also affects the occurrence and severity of extreme events (Hoell & Funk, 2013; Yang et al., 2018). Many studies have studied changes in ENSO patterns and teleconnections over the years highlighting the non-stationary behaviour of the phenomenon contributes to forecasting uncertainty as there are no two identical ENSO events registered until now (McGregor & Ebi, 2018; Timmermann et al., 2018; Yang et al., 2018). Such large variability results from negative and positive feedbacks between the atmosphere and ocean that modulates SST anomalies, causes changes in the atmospheric deep convection and consequently on affects the Walker Circulation, upsetting normal annual temperature and precipitation patterns (Timmermann et al., 2018).

Different indices are used to study and diagnose ENSO development, the main indices developed by the National Oceanic and Atmospheric Administration (NOAA) are described as follows:

- *Southern Oscillation Index (SOI):* the index (Figure 1.2) estimates the intensity of the atmospheric component as it indicates the standardized air pressure difference between the stations of Darwin (Australia) and Tahiti (French Polynesia), located at the opposite extremes of the barometric seesaw (respectively of the Western and Eastern Hemispheres) spanning the Pacific Ocean (Hoell & Funk, 2013). La Niña is identified by strengthened trade winds caused by below average pressure in Darwin and above average pressure in Tahiti, and El Niño is characterized by below average pressure in Tahiti and above average pressure in Darwin (Hoell & Funk, 2013; McGregor & Ebi, 2018; McPhaden et al., 2020). Negative values of SOI indicate lower than normal air pressure at Tahiti while positive values indicate higher than normal air pressure values at Darwin, negative SOI values perpetuating in time reflect warmer ocean temperatures and so El Niño occurrence, opposite parameters describe La Niña conditions (Southern Oscillation Index (SOI) | El Niño/Southern Oscillation (ENSO) | National Centers for Environmental Information (NCEI) (noaa.gov)). Anomalies values are departures from 1981-2010 baseline (NOAA, https://www.ncdc.noaa.gov/teleconnections/enso/).

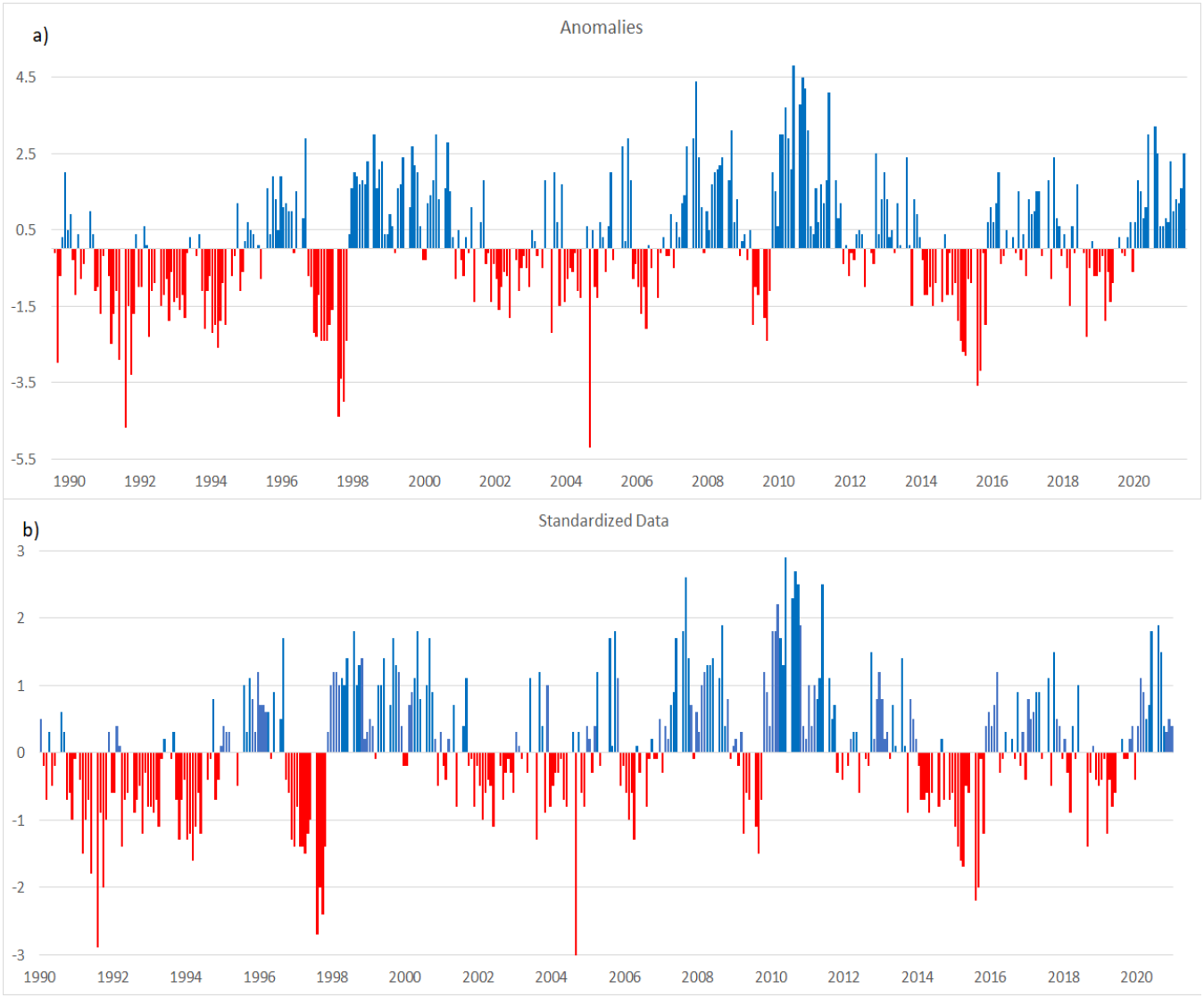

Figure 1.2. a) SOI anomalies from 1990 to 2021 expressed in hPa b) Standardized SOI values from 1990 to 2021. Data downloaded from https://www.cpc.ncep.noaa.gov/data/indices/soi

- *Equatorial Pacific Sea Surface Temperature (SST):* five consecutive 3-months running mean of sea surface temperature (SST) anomalies in the Niño 3.4 region of +0.5 °C or -0.5 °C indicates El Niño or La Niña occurrence respectively and are expressed by the Oceanic Niño Index (ONI, Figure 1.3) (McGregor & Ebi, 2018, Equatorial Pacific Sea Surface Temperatures (SST) | El Niño/Southern Oscillation (ENSO) | National Centers for Environmental Information (NCEI) (noaa.gov)).

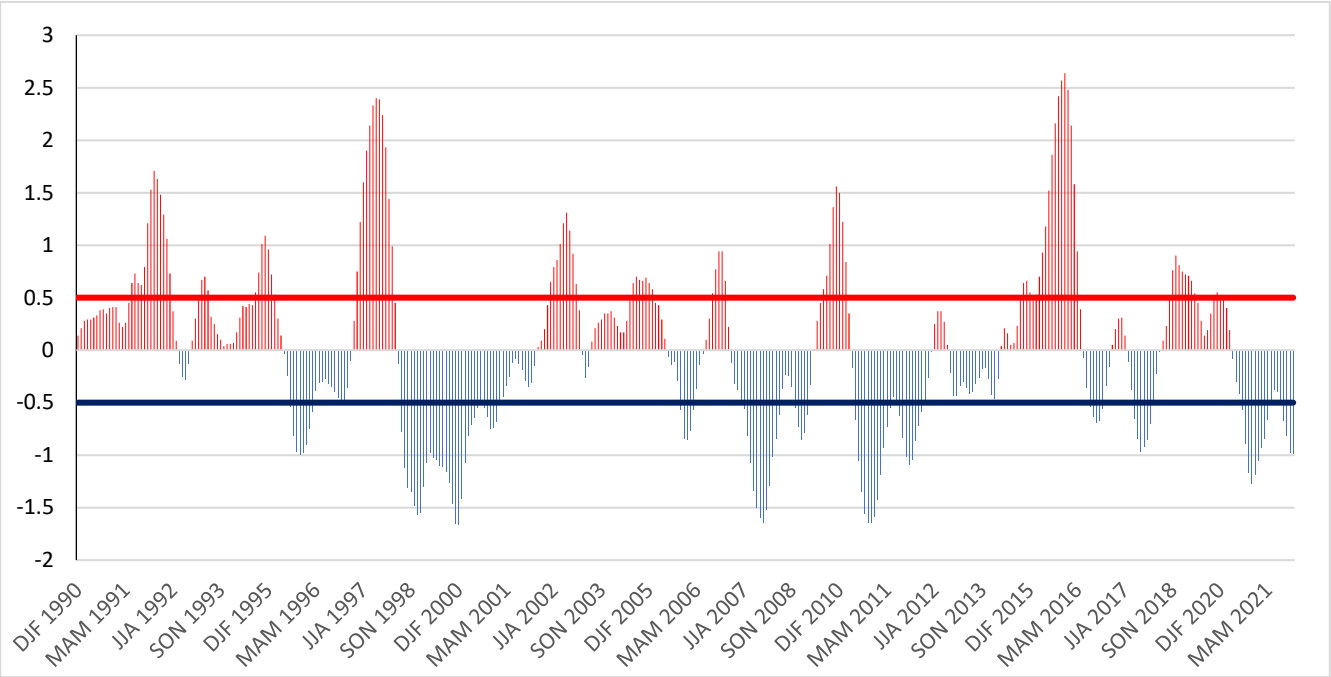

Figure 1.3. ONI Index 1990-2021. Data taken from https://www.cpc.ncep.noaa.gov/data/indices/oni.ascii.txt

- *Outgoing Longwave Radiation (OLR):* recurrent annual storms during ENSO are shifted towards east. It is possible to identify them by looking at the cloud presence with remote sensing and their emission of longwave radiations which will indicate El Niño conditions when cloud cover is higher than normal in the centre equatorial Pacific and so longwave radiations will have a lower value (colder conditions) and will indicate La Niña occurrence with opposite conditions (Figure 1.4) (McGregor & Ebi, 2018). Radiation data are taken from the Advanced Very High Resolution Radiometer (AVHRR) on the NOAA satellite and elaborated to create a standardized anomaly index (Outgoing Longwave Radiation (OLR) | El Niño/Southern Oscillation (ENSO) | National Centers for Environmental Information (NCEI) (noaa.gov)).

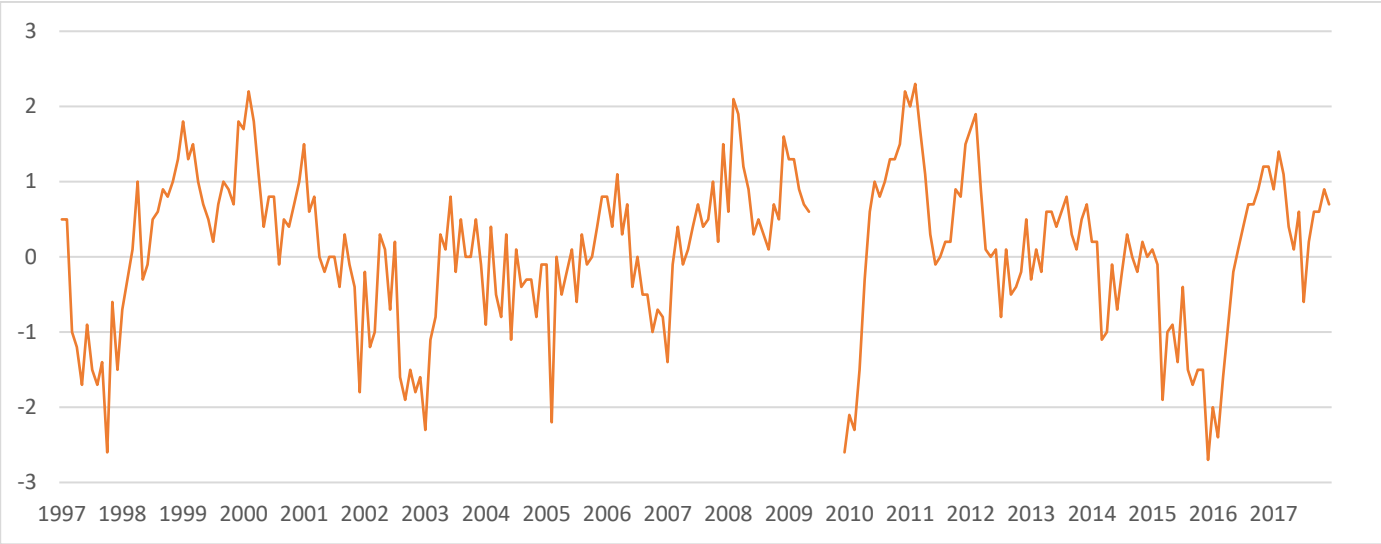

Figure 1.4. OLR Index from 1997 to 2017. Data dowloaded from https://www.cpc.ncep.noaa.gov/data/indices/olr

Several studies have tried to classify El Niño by using different indices, however, it does not exist an event equal to another one and variables affecting the phenomenon are numerous (Hoell & Funk, 2013; Wen et al., 2020; Yu & Kim, 2013). The conventional and best known one is called Eastern Pacific (EP) El Niño characterized by a significant warming of the eastern part of the Pacific Ocean, (Niño 3 region), the most intense El Niño events and weak La Niña belong to this type (Cai et al., 2018; Hoell & Funk, 2013). The warming or cooling of most of the central equatorial part close to the Date Line is called El Niño Modoki, (also known as the dateline El Niño, Central Pacific (CP) El Niño, or Warm Pool El Niño), normally creating strong to moderate La Niña ad moderate El Niño, this type appears to be the more recurrent in the last years(Cai et al., 2018; Hoell & Funk, 2013; Wen et al., 2020; Yu & Kim, 2013). Finally, the Mixed-Type Pacific (MP) El Niño shows intermediate characteristics between the two mentioned above (Wen et al., 2020; Yu & Kim, 2013). Other attempts to classify El Niño include Kane (1999) work that categorized El Niños according to the positive SST anomalies along the Peruvian and Ecuadorian coasts as strong (SST anomalies > 3°C), moderate (2°C < SST anomalies < 3°C) and weak (1°C < SST anomalies < 2°C).

It has been determined that the impact of ENSO is proportional to the intensity of the event.

Strong EP El Niño causes flooding in southeast USA, northeast Peru and Ecuador and droughts in west Pacific coasts. It also impacts the oceans as the typical warming of the Humboldt current during El Niño causes also the death of plankton and fishes near the coast and coral bleaching (Cai et al., 2018; Kane, 1999). In India, severe droughts and less frequently higher than normal rainfalls are associated with El Niño, independently by its strength, also south-eastern Australian droughts over the years showed a correlation with the event (Kane, 1999). In California, strong El Niño events are linked to high precipitations spreading all over the state, as weaker

events only affect the southern California (Hoell et al., 2016). The 1997-98 event was very strong, the increase of precipitation in California even provide the conditions for the desert areas to bloom, heavy rainfall and floods affected Arizona, and wetter than normal conditions during winter and spring were observed in the northeast of the US and Florida (Adams et al., 1999; Kane, 1999). Effects on East Asian precipitation were variable and relative to the type of El Niño, for EP El Niño dried than normal conditions were observed in North China and wetter than normal condition in Southeast China, the MP El Niño was linked to heavy rainfall in the Yangtze-Huaihe River valley and reduced rainfalls over South and North China, while CP El Niño caused wetter than normal conditions in South and North China and drought in the Jianghuai region (Wen et al., 2020).

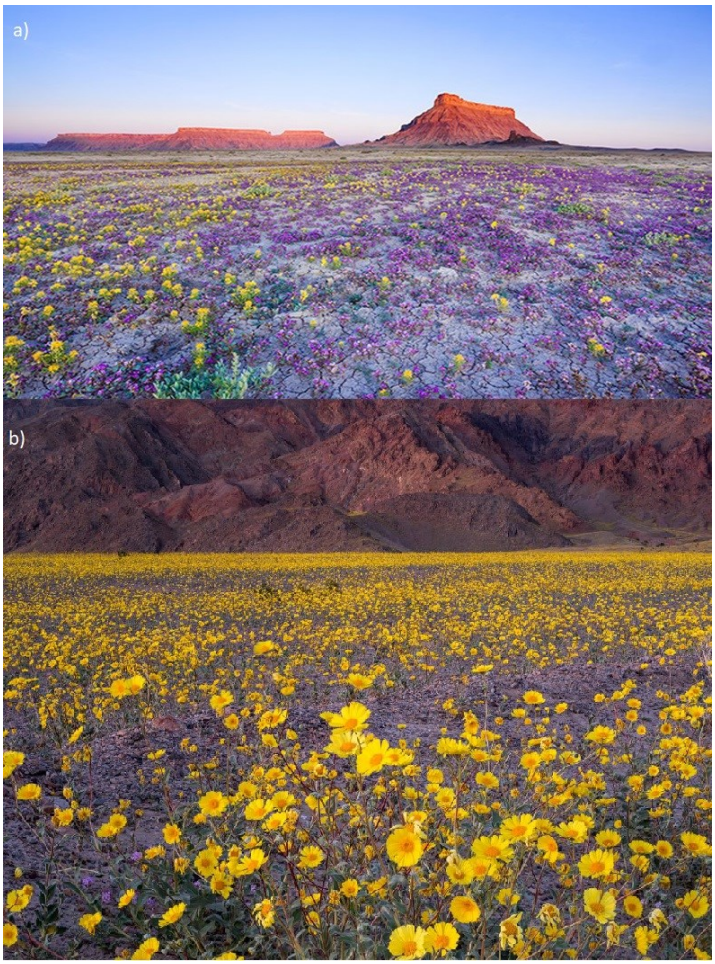

Figure 1.5. Desert flowering after El Niño event of 2015-2016. a) Flowers bloom in Chile's Atacama Desert (photo downloaded from: https://www.telesurenglish.net/multimedia/Flowers-Bloom-in-Chiles-Atacama-Desert-20151102-0017.html); b) Flowers bloom in California's Death Valley (photo of Jack Dykinga downloaded from: https://en.protothema.gr/death-valley-is-alive-again-pics/)

Strong El Niño play a role in cooling winters in Europe, especially in the Northeast (e.g., 1940-41-42) as it interacts with other variability modes, such as the NAO (North Atlantic Oscillation) for which El Niño induced negative conditions tends to increase precipitation in the northern Mediterranean and decrease precipitation in Scandinavia (Brönnimann, 2007). More recent studies (Hoell & Funk, 2013) have shown that repercussions in

Europe are more likely to be related to La Niña event. The El Niño 1997-1998 event caused higher than normal precipitation on Christmas Island, Australia and India, drought conditions which enhanced wildfires conditions were observed in southern Peru, western Bolivia, North East Brazil, Amazonia and Roraima, Micronesia, Thailand, Vietnam, Malaysia, Indonesia, Western Fiji, Philippines and West Papua New Guinea, floods and heavy rains were recorded in eastern and northern Peru, eastern Bolivia, South Brazil, Paraguay, Uruguay, North East Argentina, Chile and Ecuador (Kane, 1999). The recent 2015-2016 event caused wildfires in Indonesia with the consequent haze hazard in the surrounding regions, extreme floods in Peru, the flowering of Atacama Desert in Chile and of Death Valley in California (Figure 1.5), coral bleaching, health issues, and other disasters similar to impacts recorded during 1997-1998 event in many areas of the Pacific (McGregor & Ebi, 2018). Tropical pacific regions often suffer precipitation deficit and irregularity during El Niño, and independently from the season in which the event occurs, dry season tend to last more and wet season to be shorter (Lyon, 2004; J. Retana et al., 1999). Our study region is located in the Central America and during ENSO event its Pacific side shows almost opposite climatic conditions compared to the Atlantic regions (Lyon, 2004; V. O. Magaña et al., 2003).

As mentioned, the impact of ENSO and associated influence on extreme precipitation and temperature extends to affectations on human health, water resources, forestry, ecosystems, and agriculture. Health conditions are proven to be affected by the phenomenon as the spread and/or intensity of many diseases are directly correlated with humidity or temperature conditions, factors which typical seasonal patterns are directly altered by ENSO (McGregor & Ebi, 2018). Scientists have found evidence of this correlation mainly with diseases brought by vectors or water-borne because population fluctuations of vectors and microorganisms are highly affected by climatic conditions (Anyamba et al., 2019; J. Retana et al., 1999). Some examples of ENSO-worsened diseases were malaria in Africa, dengue and Zika around the Equator, cholera, and diarrhoea mostly in Asia and Africa (Anyamba et al., 2019). In 1993, in southeast USA, rats' population increased of ten times causing the spread of a mortal pulmonary hantavirus (Anyamba et al., 2019; McGregor & Ebi, 2018; J. Retana et al., 1999). In Costa Rica, cases of dengue increased both in the Pacific and the Caribbean, malaria increased mainly during the rainiest months in the Caribbean and, to a lesser extent in the Chorotega and Huetar Norte regions (United Nations, 1998). Diseases are also a threat for ecosystems as vectors and plagues are often opportunistic communities and adapt more rapidly to extreme climatic conditions than their natural enemies, belonging to this category of plagues are locusts and leafhoppers, mosquitos, worms and rodents (J. Retana et al., 1999). In Costa Rica, during ENOS of 1994, government spent more than $20 million to upfront a big and rapid rat invasion (J. Retana et al., 1999). In Costa Rica, warm ENSO have been found to favour conditions for on forest fires intensification, due to high temperatures and strong winds (Moraga Peralta, 2010). Altered precipitation normal

spatial and temporal patterns (Waylen et al., 1996) and anomalous high tides (Lizano, 2014) are also part of the impacts of ENSO that cause further disruptions in the region ecosystems.

In the Pacific coast of Central America, reduction of precipitation is one of the main impacts of El Niño, which results in drought conditions, inevitably affecting agriculture, both rainfed and irrigated crops, and therefore, monitoring food production in terms of yield and economic losses can be a great indicator of the magnitude and gravity of this event. J. A. Retana (1999) individuates two ways in which the agricultural sector can be affected by climatic variability by the direct impact of precipitation deficit in plant growth and therefore yield, and by indirect impact on farms and other activities of the production chain like transportation, local markets and commercialization. After the event of 1958 inhabitants of northeast Brazil left their homes after severe ENSO-induced precipitation deficit (J. A. Retana, 1999), the event of 1982-1983 caused famine in Australia and Indonesia, Peru experienced a catastrophic drought which affected more than 200000 ha of cultivated land, causing a loss for the agricultural sector of $650 million, in southern Africa losses reached one thousand million dollars (J. A. Retana, 1999). In Mexico and Central America losses were around $600 million of which $100 million in Nicaragua and Costa Rica (J. A. Retana, 1999). Adams et al., 1999 have calculated change in crop yield and prices over California after the strong 1997-98 event, consumers lost over $15 million with the increase in strawberry prices due to yield losses in spring 1998. During the same event Mexico registered losses for agriculture of around 2-billion dollars, Bolivia lost 41% of barley production, 40% of potato, 39% in corn and 34% in broad bean, Peru lost 4,7% of cultivated land (V. O. Magaña et al., 2003; J. A. Retana, 1999). After 1997-1998 ENSO event in Costa Rica, livestock production suffered because water and food had to be rationed, especially in Guanacaste and the Northern Zone, where pastures dried completely and heads of cattle died, palm and orange plantations were negatively affected (United Nations, 1998). Fisheries and pelagic species suffered the increase of SST which in December 1997 reached 4 °C above the average and caused ocean salinity alterations (United Nations, 1998). Soils started to lose water content at a dangerous rate because of the increase in air temperature from October 1997 (up to °C above the average in the Chorotega region and the Northern Zone in May and April 1998), causing important agricultural production loss in which most affected crops were basic grains, coffee, rice (usually during ENSO loses 3000 ha or more of cultivated land), beans, sugar cane, and melon (compromised because of changes in its sowing dates) and forest fires caused by traditional burning of post-harvest residuals in combination with strong winds were increased (Jiménez et al., 2016; J. A. Retana, 1999). The 1997-1998 El Niño event brought 32,8 million dollars losses in the agricultural sector (Table 1.1) which corresponded to the equivalent of the 58% of all economic damages caused by the event, Guanacaste alone registered damages in rice production of 80% (Birkel, 2005; IICA, 2001; Jiménez et al., 2016; J. A. Retana, 1999).

Sector and subsector	Damage (in million dollars)		
	Total (in million dollars)	**Direct (in million dollars)**	**Indirect (in million dollars)**
TOTAL	**$ 54,4**	**34,4**	**18,0**
Agriculture	**32,8**	**25,6**	**7,2**
For internal consumption	23,7	16,6	7,00
Rice	11,9	9,1	2,8
Beans	11,1	7,2	3,9
Corn	0,7	0,4	0,3
For export	9,2	9,0	0,2
Sugar cane	3,0	3,0	
Other	6,2	6,0	0,2
Livestock	**16,0**	**8,6**	**7,4**
Fishery sector	**3,6**	**0,2**	**3,4**

Table 1.1. Economic losses (in million dollars) in the agricultural sector in Costa Rica after the 1997/1998 event (Birkel, 2005)

Negative impacts in the agriculture sector in Costa Rica caused by the 1997-1998 El Niño event were more severe in the Huetar Norte and Chorotega regions, where beans and rice for domestic production and livestock production are concentrated. The combined effect of a prolonged drought and changes in the timing of rainfall, caused inhibition of blooming and/or the use of agricultural machinery (United Nations, 1998). At the time of the event the impact was reduced thanks to public aid and mitigation projects undertaken in a preventive way because of the long history of droughts in the region, such measures including the functioning of the Arenal Tempisque irrigation district in supplying water to farmers (United Nations, 1998).

The 2015-2016 El Niño event caused a similar situation in the Chorotega region, precipitation deficit affected population, touristic sector, livestock and agricultural production. A main concern for that area is the increase in water consumption that have caused a large use of groundwater reservoirs, in 2015 water supply came for 78% from underground waters, causing conflicts and environmental problems like groundwater salinization (Hund et al., 2018; Jiménez et al., 2016). Furthermore, there is a faster decease in groundwater resources due to deficits in the average annual wet season groundwater recharge (Hund et al., 2018).

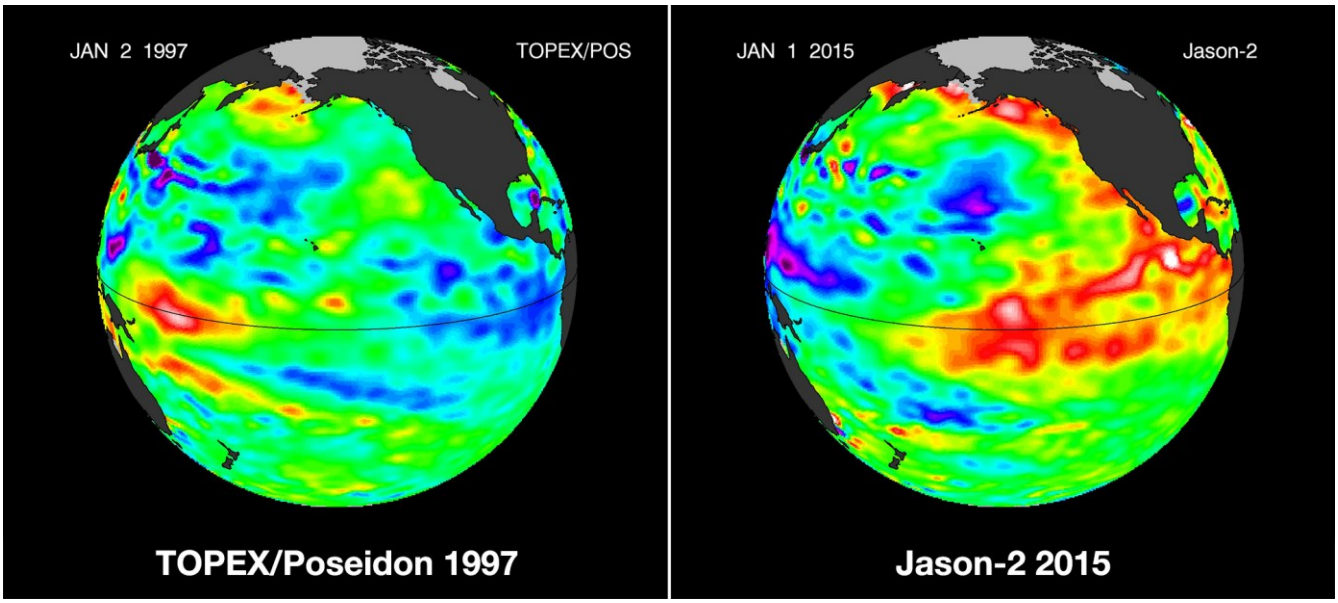

Figure 1.6. December 1997 vs. December 2015 El Niño events (NASA, 2016; https://sealevel.jpl.nasa.gov/data/el-nino-la-nina-watch-and-pdo/el-nino-2015/).

The 1997-1998 and 2015-2016 events have some common characteristics but different timing, peak months (November 1997 and January 2016) and overall different dynamics. The 2015-2016 event was stronger, longer and affected larger areas compared to the 1997-1998 event (Figure 1.6) (NASA, 2016). It is important to remember that the impact of ENSO varies according to the precipitation regime in Costa Rica, despite the relatively small size of the country. While El Niño is linked to drought in the northern Pacific area, rainfall over the Caribbean slope tends to increase under the same conditions. For the 1997-1998 event in Costa Rica, the different impact of El Niño for rainfall distribution between the Caribbean and Pacific was marked. During that event, rainfall amount in the Caribbean supered of 10% the average and a surplus of 30% caused overflowing rivers, floodings and landslides from April to November 1997 (United Nations, 1998). However, the Pacific side, and more than anywhere else the area the Chorotega region, suffered a strong precipitation deficit (50% below average), the Huetar Norte zone suffered a less severe precipitation deficit (30% below average) causing drought conditions and forest fires from November 1997 to May 1998 (United Nations, 1998).

All the reasons explained above and many more clarify the big interest on the study of this climatic phenomenon which can be said to be one of the most important worldwide, affecting climatic patterns of a big percentage of the world area. Our research area is placed in one of the directly affected regions, that is the Pacific side of Central America, characterized by common climatic features and located within the so-called the Dry Corridor of Central America (CADC, Gotlieb et al., 2019), where the most dramatic effects on many economic and social aspects are observed for Central America. The CADC stretches from the north of Costa Rica to Nicaragua, Honduras, Guatemala, and a part of the Pacific coast of Panama (Imbach et al., 2017). Climate is characterized

the dry season from November-December to April-May and the wet season from May-June to October-November interrupted by a reduction of rainfall between July and August, feature known as the Mid-Summer drought (V. Magaña et al., 1999). The tropical dry forest is the most endangered ecosystem in the region (Birkel, 2005; Imbach et al., 2017) and this area is characterized by a high vulnerability to climate change and climate variability as its population is mainly rural and involved in the agricultural sector, hence socioeconomical activities are largely dependent from ecosystem services for its livelihood and jeopardized by increasingly frequent droughts, floods and storms (Eduardo Quesada-Hernández et al., 2019; Imbach et al., 2017; Pascale et al., 2021). Despite many studies have analysed ENOS impacts on Costa Rican environment and agriculture, no previous studies related to long-term changes in NDVI are reported, this is key to understand the continuous effects of El Niño in one of the most important regions of Costa Rica for agricultural production. The goal of this study is to evaluate the impacts of the last two strongest El Niño events, the 1997-1998 event and the 2015-2016 event, on agriculture with the help of remote sensing data from Landsat from 1990 to 2021, and modern cloud computing platforms such as Google Earth Engine. These technologies allow us to develop an improved outlook of historical patterns of NDVI and key parameters correlated with ENSO.

2. Materials and Methods

2.1. Study area

The study area is the Chorotega region (Guanacaste province with an area of 10.141 km^2), located in the northern Pacific part of Costa Rica (Figure 2.1b) and that belongs in the CADC sub-region of Central America (Figure 2.1a). As previously introduced, CADC covers a large part of Central America, and a common feature of this area is its drought prone behaviour compared with the other areas of Central America. Such conditions involve multiple processes and interactions and key elements for drought development include topography, ENSO and its impact on the Caribbean Low Level Jet and associated transport of moisture for precipitation (Durán-Quesada et al., 2017, 2020; Eduardo Quesada-Hernández et al., 2019; Harvey et al., 2021). In the area, drought is the climatic phenomenon that have the most negative impact on the population which mainly rely on

agriculture for its livelihood and salary, and climate change causes uncertainty in the future suitability of this land d for the cultivation of the traditional crops (Imbach et al., 2017).

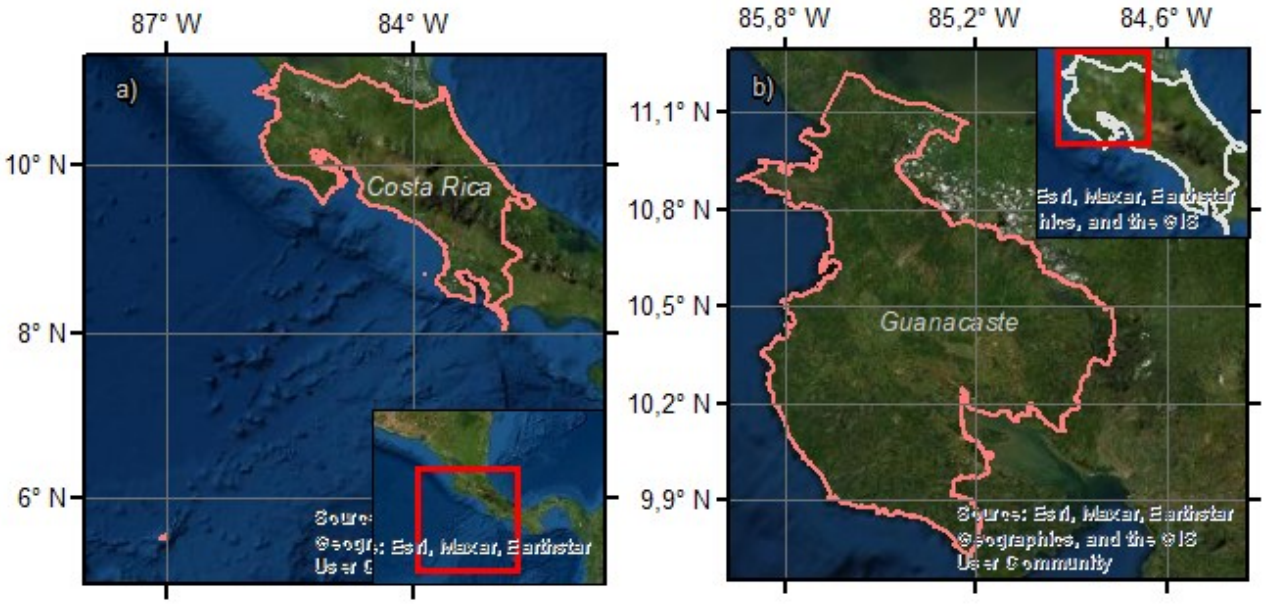

Figure 2.1. a) Location of Costa Rica in Central America; b) location of the Chorotega Region (Guanacaste province) in Costa Rica

The bimodal pattern of precipitation is the main characteristic of the Chorotega region (Birkel, 2005; J. Retana et al., 1999). Differences in precipitation amount are more marked in the part of the country belonging to the CADC, the average annual precipitation is 1710 mm (Benavides et al., 2021; Harvey et al., 2021). Mean monthly temperature is around 27,7 °C, with the average minimum reaching 23.1 °C and the average maximum 32.2 °C (J. Retana et al., 1999). East and northeast trade winds are relevant to shape the distribution of precipitation and characteristic large-scale patterns of the region are subject to variations due to the influence of tropical waves, low-pressure systems, tropical cyclones, convective systems, the Inter Tropical Convergence zone and ENOS which is the main driver of interannual variability (Durán-Quesada et al., 2020). In the study region, the influence of El Niño events often begins with an anomalous increase of the trade winds, inhibiting rainfall due to a decrease in the transport of moisture (Durán-Quesada et al., 2017) which can cause a rainfall reduction of nearly 30-40%, a longer MSD and overall temperatures increases of 1 to 2°C that for the 1997-98 event reached up to 4 °C (J. Retana et al., 1999).

It is possible to distinguish two areas with different type of predominant ecosystems and topography (Figure 2.2). The Nicoya Peninsula, covered by both tropical dry and tropical humid forests unsuitable for agriculture because of its steep slopes and infertile soils, and the Tempisque North-eastern Basin a fertile lowland

highly suitable and exploited for agriculture and pastures, originally typical ecosystems in the area were tropical dry forest and natural savannah(Calvo-Alvarado et al., 2009) .

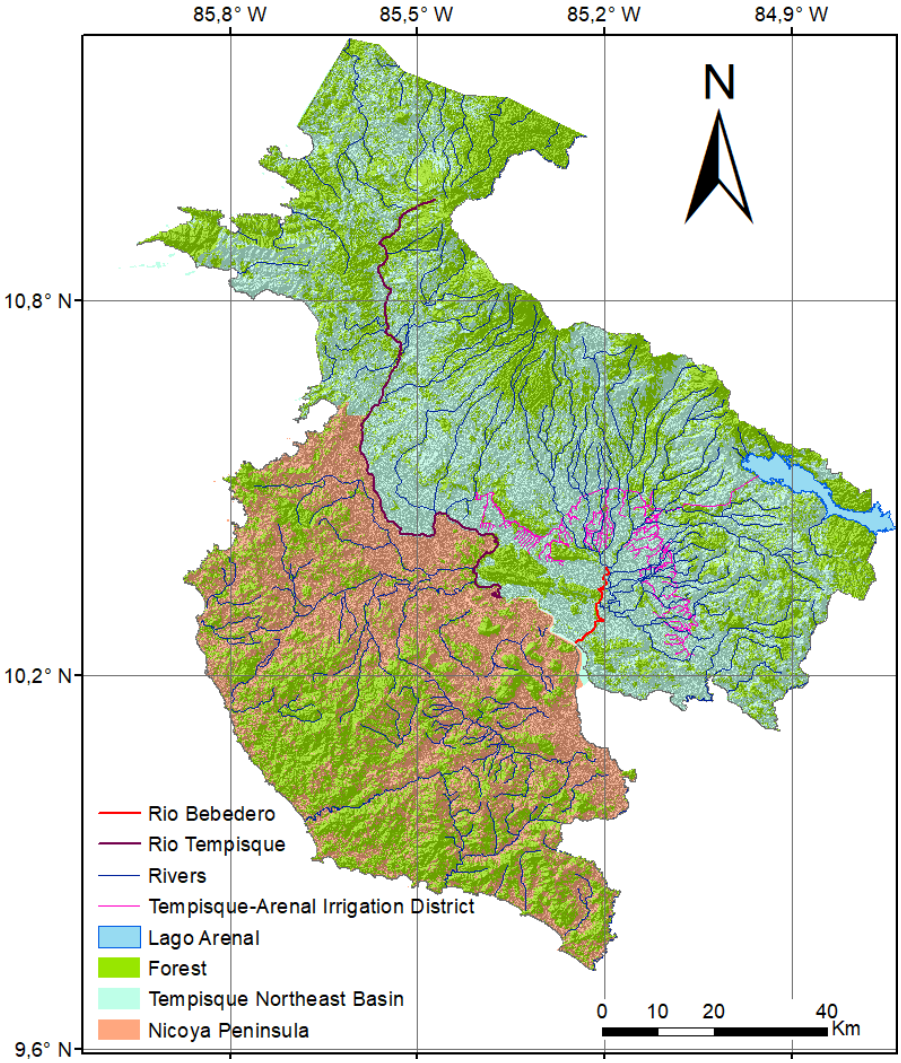

Figure 2.2. Guanacaste rivers, forests, and its Northeast Basin, Nicoya Peninsula, and the Tempisque-Arenal Irrigation District

A crucial contribution to the life of existing cultivated land is the Tempisque-Arenal Irrigation District (TAID, Figure 2.2) with its 366 km of channels is the largest in the country. The TAID takes water from the artificial Lake Arenal (with an area of 85,5 km^2) into the central lowlands of the region, in natural conditions the Lake supplies water to the Caribbean side of the country (Benavides et al., 2021; Birkel et al., 2017). The flow of rivers in Guanacaste is low and slow compared to the rest of Costa Rica and is highly affected by the annual cycle of rainfall and meteorological systems, e.g., the Tempisque river (the third longest river in the country with 144km of length, Figure 2.2) has an average flow of 24,6 m^3/s but towards the end of dry season can arrive to a flow of 2,6 m^3/s even lower mean flow and lower peaks are measured for the other important river in the catchment, the Bebedero river (Figure 2.2), emphasizing the important role of TAID in supporting production (Birkel et al.,

2017). During El Niño events, runoff volumes of less than 400mm/year were observed and during La Niña even higher than 1200 mm/year with resulting catastrophic drought and floods (Birkel et al., 2017).

Most cultivated crop in the region are, in decrescent quantity produced order, sugar cane, irrigated rice and rainfed rice cultivated during the wet season often in rotation (since 2002 in some farms) with melons grown during dry season irrigated with drip irrigation systems (Morillas et al., 2019). Melon is an opportunity crop and its production started in 1980 and mainly took the place of abandoned pastures, they are planted from mid-December to early February and grow for approximately 75 days, normally from January to April depending on climatic conditions and planting date with the harvest lasting until the end of April (Morillas et al., 2019). Rainfed rice is planted the firsts week of July when soil is dry and grows for 120 days between July and November getting abundant water during wet season, and it is harvested, depending on meteorological conditions, between the end of October and mid-November (Morillas et al., 2019). Irrigated rice is planted for the first cycle between the end of February and the beginning of March and for the second cycle in July (Lizano S, 1991). Sugar cane can be planted any time of the year, non-irrigated plants during the wet season from May to August and irrigated plants during the dry season from February to April, important is the apport of water during dry season and growing stages, once it is mature, after 12 months, it remains available continuously during the year (Flores Q, 2007; Lizano S, 1991). Albeit introduction of modern production methods at farm scale, production methods used in the area for both agriculture and pastures tend to be obsolete and therefore characterized by a low efficiency. This leads to a general waste of resources causing pollution and degradation, especially waste and overexploiting of water resources during dry periods leads to lack of water and problems for agriculture (Birkel et al., 2017). Supplied by TAID are rice and sugar cane cultivations (Benavides et al., 2021). Rice is sowed during dry season from December to February and during wet season from May to August, sugar cane is planted from January to March (Benavides et al., 2021). Hence, improvement of water use and sustainable agricultural practices is a priority for this region.

Costa Rica is well known to be one of the most successful countries in terms of landscape requalification and forest recuperation, but it has not always been like this, the big push towards innovative environmental policies and conservation initiatives came after a period of catastrophic land use change and deforestation due to a fast economic development. Between 1960 and 1979 Costa Rican deforestation rate was of 35000 ha/year and from 1979 to 1986 of 39000 ha/year, at the time between the highest rates in the world, after that, the country started to introduce conservation and reforestation policies and the land was reforested at a rate of 17000 ha/year between 1986 and 2000 and 26000 ha/year from 2000 to 2005, reforestation continued until 2013 and the biggest effort took place in the Chorotega region (Stan & Sanchez-Azofeifa, 2019; Tapia Arenas, 2016). The prevalent ecosystem in the area is the Tropical Dry Forest (TDF) which have been affected by the

expansion of agricultural and livestock production leading to high deforestation rates (Calvo-Alvarado et al., 2009). Contributing to this rapid change was the expansion of cattle industry aided by government incentives in the 50s consequently to the increase of international beef demand (Stan & Sanchez-Azofeifa, 2019). In the 60s livestock production increased by 62%, and over 40% of the production came from the Chorotega region (Stan & Sanchez-Azofeifa, 2019). Originally the region hosted the 97% of the tropical dry forests of Costa Rica, from the 50s have experienced a big economic development in primary, secondary and tertiary sectors followed by an important land use change which led to catastrophic deforestation rates, the highest in the country, until the 80s, when meat market declined (Stan & Sanchez-Azofeifa, 2019; Tapia Arenas, 2016). Since the 90s, environmental problems, market decline, conflicts linked to water overexploitation increased and pointed out the need for a change in direction and the introduction of conservation policies with the creation of protected areas (25% of the region) and shifting economic incentives towards other activities like sustainable tourism, Payments for Environmental Services (PES), and clean energy production but cash crops and livestock production remain the main activities in the region, jeopardizing natural and protected areas together with population growth (Stan & Sanchez-Azofeifa, 2019). From 1986 to 2000, forest cover increased from 23,1% to 40,4% to around 50% in 2005, to 60 % in 2015, mainly due to the abandonment of pastures and degraded lands no more suitable for agriculture, shift of the regional economy towards touristic sector, the prohibition of wood extraction from natural forests, the policies introduced by the country like the Payment for Environmental Services (PES) contributing to the protection of 31 2017 ha of forest until 2015, and the forest restoration efforts (Calvo-Alvarado et al., 2009; Tapia Arenas, 2016).

2.2. Selection of the most significant events

Given the relevance of intense El Niño events for the region, the most severe events in terms of strength and duration analysing official historical records of the area were selected. Information from the Costa Rica National Meteorological Institute (IMN) records, monthly updated section for early warning of El Niño phenomenon and available from https://www.imn.ac.cr/boletin-enos was used. As shown Figure 2.3 from NOAA, normalized SST anomalies are used to identify the most significant events. SST anomalies can be considered between the best parameters to identify El Niño influence over the analysis region, because the warm current typical of the event directly touches the Pacific coasts of Costa Rica. In the selection of the events, the different indices explained in the introduction (i.e., SOI, ONI and OLR, Figure 1.2, Figure 1.3, and Figure 1.4) were compared with IMN bulletin information, together with precipitation data from regional IMN network and NASA publications about ENSO.

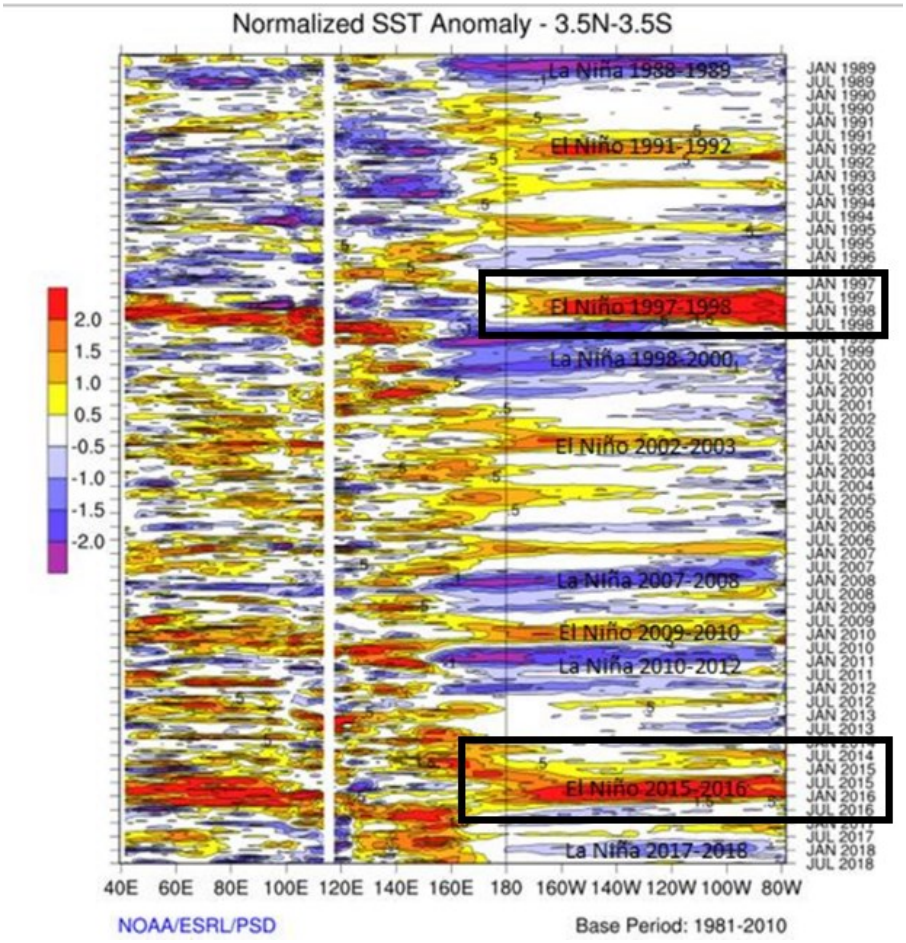

Figure 2.3. Sea Surface Temperature Anomalies record from January 1989 to July 2018 (https://www.imn.ac.cr/boletin-enos)

2.3. Precipitation data

ENSO is the main driver of alterations of normal seasonal patterns in the region, its development varies for the events as it does not have a fixed timing to develop. It is well known that the El Niño tends to cause severe drought in the CADC, with the consequent precipitation reduction, which is noticeable from time series. Precipitation reduction leads to river flows reduction, groundwater recharge reduction and consequently to vegetation stress that together with increased temperature and strong winds increases evapotranspiration from plants.

In this study, precipitation data from the IMN historical record and available for this research as parto of the B7507 project (MCITT grant) was used to observe drought conditions induced by precipitation deficit during the selected El Niño events and compare it with NDVI trends. Precipitation records from 27 stations in the region from 1990 to present were used and their distribution is shown in Figure 2.4. Ten stations for every month were selected between the ones containing fewer missing data (Table 2.1).

Period	Selected stations										
12/1989 to 11/1994	Code	CR00000122	CR00000033	CR00000036	CR00000018	CR00000132	X74008	X74002	X74006	X74037	X76041
	Name	Cañas, Guanacaste	Llano Grande, Liberia	Bagaces	Nicoya Extension Agricola	Santa Cruz	Pelon de la Bajura, Liberia	Filadelfia	La Guinea, Filadelfia	Finca Las Huacas, Liberia	Ingenio Taboga, Cañas
12/1994 to 11/1998	Code	CR00000122	CR00000033	CR00000036	CR00000018	CR00000132	X72129	X74002	X74006	X74037	X76041
	Name	Cañas, Guanacaste	Llano Grande, Liberia	Bagaces	Nicoya Extension Agricola	Santa Cruz	Murciélago	Filadelfia	La Guinea, Filadelfia	Finca Las Huacas, Liberia	Ingenio Taboga, Cañas
12/1998 to 4/1999	Code	CR00000122	CR00000033	CR00000036	CR00000018	CR00000132	X74008	X74002	X74006	X74037	X76041
	Name	Cañas, Guanacaste	Llano Grande, Liberia	Bagaces	Nicoya Extension Agricola	Santa Cruz	Pelon de la Bajura, Liberia	Filadelfia	La Guinea, Filadelfia	Finca Las Huacas, Liberia	Ingenio Taboga, Cañas
5/1999 to 11/2006	Code	CR00000122	CR00000033	CR00000036	CR00000129	CR00000132	X74008	X74002	X74006	X74037	X76041
	Name	Cañas, Guanacaste	Llano Grande, Liberia	Bagaces	Finca la Ceiba, Pueblo Viejo, Nicoya	Santa Cruz	Pelon de la Bajura, Liberia	Filadelfia	La Guinea, Filadelfia	Finca Las Huacas, Liberia	Ingenio Taboga, Cañas
12/2006 to 4/2011	Code	CR00000122	CR00000033	CR00000036	CR00000129	CR00000132	X74008	X74002	CR0000001	X74037	X76041
	Name	Cañas, Guanacaste	Llano Grande, Liberia	Bagaces	Finca la Ceiba, Pueblo Viejo, Nicoya	Santa Cruz	Pelon de la Bajura, Liberia	Filadelfia	Nicoya Extension Agricola	Finca Las Huacas, Liberia	Ingenio Taboga, Cañas
5/2011 to 11/2011	Code	CR00000122	CR00000033	CR00000036	CR00000129	CR00000132	X74008	CR0000013 1	CR0000001 8	X74037	X76041
	Name	Cañas, Guanacaste	Llano Grande, Liberia	Bagaces	Finca la Ceiba, Pueblo Viejo, Nicoya	Santa Cruz	Pelon de la Bajura, Liberia	Aeropuerto, Liberia	Nicoya Extension Agricola	Finca Las Huacas, Liberia	Ingenio Taboga, Cañas
12/2011 to 11/2013	Code		CR00000033	CR00000036	CR00000129	CR00000132	X74008	CR0000013 1	CR0000001 8	X74037	X76041
	Name		Llano Grande, Liberia	Bagaces	Finca la Ceiba, Pueblo Viejo, Nicoya	Santa Cruz	Pelon de la Bajura, Liberia	Aeropuerto, Liberia	Nicoya Extension Agricola	Finca Las Huacas, Liberia	Ingenio Taboga, Cañas
12/2013 to 4/2014	Code		CR00000033	CR00000036	CR00000129	CR00000132	X74008	CR0000013 1		X74037	X76041
	Name		Llano Grande, Liberia	Bagaces	Finca la Ceiba, Pueblo Viejo, Nicoya	Santa Cruz	Pelon de la Bajura, Liberia	Aeropuerto, Liberia		Finca Las Huacas, Liberia	Ingenio Taboga, Cañas
5/2015 to 11/2015	Code		CR00000033	CR00000036	CR00000129	CR00000132	X74008	CR0000013 1	CR0000013 3	X74037	X72129
	Name		Llano Grande, Liberia	Bagaces	Finca la Ceiba, Pueblo Viejo, Nicoya	Santa Cruz	Pelon de la Bajura, Liberia	Aeropuerto, Liberia	Hacienda Mojica, Bagaces	Finca Las Huacas, Liberia	Murciélago
12/2015 to 11/2017	Code		CR00000033		CR00000129	CR00000132	X74008	CR0000013 1	CR0000013 3	X74037	X72129
	Name		Llano Grande, Liberia		Finca la Ceiba, Pueblo Viejo, Nicoya	Santa Cruz	Pelon de la Bajura, Liberia	Aeropuerto, Liberia	Hacienda Mojica, Bagaces	Finca Las Huacas, Liberia	Murciélago
12/2017	Code		CR00000033		CR00000129	CR00000132	X74008	CR0000013	CR0000013	X74037	
	Name		Llano Grande, Liberia		Finca la Ceiba, Pueblo Viejo, Nicoya	Santa Cruz	Pelon de la Bajura, Liberia	Aeropuerto, Liberia	Hacienda Mojica, Bagaces	Finca Las Huacas, Liberia	
1/2018 to 11/2019	Code				CR00000129	CR00000132	X74008	CR0000013 1	CR0000013 3	X74037	
	Name				Finca la Ceiba, Pueblo Viejo, Nicoya	Santa Cruz	Pelon de la Bajura, Liberia	Aeropuerto, Liberia	Hacienda Mojica, Bagaces	Finca Las Huacas, Liberia	
12/2019 to 4/2020	Code				CR00000129	CR00000132	X74008	CR0000013 1	CR0000013 3		
	Name				Finca la Ceiba, Pueblo Viejo, Nicoya	Santa Cruz	Pelon de la Bajura, Liberia	Aeropuerto, Liberia	Hacienda Mojica, Bagaces		
5/2020 to 4/2021	Code						X74008	CR0000013 1	CR0000013 3		
	Name						Pelon de la Bajura, Liberia	Aeropuerto, Liberia	Hacienda Mojica,		

Table 2.1. Selected stations for precipitation time series. Precipitation data were provided by IMN

Some months contained data gaps which were filled by calculating the average of the same month for the ten previous or closest years, lowest and highest value were excluded from the calculation. Stations with more than 55% missing data were not considered.

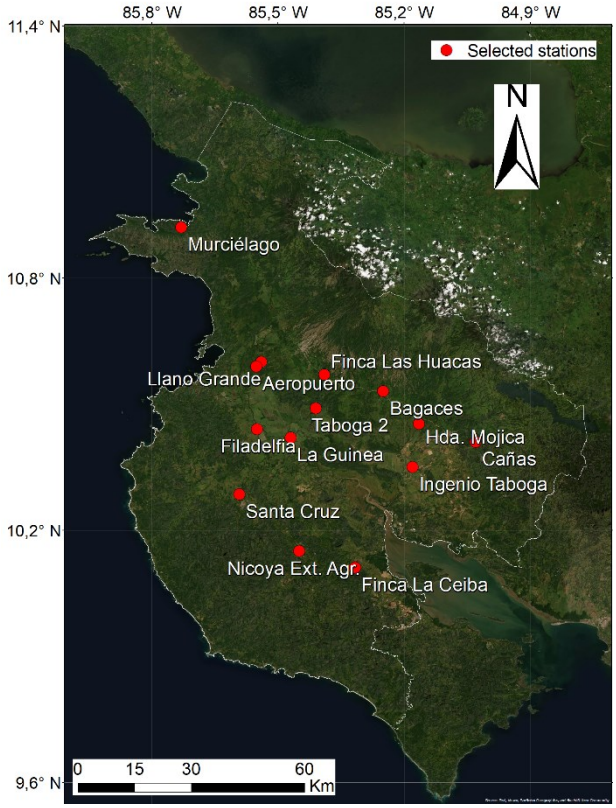

Figure 2.4. Selected stations

Then annual, dry and wet season time series charts were developed. To build annual charts, values were averaged for the 12 months of every year from 1990 to 2021. To build dry seasons charts, values were averaged for the 5 months (December to April) of every dry season from 1990 to 2021, the same was done for the 7 months (May to November) of the wet seasons for every year from 1990 to 2021.

2.4. Remote sensing images

2.4.1. What is remote sensing

Remote sensing consists in the detection of physical information of a surface from distance by a sensor (usually a camera) belonging to a platform (e.g., satellite, aircraft, UAV, UGV or a probe) (Weiss et al., 2020). The information acquired can be used in many fields and for different purposes, some examples are detection of forest fires, observation of clouds and storms, tracking land use changes over time, study topography, hydrological characteristics of a territory, even vegetation status and temperatures of surfaces through the analysis of their reflected or emitted electromagnetic radiation (Weiss et al., 2020).

Electromagnetic radiation is a type of energy characterized by a spatial and temporal wave-like motion, oscillating in all directions perpendicularly to their travel direction, in the form of radio waves, X-rays, microwaves and gamma rays depending on their characteristic wavelength or frequency (period) (Emery & Camps, 2017).

The wavelength (λ) is the distance between one crest of the wave and the adjacent one, the frequency (ν or f) often reported in Hertz (Hz or s^{-1}) describes the number of oscillations (or cycles) per second (Figure 2.5) (Emery & Camps, 2017). In free space (or vacuum) electromagnetic radiations travel at a constant speed (λ ν ≈ 300 000 km/s) given by the wavelength multiplied by the frequency, which corresponds to the speed of light (Emery & Camps, 2017).

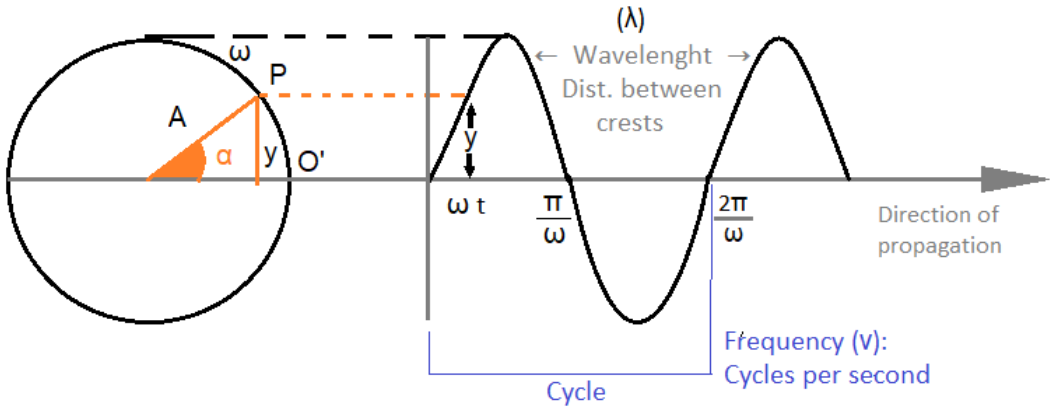

Figure 2.5. Electromagnetic waves behaviour

The fundamental particle of electromagnetic radiation is the photon, which contains emitted, reflected and absorbed radiation and is characterized by a specific energy (E) described by the Planck's equation (2.1):

$$E = h \cdot \nu, \tag{2.1}$$

Where *h* is the Planck's constant ($h = 6{,}62607 \times 10^{-34}\ J \cdot s$) and *ν* the frequency.

With remote sensing, we can analyse the meaning of different reactions (in terms of photons emissions characterized by different wavelengths and frequencies from which we can understand determined characteristics of the object) of a surface excited by a certain external radiation or internal process (Emery & Camps, 2017). Energy changes cause emission of photons in case of a decrease and an absorption in case of increase, and its frequency and wavelength values depend on the how big is the energy change, the complete range of values of frequencies and wavelengths (energies) a photon can assume, is described by the electromagnetic spectrum (Figure 2.6) (Emery & Camps, 2017).

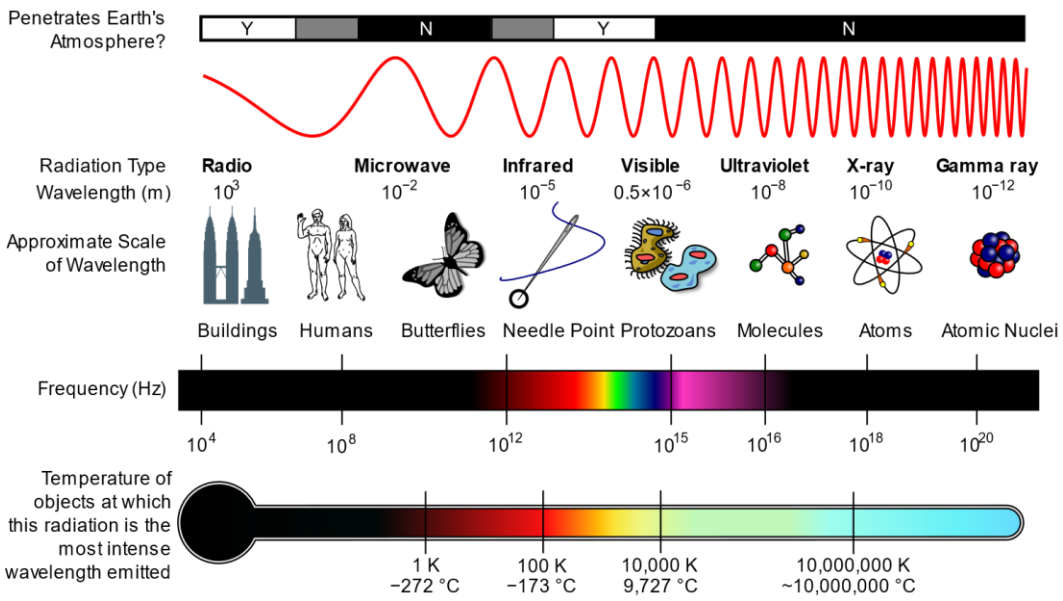

Figure 2.6. Electromagnetic spectrum properties from (https://commons.wikimedia.org/wiki/File:EM_Spectrum_Properties_edit.svg)

The human eye can see only a small range (0,4 to 0,7 µm) of this radiation, called the visible region, which results of a surface excitement by incoming solar radiation, going from the red colour (long wave, 0,7 µm, low frequency, low energy) to the blue colour (short wave, 0,4 µm, high frequency, high energy), the white colour contains all the radiations from the visible region mixed, these are all reflected radiations and are used for the remote sensing of colours (Figure 2.7) (Emery & Camps, 2017). With remote sensing we can go beyond the limits of human eyes because it allows us to observe lager areas and analyse surface's radiation at wavelengths and frequencies invisible for us (Huete, 2004).

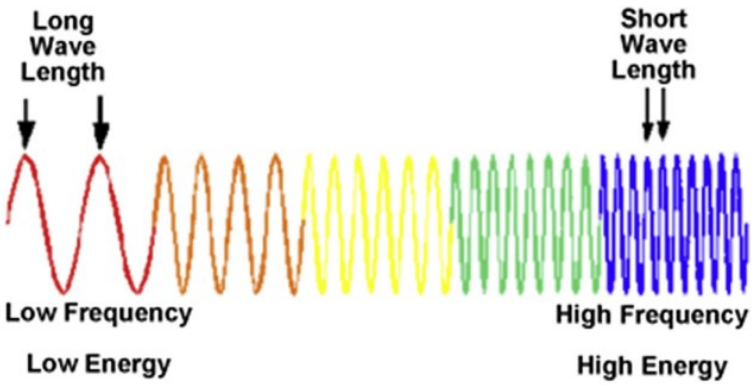

Figure 2.7. Visible colours spectrum from(Emery & Camps, 2017)

Shorter wavelengths than the visible range are characteristic of Ultraviolet (UV), X-Ray, and Gamma-ray radiations, longer wavelengths are characteristic of Near Infrared Radiations and Middle Infrared Radiations (NIR

and MIR, 0,7 to 3 µm) both are still detected by sensors as reflected radiation, longer wavelengths from 10^{-5} until 10^{-3} m contain thermal emissions and are called TIR (Thermal Infrared radiation) (Emery & Camps, 2017).

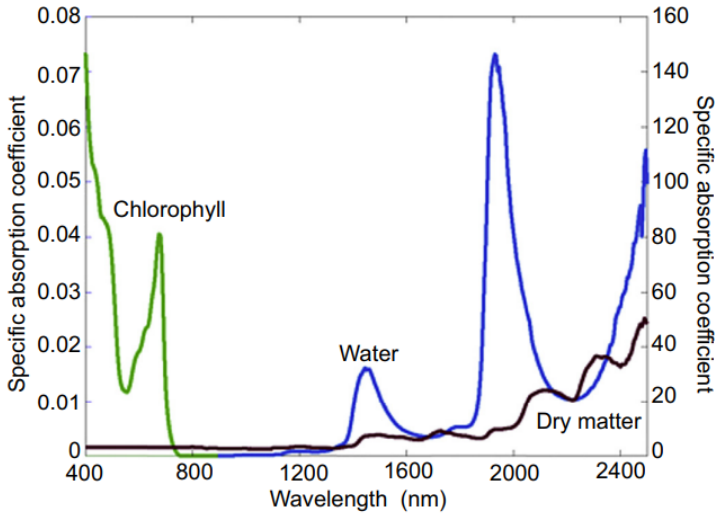

Figure 2.8. Chlorophyll, water and dry matter light specific absorption coefficient at different wavelengths (Emery & Camps, 2017).

NIR and MIR are widely used to study vegetation status because it responds very well to water contained in the leaf which can be a good indicator of plants health (Figure 2.8) (Emery & Camps, 2017). Spatial, temporal, optical characteristics of data acquired with remote sensing depend on the proprieties of the sensor (spatial, temporal, spectral and radiometric resolution) and the platform on which is mounted on, and on surface's emitted or reflected radiation (Huete, 2004; Weiss et al., 2020). The dimension of detectable objects in an image which is composed of pixels, each of which contain a specific square area determining the spatial resolution (Huete, 2004). The number of detectable wavelengths by a sensor determine its spectral resolution, the time taken by the satellite to pass over a specific area for the second time is the temporal resolution (Huete, 2004).

A surface's emitted (thermal) or reflected radiation is unique and characteristic, it is called spectral signature (Figure 2.9) and allow us to see its mineral, organic composition, and moisture, by observing surface's luminosity and shadowing we can easily see its structural properties (Huete, 2004). The capability of a sensor to distinguish reflectance or light intensity differences defines the radiometric resolution (Huete, 2004).

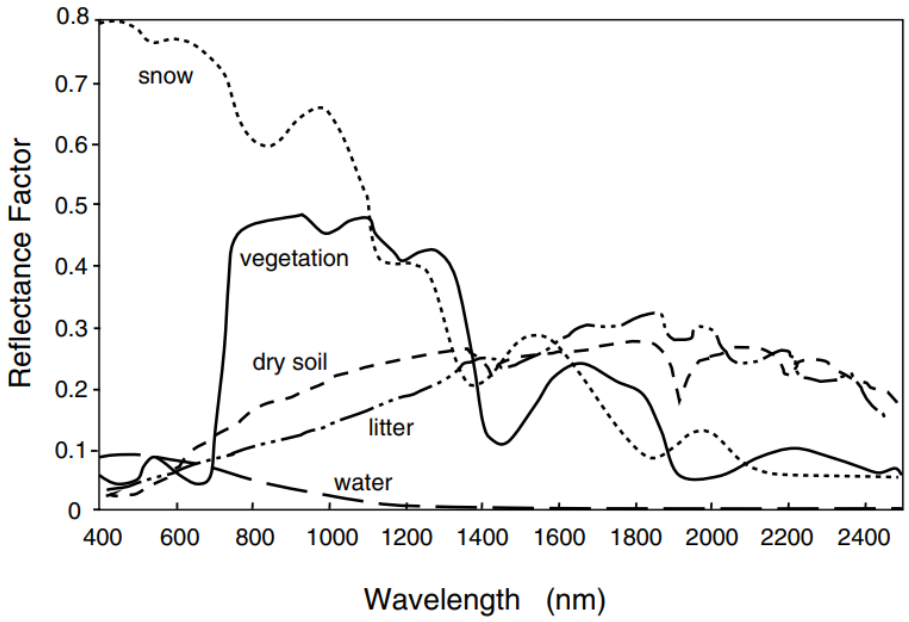

Figure 2.9. Spectral reflectance signatures of snow, vegetation, dry soil, litter and water. From (Huete, 2004)

Leaf pigments absorb light in the visible region (400-700 nm), in fact, chlorophyll (green pigment) a and b absorb respectively blue (400-500 nm) and red (600-700 nm), green colour (500-600 nm) is the least absorbed and mostly is reflected and that's why healthy leaves are green (Huete, 2004). Carotene (orange-red pigment) and xanthophyll (red and blue pigment) have a strong absorption of blue (400-500 nm) (Huete, 2004). Not healthy vegetation reflects and absorb lights over different wavelengths, so it becomes easy to discriminate stressed from healthy plants (Huete, 2004). NIR wavelengths (700-1300 nm) are strongly reflected by vegetation, and pigments and cellulose are transparent to them, observable only by specific sensors different from human eyes (Huete, 2004). The red edge is the evident increase of reflectance between red and NIR wavelengths and it is widely used to observe plants status, MIR wavelengths (1300-2500 nm) are absorbed by soil and leaf moisture and reflected as moisture decreases, especially at 1400 and 1900 nm (Huete, 2004).

2.4.2. Remote sensing environmental applications

The study of the environment and its evolutions and dynamics over time, includes the analysis of climate and atmospheric features, land use, land cover and vegetation characteristics. Remote sensing can provide all the needed information for such task if data acquisition and process is known. In this way, satellites retrievals enable the estimation of surface temperature, wetness, shape, atmospheric parameters, physical characteristics, aerosols, fires and recognized gases based on their spectral signatures (Table 2.2) (Huete, 2004). This information allows to monitoring climate change, droughts and floods, extreme climate phenomena, trace deforestation, and volcanic eruptions among others (Huete, 2004).

Spectral Region	Wavelengths	Application
Ultraviolet (UV)	0,003 to 0,4 µm	Air pollutants, ozone depletion monitoring
Visible (VIS)	0,4 to 0,7 µm	Pigments, chlorophyll, iron, ice
Near infrared (NIR)	0,7 to 1,3 µm	Canopy structure, biomass
Middle infrared (MIR)	1,3 to 3,0 µm	Leaf moisture, wood, litter
Thermal infrared (TIR)	3 to 14 µm	Drought, plant stress, temperature
Microwave	0,3 to 300 cm	Soil moisture, roughness

Table 2.2. Spectral regions used in environmental studies. From (Huete, 2004)

Ultraviolet, Visible, Near and Middle Infrared are shortwave radiations, TIR and microwave are longwave radiations (Huete, 2004). Atmospheric gases alter radiation reaching the sensor by scattering or absorbing it, therfore images acquired by satellites need to be corrected from these disturbances (caused by gases and clouds) (Huete, 2004).

To map landscape changes over time by analysing series of images of the same area for long periods and observe land use and land cover modifications, global remote-sensed products normally divide landscape features in wide land cover type classes such as grassland, forest, urban areas and water bodies is very useful to monitor and understand environmental changes (Weiss et al., 2020). More precise information, such as mapping of specific crop type or species is difficult to obtain for large areas with satellites because for this purpose finer spatial and temporal resolution are needed as well as spectral information of how to recognize a specific plant by reading satellite data (Weiss et al., 2020). Satellites used for environment-related studies orbit Earth with a low (600 to 950 km above the surface) polar orbit, most used and chosen depending on the extension of the study area and the purpose of the study, are sensors with a spatial resolution ranging from 1m to 100 m (fine spatial resolution but with a temporal resolution higher than 16 days) and from 250m to 1km (moderate spatial resolution but with a higher temporal resolution, from 1 or 2 days) (Huete, 2004).

2.4.2. Remote sensing product selection

Landsat series are widely used for environmental applications, the orbit is at 705 km above the surface and have a temporal resolution of 16 days (Huete, 2004). First Landsat satellite was launched in 1976 and had mounted on board a Multispectral Scanner (MSS) sensor with four broad bands able to detect visible and NIR regions, with a spatial resolution of ~ 80 m and a temporal resolution of 18 days (Huete, 2004). With the launch of Landsat 4 and 5 respectively in 1982 and 1984, the Thematic Mapper (TM) sensor, with seven spectral bands

of which two in the MIR, one in the thermal, two shortwave infrared (SWIR) channels, and a finer spatial resolution (30 m), was added to the MSS (Huete, 2004). In April 1999 Landsat 7 was launched, with and added sensor, the Enhanced Thematic Mapper Pluc (ETM+) with a 15 m resolution panchromatic band and a 60 m (instead of 120 m of TM) resolution thermal band (Huete, 2004). A big turn in Landsat history was made in 2008, thanks to the choices made from the two federal Landsat partners, NASA, and the U.S. Geological Survey (USGS), which contributed to the opening of databases to public, making data accessible for free (Wulder et al., 2019). Before 2008, data purchase was expensive (around $4000), and every year were sold only 25000 images. After the dataset was opened, the number of images distributed increase to about 250000 images per month, increasing enormously the potential of the products and opening new frontiers for research (Schmid, 2017). Landsat 8 was launched in February 2013, with improved overall radiometric, spectral and geometric resolutions of the OLI (Operation Land Imager) sensor, with new channels, enhanced blue for coastal aerosols detection and cirrus channels for aquatic studies and correct cloud disturbance, and a Thermal Infrared Sensor (TIRS) (Wulder et al., 2019). Cloud-based computing such as Google Earth Engine (GEE) code editor allow scientist to process and analyse data efficiently opening new frontiers in environmental studies. Landsat 9 was launched successfully in September 2021.

Landsat has been monitoring Earth continuously for nearly 50 years now, allowing the study of a global long time series of fine resolution images. It was because of Landsat programs, and its long term precise environmental monitoring characteristics, that many environmental initiatives to monitor and mitigate climate change have been possible. Focus on the climate change issue was highlighted during the UNFCCC (United Nations Framework Convention on Climate Change) held in Rio de Janeiro in 1992, in which a tool to “reduce emissions from deforestation and forest degradation” known as REDD+ was launched. Landsat is regarded as the only free available product with the required spatial and temporal coverage to support conservation policies to protect carbon stocks and improve forest management (Wulder et al., 2019).

Landsat products can be used to monitor the area of interest because of the high spatial resolution (30m), perfect for the small study area, temporal resolution (16 days), spectral resolution and big archive of information allowing the assessment of changes over a long period of time, 1990 – 2021 in the case of this research. It is the aim of this work to analyse NDVI changes after the strongest El Niño events of the last 30 years which were the 1997-1998 event and the 2015-2016 event, selected by considering the three ENSO indices described above (Figure 1.2, Figure 1.3 and Figure 1.4) as well as available literature and public Costa Rican observational records (NASA, 2016). The analysis herein presented considered retrievals from Landsat 5 (functional from 1984 to 2012), Landsat 7 (functional from 1999 to date) and Landsat 8 (functional from 2013 to date).

On 31st May 2003, Landsat 7 Enhanced Thematic Mapper Plus (ETM+) Scan Line Corrector (SLC), essential for the continuous acquisition of the image, failed, resulting in damaged images which show gaps, zigzag patterns and overlaps as shown in Figure 2.10b (Markham et al., 2004; Scaramuzza & Barsi, 2005). The failure was irreversible, and ETM+ sensor continued to operate but with SLC turned off, so SLC-off images became available in November 2003 (Scaramuzza & Barsi, 2005). Efforts were made to fix damaged images by USGS and NASA which have developed a gap-filled product launched in November 2004, the product still has limitations such as gaps appearing as clouds in cloud-free images and dark spots (Scaramuzza & Barsi, 2005).

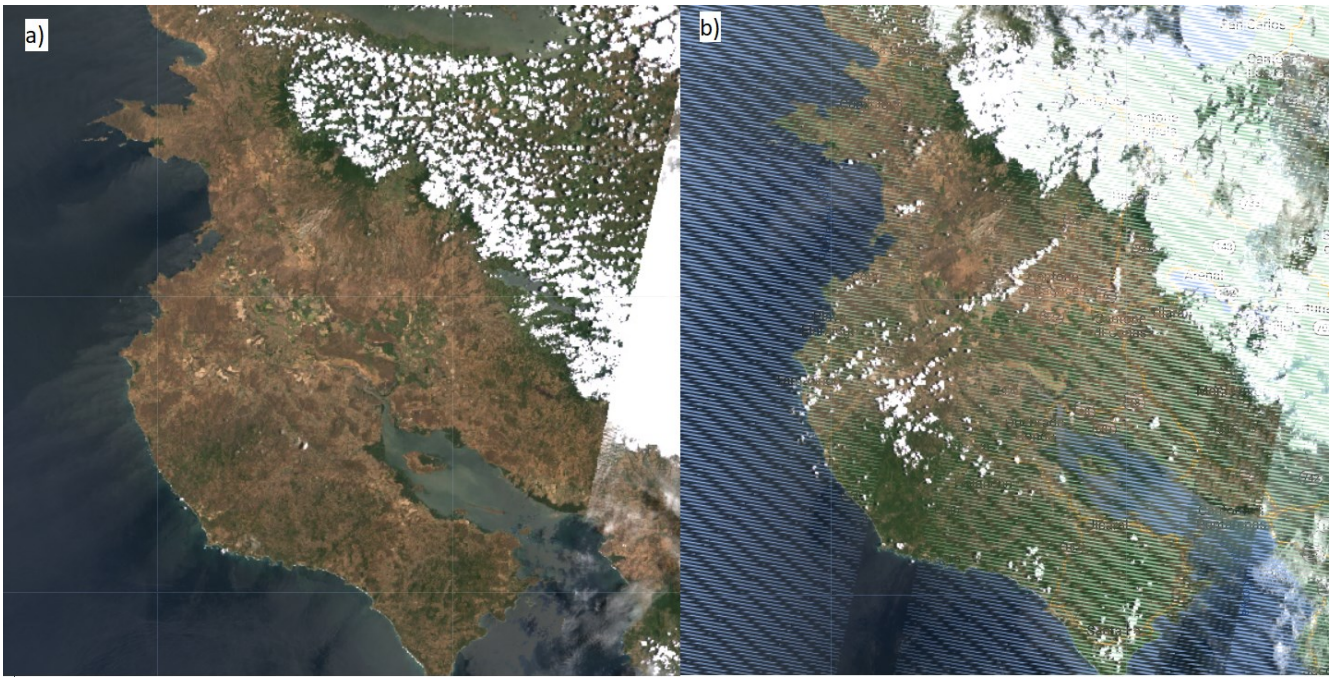

Figure 2.10. Landsat 7 images downloaded from Google Earth Engine code editor of April a) before the failure, 2001; b) after the failure, 2005

As observed in the northwest of the region in Figure 2.10, Landsat images are often affected by clouds and cloud shadows because of the optical nature of its sensors and this does not depend on the sensor characteristics but on climatic condition of the area studied, which is often covered by clouds because of the recurrent turbulences and most of all during the long annual wet season (Cao et al., 2021). To overcome this problem, USGS developed an algorithm called Function of mask (Fmask) to create the Quality Assessment (QA) band for each image of Landsat 4, Landsat 5, Landsat 6, Landsat 7, and Landsat 8. Pixels recognized as clouds or cloud shadows are reconstructed in the QA band, this method is not very precise, and it does not work for pixel entirely composed by clouds (Cao et al., 2021). In this study, images from the Landsat collection were chosen for their fine spatial resolution and temporal coverage. Landsat 5 was used for the time period from 1990 to 1999. Landsat 7 was used from 2000 (the first year in which complete images were available for the Chorotega region) until 2014 because it is a more advanced and complete product than the previous one. Since 2014, images have

been available from Landsat 8, of the three datasets the most complete, which was chosen to analyse the time period from 2014 to 2020. For this work, images were downloaded from GEE code editor platform, through which mean NDVI values were calculated for dry season, wet season, and the entire year.

2.5 Google Earth Engine

After the big turn of 2008 with the free Landsat product distribution policy, the next step for public to widen the use of imagery was to find an efficient and accessible computing platform able to store and process available datasets such as Amazon Web Services (AWS) by Amazon, Azure by Microsoft and Google Earth Engine (GGE) by Google (Amani et al., 2020). Google have created a massive free-access computing platform, launched in 2010, grouping a large set (more than 10 PB) of remote sensing data, downloadable in raster format, from most important satellites and datasets to improve Earth monitoring and research project (Amani et al., 2020; Schmid, 2017).

The GGE platform includes three components: the Earth Engine (EE) Explorer, The Earth Engine (EE) Code Editor, and the Earth Engine Timelapse (Amani et al., 2020). The Earth Explorer allows the user to display data of the big Data Catalog (Annex A) online, and in the Workspace section, to zoom the map in the desired location, display in RGB or grey/pseudocolor, modify luminosity, contrast or opacity and add different layers from different datasets (Amani et al., 2020). The GEE Code Editor is accessible by a free online application and is a web-based integrated development environment (IDE) for running datasets in a JavaScript and Python application programming interface (API) extremely simplifying geospatial analyses also for less skilled researchers in web programming because Google have facilitated data processing to a point that operations with manipulation of massive amount of data that before could have taken millions of hours now have drastically reduced to hundred hours or even less depending on users' objective (Amani et al., 2020; Schmid, 2017). With the code editor it is possible to process and extract from images a big variety of information, and in addition to data accessible from Google Data Catalog, user can upload his own data (e.g., rasters and/or shapefiles) if he needs it, it is also possible to write polygons, lines and point by using the "*Geometry*" tool (Amani et al., 2020). The Time Lapse section allow users to see the surface evolution through cloud-free global remote sensed images years from 1984 to date, very useful to see effects of climate change and natural or anthropogenic world surfaces' modifications (Amani et al., 2020).

Among the most important datasets, we find the Landsat series (from 1984 to present), very useful for studies observing changes of parameters over time and for their fine resolution to study small regions, the only problem are clouds, which can be masked by working with multitemporal images (Amani et al., 2020). Another famous database is the Sentinel series developed by the European Space Agency (ESA) characterized by a very

high spatial resolution, in orbit from 2014 to date (Amani et al., 2020). The well-known MODIS series from 2000 to present is also included in GEE Data Catalog, with its near-real-time (NRT) national and global surface mapping and a spatial resolution from 250m to 1km (Amani et al., 2020). GEE can be applied to many fields such as Urban monitoring and modelling, vegetation characteristics such as biodiversity mapping, hydrology, natural disasters monitoring, the study of land cover dynamics, atmosphere and climate analysis, image processing, soil characterization and monitoring, and most important for this study, can be widely applied in the agricultural sector (Amani et al., 2020). NDVI images composites were generated and downloaded from GEE Code Editor platform in .tif format and the mean NDVI value for the period selected in .csv format, in this study were used Landsat images elaborated with specific scripts.

2.6. The Normalized Difference Vegetation Index (NDVI)

2.6.1. NDVI characterization

Images acquired by optical sensors such as the ones on board of Landsat, are composed by multiple bands which can be combined to derive desired information (S. Huang et al., 2021). The objective of this study is to evaluate the vegetation conditions trends over time and space which can be easily observed through the calculation of a wide set of multispectral vegetation indices which use canopy reflectance. The most known is the NDVI, which analyse reflectance in red and NIR wavelengths (Huete, 2004; Schmid, 2017). NDVI can be easily correlated with vegetation status and density and is obtained by calculating the normalized difference between two satellite bands (2.2), the near infrared (NIR) (0.7-1.3µm) and the red band (R) (0.6-0.7µm) reflectance as follows:

$$NDVI = \frac{(NIR - R)}{(NIR + R)} \tag{2.2}$$

The index can assume values ranging from -1 to +1, negative values indicate water bodies, values close to 0,1 could indicate stones, sand, concrete and snow, positive values are typical of vegetation, e.g., 0,3 indicate sparse vegetation, 0,6 to 1 indicate different types of forest/vegetation densities, the higher the value the "greener" the vegetation is (S. Huang et al., 2021; Schmid, 2017). NDVI is useful to discriminate different land covers (Figure 2.11), forecast crop yields, estimate biomass and Leaf Area Index (LAI), and plant response to different climatic conditions (S. Huang et al., 2021).

Remote sensing images allows the observation of the dynamics in the NDVI which can be easily correlated and often shows a direct relationship with climate and precipitation dynamics because vegetation conditions mainly depend on these variables. However, this relationship is not always obvious, especially in

tropical regions, unless for extreme events such as El Niño (Erasmi et al., 2009). Drought conditions should inhibit photosynthesis and reduce evapotranspiration causing a decrease in red light absorption by the leaf resulting in a decrease of NDVI value, Erasmi et al., 2009 have studied NDVI change in Indonesia after El Niño events under different land uses and found that tropical forest resulted almost undisturbed while cropland and shrubland have visibly suffered the anomalous changes of climatic conditions (Erasmi et al., 2009).

This study aims to measure vegetation response to drought conditions through NDVI calculation, which is expected to be negative, as observed in many previous studies (Rembold et al., 2016). Figure 2.11 is an example of how it is possible to interpretate different values of NDVI to discriminate different land cover types, the comparison between Figure 2.11b, representing mean NDVI distribution of January and February 2021 calculated with GEE Code Editor on multitemporal Landsat 8 images, Figure 2.11a, derived by 2020 Global land cover map from GlobeLand30 database and Figure 2.11c, an aerial image of the same area taken from Google Earth Explorer.

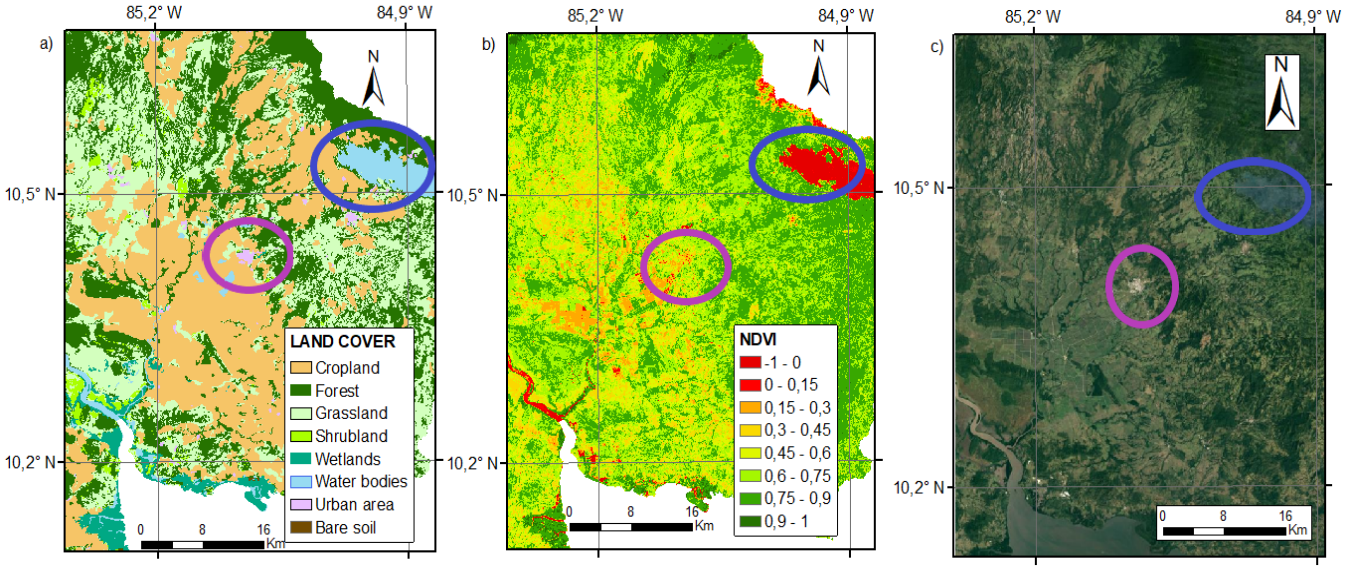

Figure 2.11. Comparison between a) GlobeLand30 2020 land cover map; b) mean NDVI of January-February 2021; c) Aerial photo, screenshot from Google Earth Explorer. All three images represent the same area.

2.6.2. NDVI calculations in Google Earth Engine Code Editor

Using GEE Code Editor, multitemporal monthly mean NDVI values were calculated from Landsat 5,7 and 8 for the period from 1990 to 2021. From 1990 to 1999 was used Landsat 5 dataset. First, it was selected and imported the collection (LANDSAT/LT05/C01/T1_SR) and imported the region boundaries shapefile of the region, derived from ArcGis Online, as shown in the input script (Annex B). For Landsat 5 the USGS Landsat 5 Collection

1, Surface Reflectance, Tier 1 dataset from the ETM sensor creating images containing 4 bands in the visible and NIR and 2 bands in the short-wave infrared (SWIR) (Table 2.3) was selected.

Name	Units	Scale	Wavelenght	Description
B1		0,0001	0,45 – 0,52 µm	Band 1 (blue) SR
B2		0,0001	0,52 – 0,60 µm	Band 2 (green) SR
B3		0,0001	0,63 – 0,69 µm	Band 3 (red) SR
B4		0,0001	0,77 – 0,90 µm	Band 4 (near infrared) SR
B5		0,0001	1,55 – 1,75 µm	Band 5 (shortwave infrared 1) SR
B6	Kelvin	0,1	10,40 – 12,50 µm	Band 6 brightness temperature
B7		0,0001	2,08 – 2,35 µm	Band 7 (shortwave infrared 2) SR

Table 2.3. Band composition of Landsat 5 ETM sensor.

Data were processed to get the least cloudy images by using the quality assessment band (QA), in the script was indicated the dataset selected, the regional boundaries (geometry), and the period of interest, then bands correspondent to Red, Green, and Blue were inserted (Annex B). Then NDVI was calculated and limit for possible output values were restricted to the normal range NDVI can assume (-1 to 1) as showed in Annex B. A graph containing the count of all NDVI values in each pixel was created and values contained in the histogram were available to be downloaded in .csv format. NDVI images of our study region could be exported to Drive and downloaded from there in .tif format. Once the script and the process were set, the interface is very clear and easy to use, you should press the "*Run*" button and automatically appears the map with the mean NDVI layer, in the "*Console*" section you can find the number of images per selected period and the histogram with the pixel count, in the "*Task*" section is possible to export the data in Drive (Figure 2.12).

Name	Units	Scale	Wavelenght	Description
B1		0,0001	0,45 – 0,52 µm	Band 1 (blue) SR
B2		0,0001	0,52 – 0,60 µm	Band 2 (green) SR
B3		0,0001	0,63 – 0,69 µm	Band 3 (red) SR
B4		0,0001	0,77 – 0,90 µm	Band 4 (near infrared) SR
B5		0,0001	1,55 – 1,75 µm	Band 5 (shortwave infrared 1) SR
B6	Kelvin	0,1	10,40 – 12,50 µm	Band 6 brightness temperature
B7		0,0001	2,08 – 2,35 µm	Band 7 (shortwave infrared 2) SR

Table 2.3. Band composition of Landsat 5 ETM sensor

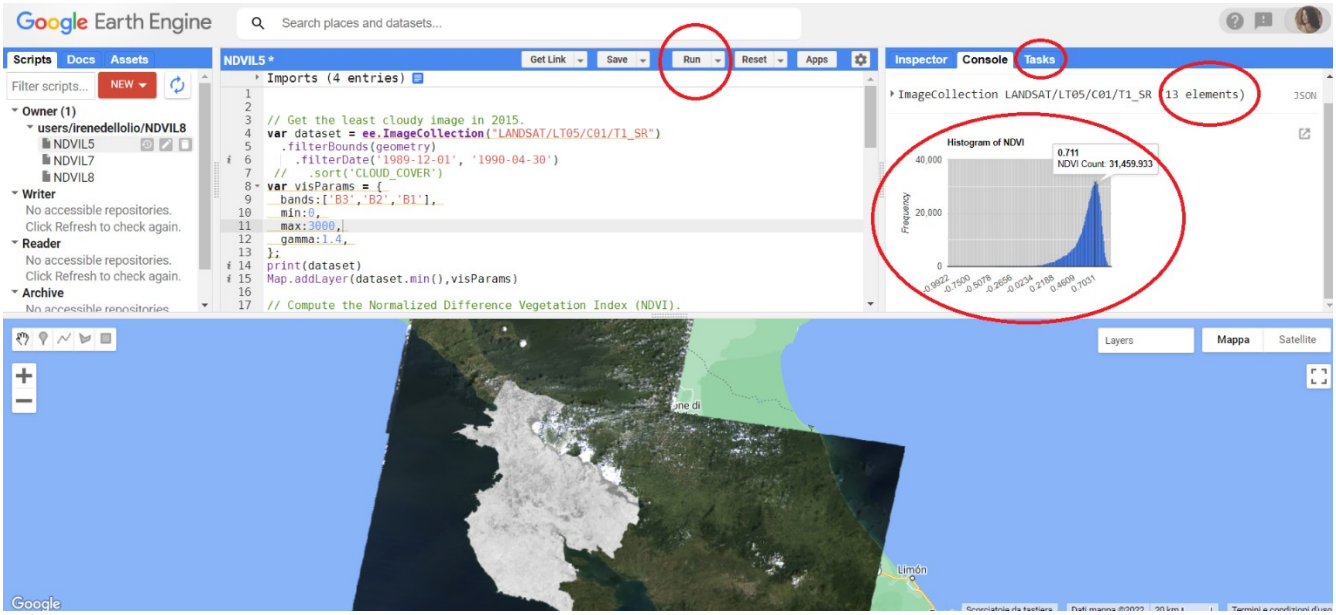

Figure 2.12. Google Earth Engine Code Editor interface

From 2000 to 2014 USGS Landsat 7 Surface Reflectance Tier 1 dataset from Collection 1 was used, which is the atmospherically corrected Surface Reflectance from the Enhanced Thematic Mapper Plus (ETM+) sensor. The Earth Engine Snippet is *ee.ImageCollection*("LANDSAT/LE07/C01/T1_SR").

Images captured by Landsat 7 are composed by (Table 2.4) 4 bands from visible and NIR wavelengths, and 2 SWIR bands with 30m spatial resolution, one TIR band originally with 60m spatial resolution then resamples using cubic convolution to 30m resolution.

Name	Units	Scale	Wavelenght	Description
B1		0,0001	0,45 – 0,52 µm	Band 1 (blue) SR
B2		0,0001	0,52 – 0,60 µm	Band 2 (green) SR
B3		0,0001	0,63 – 0,69 µm	Band 3 (red) SR
B4		0,0001	0,77 – 0,90 µm	Band 4 (near infrared) SR
B5		0,0001	1,55 – 1,75 µm	Band 5 (shortwave infrared 1) SR
B6	Kelvin	0,1	10,40 – 12,50 µm	Band 6 brightness temperature
B7		0,0001	2,08 – 2,35 µm	Band 7 (shortwave infrared 2) SR

Table 2.4. Landsat 7 band composition

The process to extract the information of interest is the same as for Landsat 5, the only change in this case is the initial Snippet to make sure that the Editor accesses the right database, band numbers are the same.

From 2014 to 2021 USGS Landsat 8 Surface Reflectance Tier 1 was used. Data are acquired by the OLI/TIRS sensors and contains (Table 2.5) 5 visible and NIR bands, 2 SWIR bands, one TIR band, and intermediate bands. EE Snippet is *ee.ImageCollection*("LANDSAT/LE07/C01/T1_SR").

Name	**Scale**	**Wavelenght**	**Description**
B1	$2{,}75e^{-05}$	0,435 – 0,451 µm	Band 1 (ultra blue, coastal aerosol) SR
B2	$2{,}75e^{-05}$	0,452 – 0,512 µm	Band 2 (blue) SR
B3	$2{,}75e^{-05}$	0,533 – 0,590 µm	Band 3 (green) SR
B4	$2{,}75e^{-05}$	0,636 – 0,673 µm	Band 4 (red) SR
B5	$2{,}75e^{-05}$	0,851 – 0,879 µm	Band 5 (near infrared) SR
B6	$2{,}75e^{-05}$	1,566 – 1,651 µm	Band 6 (shortwave infrared 1) SR
B7	$2{,}75e^{-05}$	2,107 – 2,294 µm	Band 7 (shortwave infrared 2) SR
B10	0,000341802	10,60 – 11,19 µm	Band 10 surface temperature

Table 2.5. Landsat 8 band composition

The script used to calculate NDVI maps is the same, there is only the need to reformulate the snippet section to make sure that data are downloaded from the right dataset, and the bands' correspondences with RGB colours and NIR, different from Landsat 5 and 7.

2.6.3. NDVI maps quality assessment

Monthly mean NDVI images were processed and downloaded from 1990 to 2021, counted in order to check missing data/months with results and monthly images were divided in dry and wet season (December to April and May to November) for each year (Table 2.6 and Table 2.7).

Year	December (prev. Year)	January	February	March	April	Total
1990	3	4	1	1	4	***13***
1991	0	0	0	4	5	***9***
1992	2	0	0	2	0	***4***
1993	0	0	1	0	0	***1***
1994	0	0	0	0	0	***0***
1995	0	0	0	0	0	***0***
1996	0	0	0	0	0	***0***
1997	6	5	6	6	3	***26***
1998	4	4	3	6	6	***23***
1999	6	4	5	6	4	***25***
2000	0	3	0	2	1	***6***
2001	3	3	1	1	3	***11***
2002	3	0	0	3	4	***10***
2003	4	4	2	0	1	***11***
2004	4	5	3	1	3	***16***
2005	3	3	5	2	3	***16***
2006	5	3	6	3	1	***18***
2007	0	0	4	2	2	***8***
2008	3	3	6	5	3	***20***
2009	8	5	5	5	4	***27***
2010	3	4	2	4	4	***17***
2011	4	3	3	6	0	***16***
2012	6	6	4	3	2	***21***
2013	3	6	3	4	1	***17***
2014	3	6	6	5	3	***23***
2014	5	6	6	6	4	***27***
2015	6	6	4	6	6	***28***
2016	6	6	4	6	6	***28***
2017	4	6	6	6	5	***27***
2018	5	6	5	6	6	***28***
2019	6	5	6	6	6	***29***
2020	6	6	6	6	4	***28***
2021	6	6	4	6	5	***27***

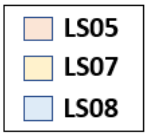

Table 2.6. Monthly available images (dry seasons, from 1990 to 2021)

Year	May	June	July	August	September	October	November	*Totale*
1990	0	0	0	0	0	0	0	***0***
1991	3	6	2	3	0	2	5	***21***
1992	0	0	0	0	0	0	0	***0***
1993	0	0	0	0	0	0	0	***0***
1994	0	0	0	0	0	0	0	***0***
1995	0	0	5	0	0	0	0	***5***
1996	0	2	3	6	3	0	4	***18***
1997	0	0	0	2	0	4	1	***7***
1998	3	2	2	0	4	0	3	***14***
1999	5	5	0	6	2	2	3	***23***
2000	0	1	4	3	4	1	3	***16***
2001	0	1	0	0	3	2	4	***10***
2002	1	2	0	1	3	1	2	***10***
2003	1	0	1	1	0	2	4	***9***
2004	0	0	0	0	3	5	2	***10***
2005	1	1	1	2	3	1	2	***11***
2006	1	1	0	0	2	4	1	***9***
2007	1	0	1	2	2	4	2	***12***
2008	0	0	1	1	1	4	1	***8***
2009	3	1	0	1	3	4	4	***16***
2010	3	1	1	0	1	4	3	***13***
2011	2	0	0	2	4	3	3	***14***
2012	2	0	0	0	2	1	2	***7***
2013	1	0	1	2	1	4	4	***13***
2014	3	2	2	1	3	3	5	***19***
2014	6	6	6	6	5	4	6	***39***
2015	6	6	3	6	6	6	6	***39***
2016	5	3	4	5	5	6	3	***31***
2017	4	3	6	5	6	3	6	***33***
2018	5	5	5	4	6	3	6	***34***
2019	6	4	5	5	6	5	4	***35***
2020	6	5	5	5	5	5	5	***36***
2021	5	5	5	3	5	6	6	***35***

LS05
LS07
LS08

Table 2.7. Monthly available images (wet seasons, from 1990 to 2021)

Seasonal multitemporal mean NDVI images were downloaded from GEE Code Editor and processed in ArcMap to have a clearer visualization of mean NDVI values. Even if the use of satellites, and more than any other for the aim this study, is one of the best methods to observe extended areas' changes over time, they have limitations, especially if we look to older Landsat 5 and Landsat 7. In this case limitations were missing data for long periods of time, e.g., in Landsat 5 were not available 1990 dry season, and from 1992 to 1996 dry season almost no data at all, incomplete and cloudy images. The latter was in part overcame with the use of the quality assessment (QA) band, and the minimum composite of multiple images was adopted to generate the optimal image.

Figure 2.13 and Figure 2.14 show the most cloudy and damaged multitemporal images for the wet and the dry seasons of the selected time period, annual damaged or cloudy images were not included because we can explain unusual annual mean NDVI values by looking at seasonal anomalies.

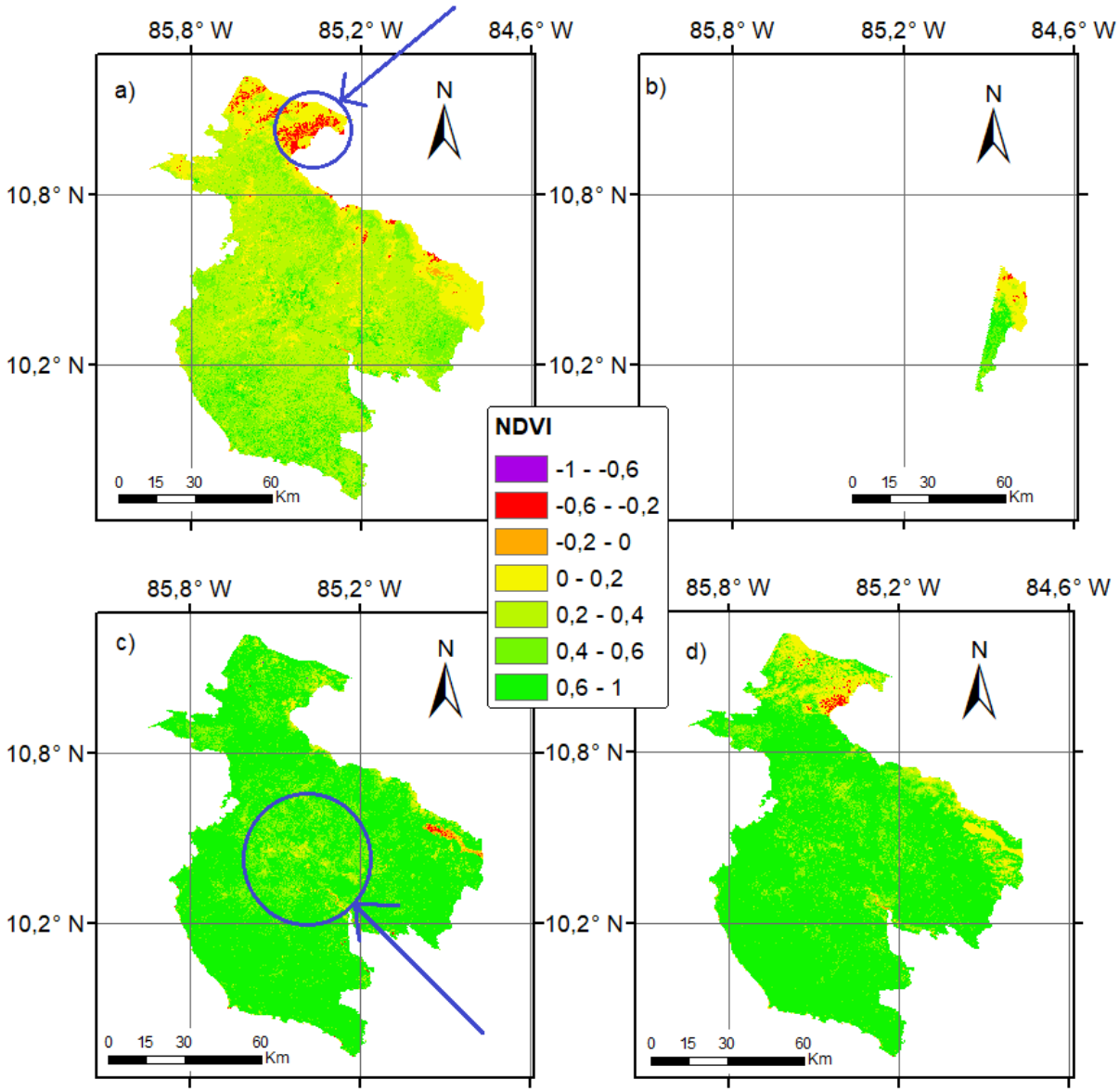

Figure 2.13. Landsat 5 cloudy or images. a) dry season of 1992; b) dry season of 1993; c) wet season of 1996; d) wet season of 1997

Clouds represent an issue for this analysis, especially when we are observing mean regional NDVI changes over time. Mean NDVI will be too compromised because clouds assume very low values, Landsat 5 NDVI calculations show a clear example of this is Figure 2.13a, even with the QA band and the minimum composite of multiple images, clouds were still clearly visible. This problem is very common since in the North-west and the Northern part of the region clouds are persistent because of the presence of the Guanacaste Mountain range and that for the dry season of 1992 only for images in five months were available, not allowing cloud masking. The dry season of 1993 (Figure 2.13b) is almost totally missing, the image was represented to show that sometimes available images does not cover all regional surface. Figure 2.13c represents the mean NDVI value for

the wet season of 1996, image seem to be complete, also, by looking at Table 2.7 the number of images could appear sufficient to obtain a clear image but the yellow alone is not and index of vegetation stress but a thin cloud layer together with cloud shadow. This is very common during the wet season because it rains almost every day.

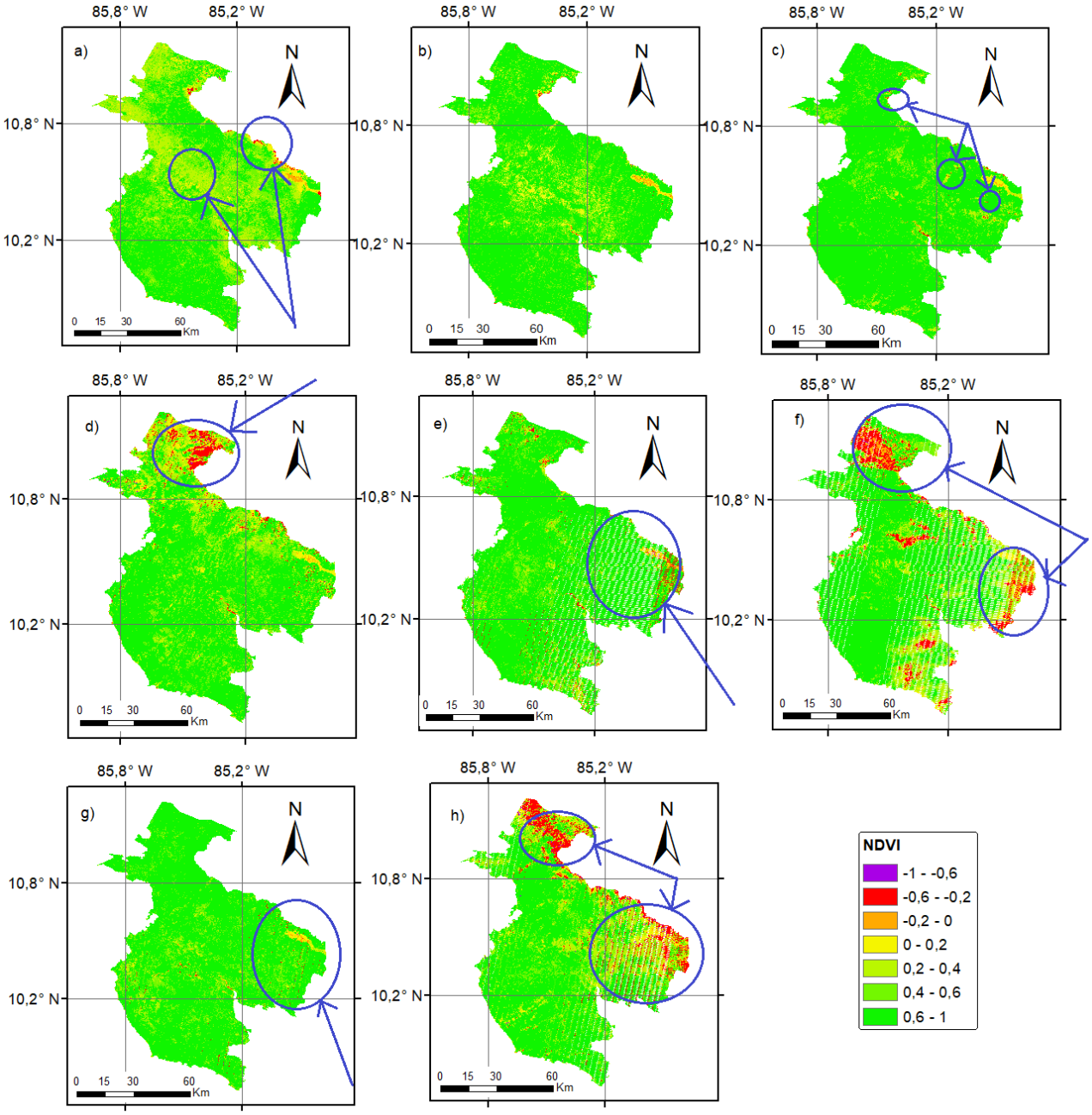

Figure 2.14. Landsat 7 most damaged or cloudy images. a) dry season of 2002; b)2004 dry season; c)2000 wet season; d)2003 wet season; e) wet season of 2004; f) wet season of 2008; g) wet season of 2010; h) wet season of 2012.

Evaluating Landsat 7, the database was more consistent and there were no missing years. Images from ETM+ sensor, in addition to cloud and cloud shadow disturbances, from the second half of 2003, after the Scan Line Corrector failure, all images were compromised, and so mean NDVI values are not the correct ones. Figure 2.14 shows the Landsat 7 most damaged and cloudy images from 2000 to 2014. Wet season calculations showed more obvious disturbances and clouds compared to dry seasons. It is important to note that even if sometimes the problems caused by the SLC failure seem masked as in Figure 2.14b showing mean NDVI for the dry season of 2004, if you zoom in the image, the damage will be clearly recognizable for every image since 2004 (Figure 2.15). Most consistent disturbance is obvious in the Southwest part of the region.

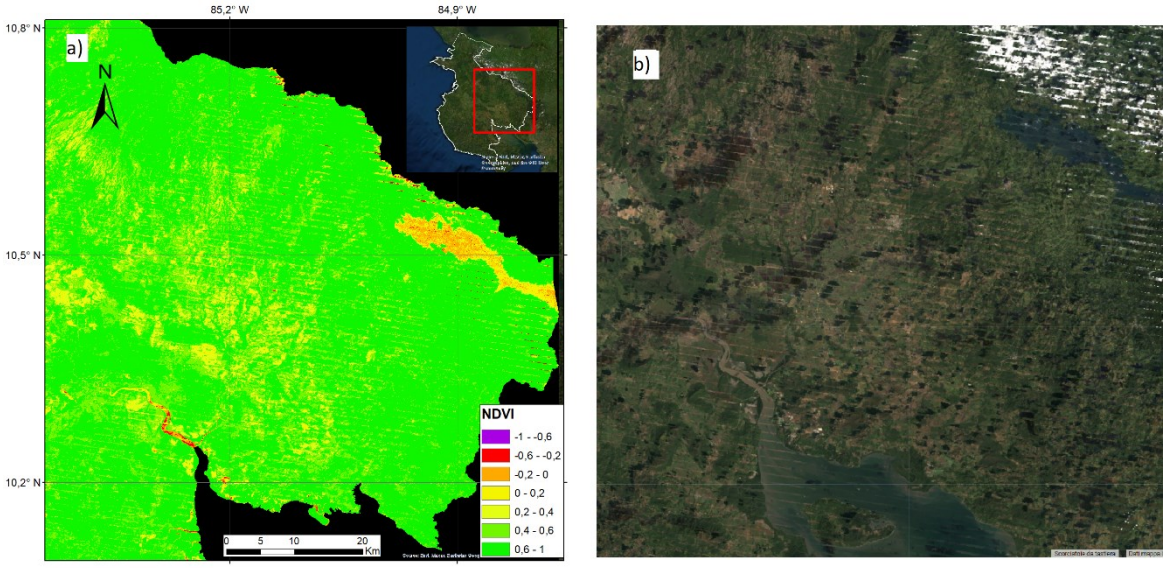

Figure 2.15. A section of the region zoomed in of the dry season of 2004. a) mean NDVI b) screenshot from Google Earth Explorer

For Landsat 8, conditions were overall clear and the dataset complete from 2014 to 2020, with clear, cloud free and complete images.

2.7. Land Cover Maps

Many land cover datasets were developed over the years, but global ones have very low resolution, not suitable for many studies and for small areas such as our study region or higher resolution databases do not cover all the globe, or they cover just a short period of time. To overcome these problems, China started to develop a 30-m resolution Global Land Cover in 2010 (Chen & Chen, 2018). In 2010, 30m spatial resolution global land cover maps of 2000 and 2010 were launched under the name of GlobeLand30 and donated to the United Nations to be distributed as a free access resource, with further improvements the maps arrived to reach an accuracy of 83% in the definition of the ten land cover classes (Chen & Chen, 2018). The ten classes (Table 2.8)

are Cultivated land, Forest, Grassland, Shrubland, Wetland, Water bodies, Tundra, Artificial surfaces, and bare soil.

Code	Class Name	Class Description
10	Cultivated land	Arable land (cropland): dry land, paddy field, land for greenhouses, vegetable fields, artificial tame pastures, economic cropland in which shrub crops or herbaceous crops are planted, and land abandoned with the reclamation of arable land
20	Forest	Broadleaved deciduous forest, evergreen broad-leaf forest, deciduous coniferous forest, evergreen coniferous forest, mixed broadleaf-conifer forest
30	Grassland	Typical grassland, meadow grassland, alpine grassland, desert grassland, grass
40	Shrubland	Desert scrub, mountain scrub, deciduous and evergreen shrubs
50	Wetland	Lake swamp, river flooding wetlands, seamarsh, shrub/forest wetlands, mangrove forest, tidal flats/salt marshes
60	Water bodies	Open water, i.e., lakes, reservoirs/fishponds, rivers
70	Tundra	Brush tundra, poaceae tundra, wet tundra, bare tundra, mixed tundra
80	Artificial surfaces	Settlement place, industrial and mining area, traffic facilities
90	Bareland	Saline-alkali land, sand, gravel, rock, microbiotic crust
100	Permanent snow/ice	Permanent snow, ice sheet and glaciers

Table 2.8. GlobeLand30 Classification

Land cover maps of 2000, 2010 and 2020 were downloaded in .tif format from GlobeLand30 website (http://www.globeland30.org/home_en.html). This dataset was developed by using Landsat, HJ-1 (China Environment and Disaster Reduction Satellite), and the 16-meter resolution GF-1 (China High Resolution Satellite). Maps were uploaded in ArcMap (Figure 2.16) and the land cover type of interest was extracted (i.e., cropland) for the three years (2000, 2010, 2020).

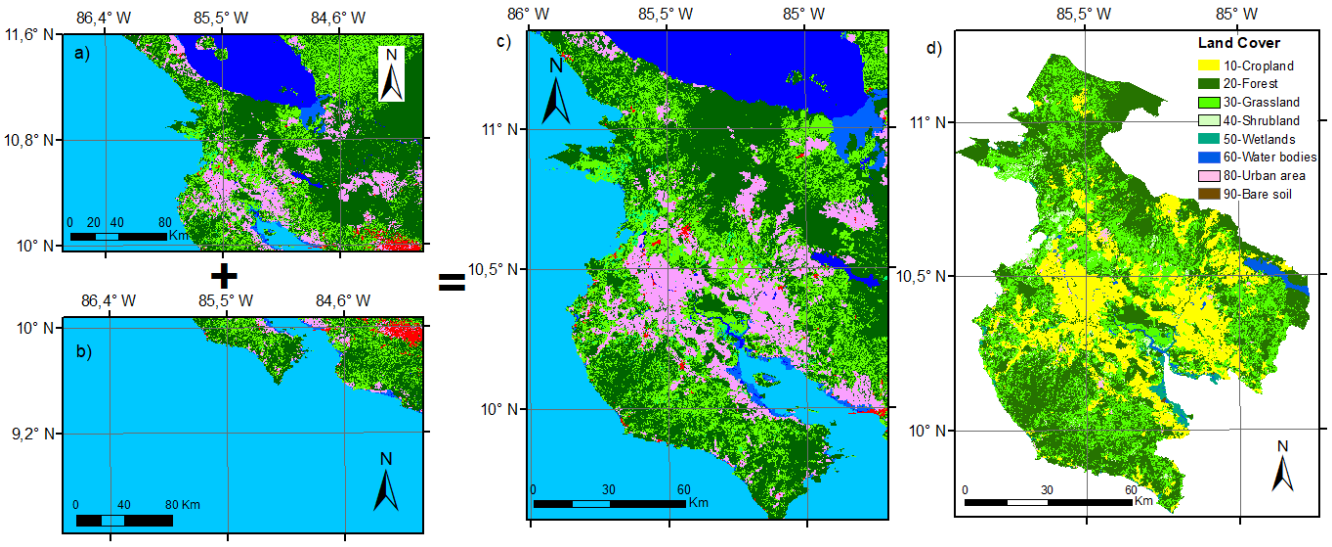

Figure 2.16. GlobeLand30 raster dataset of 2020 processed in ArcMap. a) Northern section of the Chorotega region; b) Southern portion of the Chorotega region; c) Merged sections; d) Clipped image with regional boundaries.

The area of the Chorotega region occupy two quadrants of the global dataset (Figure 2.16a and Figure 2.16b) which were united by using the "Mosaic to new raster" tool in ArcMap toolbox to create a single continuous map (Figure 2.16c). Then the figure was cut by using the "Extract by Mask" tool inside the regional boundaries, symbology was adjusted to have a better display of different land covers (Figure 2.16d). Figure 2.16 shows the process for GlobeLand30 map of 2020, the same methodology was applied for 2000 and 2010 global land cover maps (Figure 2.17).

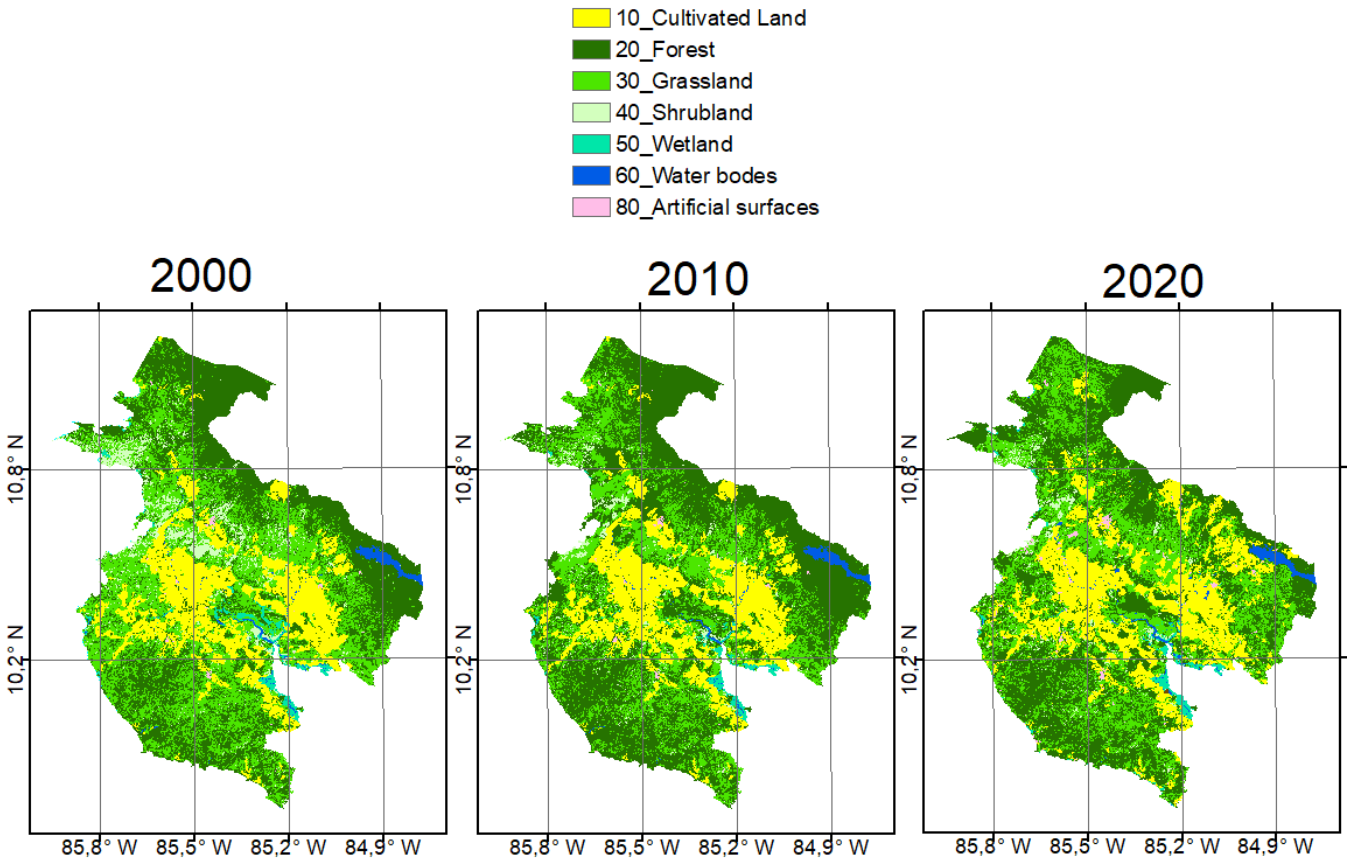

Figure 2.17. Land Cover Change maps re-elaborated from GlobeLand30 database of the Chorotega region.

Then cropland area of 2000 and 2020 was divided from the other land cover classes. Cropland area of 2000 was used to analyse the impact of El Niño 1997-1998 on cultivated land and cropland area of 2020 was used to analyse the impact of El Niño event of 2015-2016. The impacts of El Niño 1997-1998 was so severe that impacts were still present after 1-2 years. In the case of the 2015-2016 event, it is worth to notice that the drought after that event was prolonged even until 2019, so data for 2020 still contains the impacts of the severe and prolonged drought.

2.8. NDVI time series

From GEE Code Editor was possible to generate histogram charts by writing the formula in the script (Annex B) showing the pixel count for each NDVI value (Figure 2.18) calculated inside regional boundaries and data in .csv format can be downloaded, in order to be able to process them in Excel.

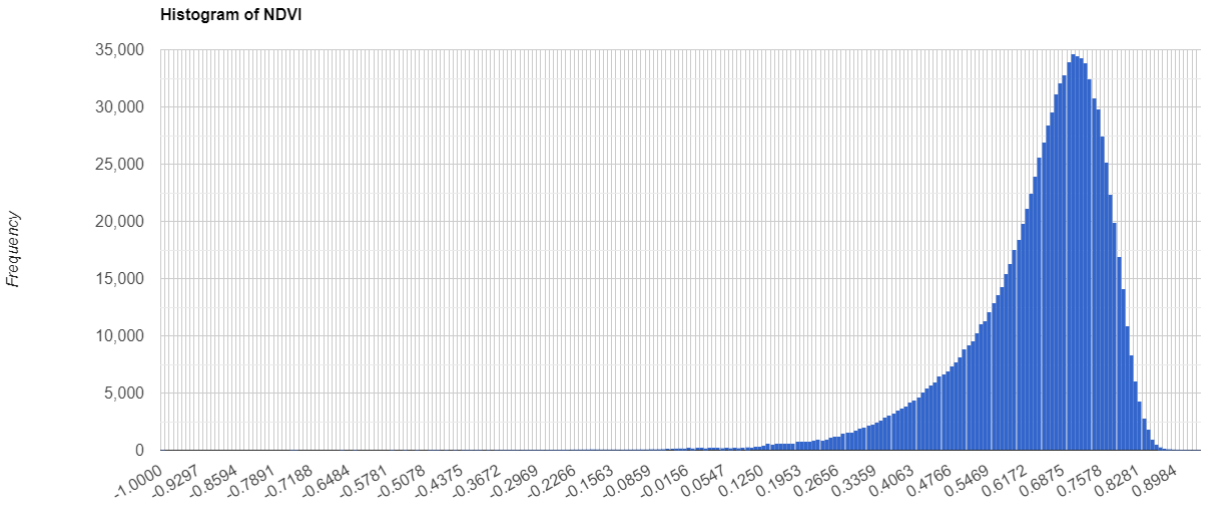

Figure 2.18. Histogram of NDVI, mean annual values for 1997 in the Chorotega region

The .csv files downloaded from GEE platform were imported in Excel, data had to be reorganized with the "Data to Columns" tool. The two columns containing Band values and the pixel Counts were multiplied. The total NDVI value divided by the number of pixels gave the mean NDVI value for the period considered. The procedure was followed for Landsat 5, 7 and 8 for calculating mean NDVI values from 1990 to 2021, for dry seasons, wet seasons, and the whole year. To obtain mean annual NDVI foe each year dry and wet season mean NDVI was summed and divided by two. Graphs representing time series of mean NDVI were created and divided by satellite from which data were derived in order to have a clear idea of NDVI course over the years and during El Niño, compare them with precipitation charts to individuate critical periods, and check for an eventual correlation and/or trend between precipitation and NDVI.

Trend analysis in Microsoft Excel were made for both precipitation and NDVI charts. In Microsoft Excel is possible to add a trendline in the chart, its formula and the R-squared value, in this study was chosen the linear regression as a statistical method to show the relationship between years and mean NDVI values.

R-squared value is calculated through the Regression function in the Data Analysis section in Excel, the input Y range will be filled with the mean NDVI values and in the in input X range will be placed the years, the output of the regression analysis shows the R-square value in the Regression Statistics section, which basically indicates how much the change of mean NDVI values depends on the passing of the years, and the p-value in the Analysis of Variance (ANOVA) section. The p-value ranges from 0 to 1 and shows the statistical significance of the test, if $p<0,05$ data is significant, in this case does exist a correlation between the passing of the years and NDVI change.

2.9. Image processing in ArcMap

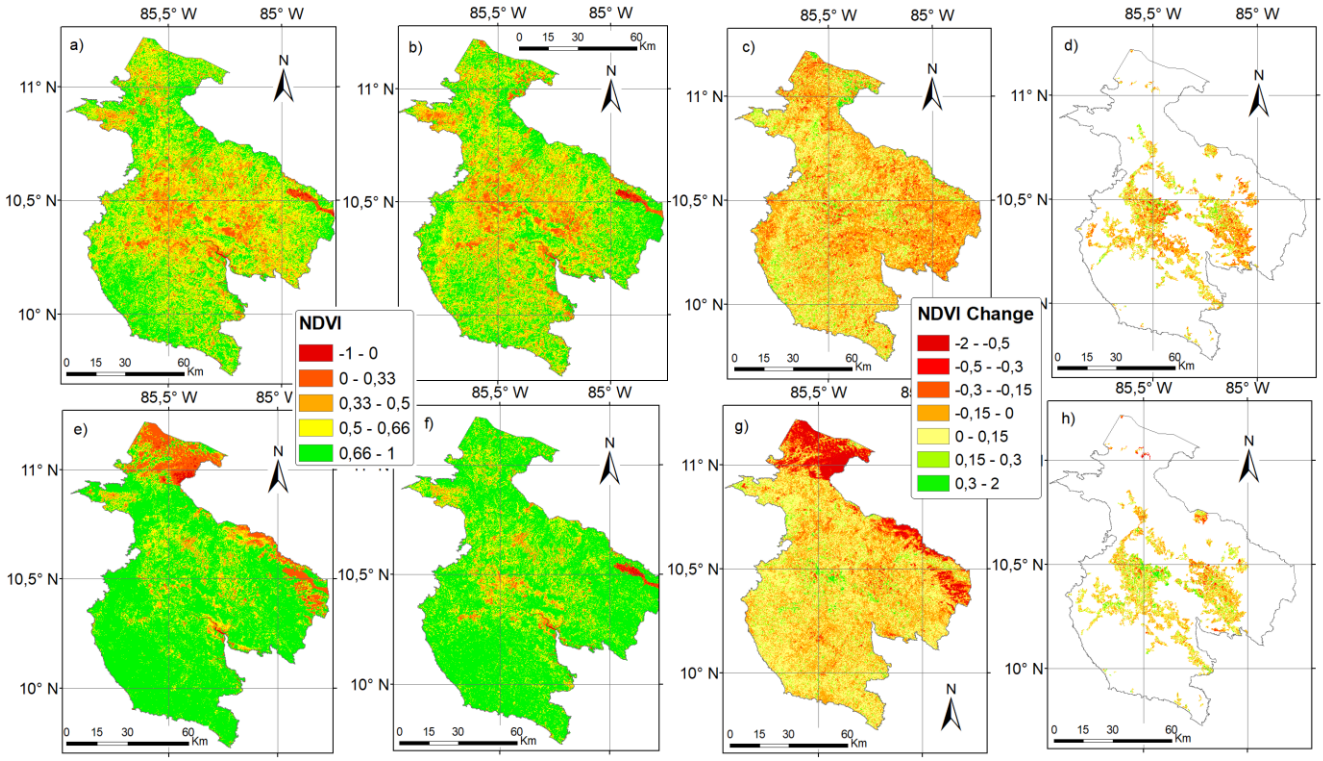

Figure 2.19. a) mean NDVI of the dry season of 1997; b) mean NDVI of the dry season of 1999; c) NDVI change for the dry season of the 1997-1998 event; d) NDVI change during the dry season of the 1997-1998 event in cropland area; e) mean wet season NDVI of 1997; f) mean wet season NDVI of 1999; g) NDVI change during wet season of the 1997-1998 event; h) NDVI change during the wet season of the 1997-1998 event in cropland area.

NDVI values from lower than 0 indicate inanimate objects, dead plants, and dry soil. Values from 0 to 0,33 indicate unhealthy plants, 0,33 to 0,5 moderately unhealthy plants, 0,5 to 0,66 moderately healthy plant, and 0,66 to 1 shows healthy plants. NDVI change during dry and wet seasons in the middle of 1997-1998 event was calculated with the use of Raster Calculator tool in ArcMap:

- For the dry season of the 1997-1998 event (Figure 2.19c), mean NDVI during the dry season of 1999 (outside El Niño event, Figure 2.19b) was subtracted from mean NDVI of the dry season on 1997 (in the mid of El Niño event, Figure 2.19a).
- Cropland area of 2000 from GlobeLand30 dataset was used to display NDVI change in cropland area during 1997-1998 event during dry season (Figure 2.19d).
- For the wet season of the 1997-1998 event (Figure 2.19g), the difference between mean NDVI of the wet season of 1997 (Figure 2.19f) and the wet season of 1999 (Figure 2.19e) was calculated.
- Cropland area of 2000 from GlobeLand30 dataset was used to display NDVI change in cropland area during 1997-1998 event during wet season (Figure 2.19h).

- Values for both wet and dry seasons NDVI change of 1997-1998 event were then reclassified in order to count the number of pixels corresponding to every range of difference of NDVI.

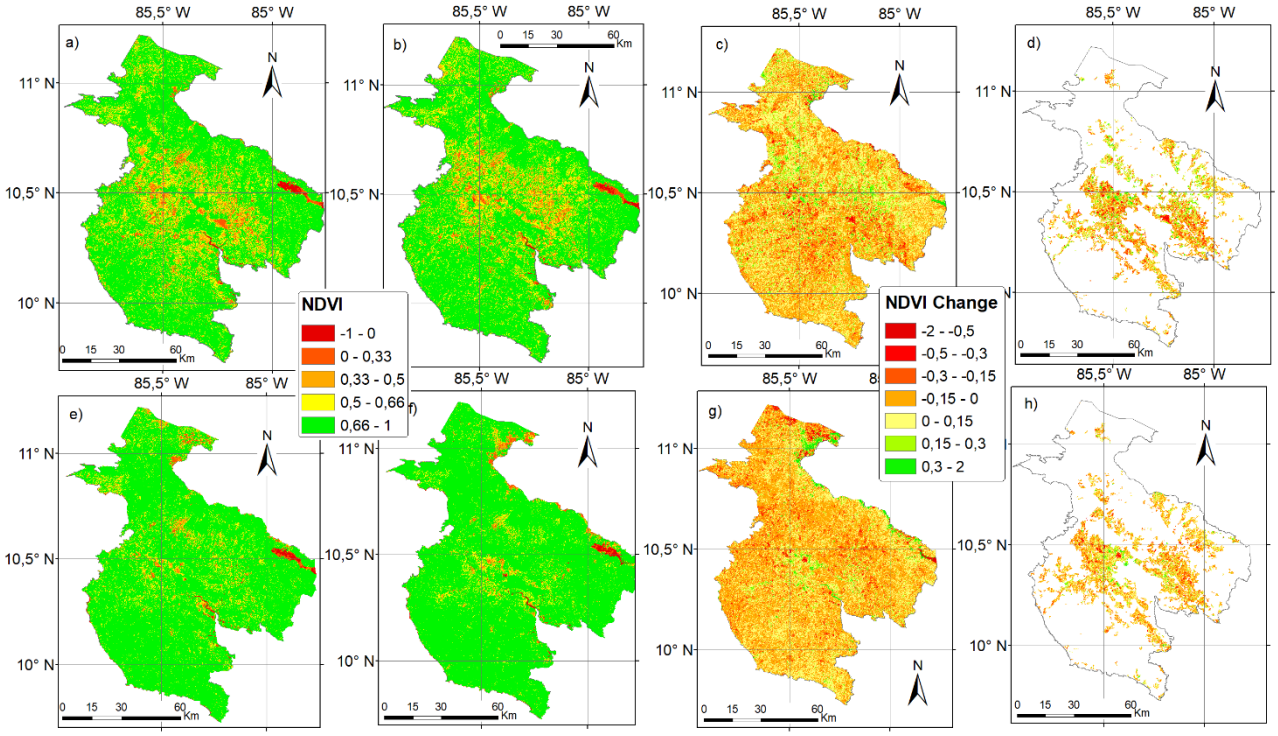

Figure 2.20. a) mean NDVI of the dry season of 2015; b) mean NDVI of the dry season of 2017; c) NDVI change for the dry season of the 2015-2017 event; d) NDVI change during the dry season of the 2015-2017 event in cropland area; e) mean wet season NDVI of 2015; f) mean wet season NDVI of 2017; g) NDVI change during wet season of the 2015-2017 event; h) NDVI change during the wet season of the 2015-2017 event in cropland area.

NDVI change during dry and wet seasons in the middle of 2015-2016 event was calculated with the use of Raster Calculator tool in ArcMap:

- For the dry season of the 2015-2016 event (Figure 2.20c), dry season mean NDVI of 2017 (outside the event, Figure 2.20b) was subtracted from dry season cropland area mean NDVI of 2015 (during the event, Figure 2.20a)
- Cropland area of 2020 from GlobeLand30 dataset was used to display NDVI change in cropland area during 2015-2016 event during dry season (Figure 2.20d).
- The difference between wet season mean NDVI of 2015 (Figure 2.20e) and wet season cropland area mean NDVI of 2017 (Figure 2.20f) was computed to observe NDVI change during the wet season of the 2015-2016 event (Figure 2.20g).
- Cropland area of 2020 from GlobeLand30 dataset was used to display NDVI change in cropland area during 2015-2016 event during wet season (Figure 2.20h).

- Values for both wet and dry seasons NDVI change of 2015-2016 event were then reclassified in order to count the number of pixels corresponding to every range of mean NDVI difference.

3. Results

3.1. Most significant events

For the analysis period the most intense El Niño events occurred in 1997-1998 and 2015-2016 even though they were not the only ones since 1990. SST positive anomalies indicate the occurrence of the phenomenon in 1991-1992, 2002-2003 and 2009-2010. Apart from that, less pronounced but still present SST anomalies are observable in 1993, in 1995, between 2006-2007 and 2012. According to the ENSO monitoring bulletin of the IMN (https://www.imn.ac.cr/en/boletin-enos) and to more recent measurements, an important El Niño event took place in 2018-2019, which contributed to conditions for a prolonged drought (2015-2019, Pascale et al., 2021)

The exact month of beginning and ending of the event differs according to the source examined, so information on the development of the events from the National Meteorological Institute, NOAA indices, and NASA information were combined.

For the 1997-1998 event starting period was set for the first trimester of 1997 and ending period for the second trimester of 1998 (Figure 3.1a). El Niño 2015-2016 event lasted more than any other before, it started the third trimester of 2014 and ended the second trimester of 2016 (Figure 3.1b).

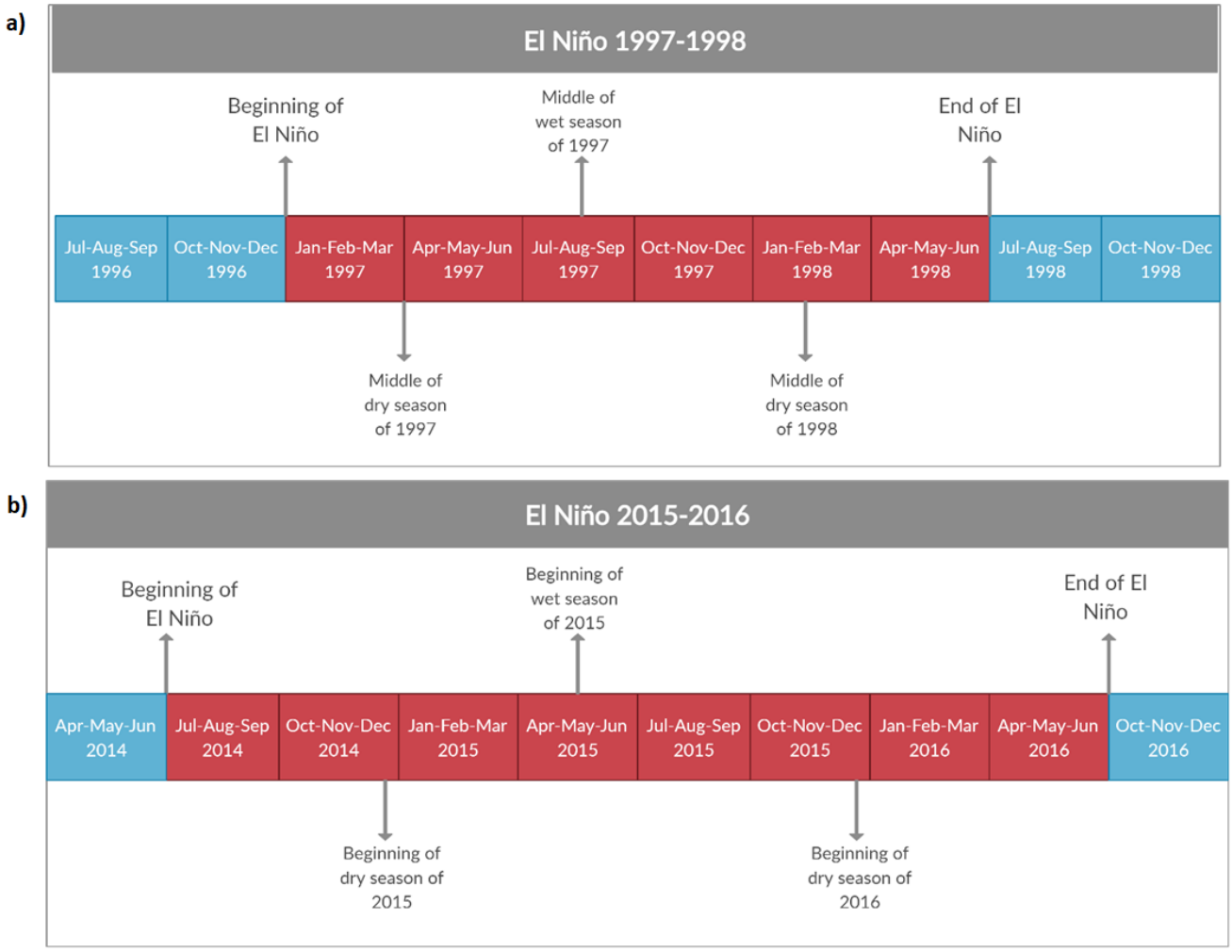

Figure 3.1. Most significant El Niño events timelines. a) 1997-1998 event; b) 2015-2016 event.

3.2. El Niño influence on NDVI

The behaviour of NDVI in regional cropland area during El Niño event was analysed for the dry and the wet season, and the whole year in the most affected period.

3.2.1. Dry season NDVI

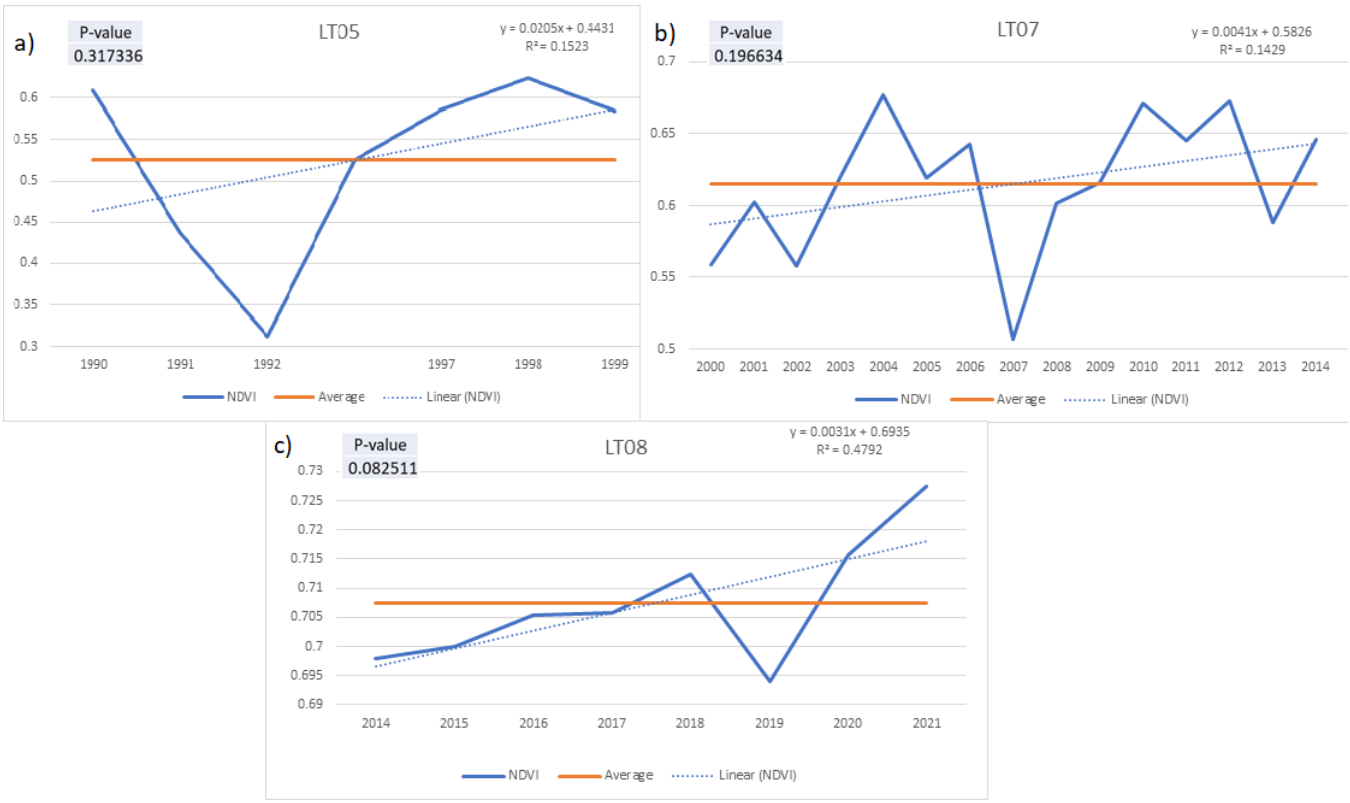

Figure 3.2. Regional dry season mean NDVI. a) Landsat 5 from 1990 to 1999; b) Landsat 7 from 2000 to 2014; c) Landsat 8 from 2014 to 2021.

The regional dry season mean NDVI (Figure 3.2) was determined to increase over the years based on the used satellites, however only Landsat 5 trend was statistically significant.

- Albeit for Landsat 5 (Figure 3.3), few images were available from 1990 to 1992 dry seasons, a drop in NDVI values was identified, which can be explained by the occurrence of a strong El Niño in 1991-1992, vegetation is negatively affected in the entire regional surface. During dry season of 1997, in the middle of 1997-1998 event, NDVI decreases between consecutive years, the most affected areas are the central ones where crops are concentrated. 1990 and 1999 dry seasons show similar spatial distribution of NDVI but with a visible increase in stress in the northern part of the region.

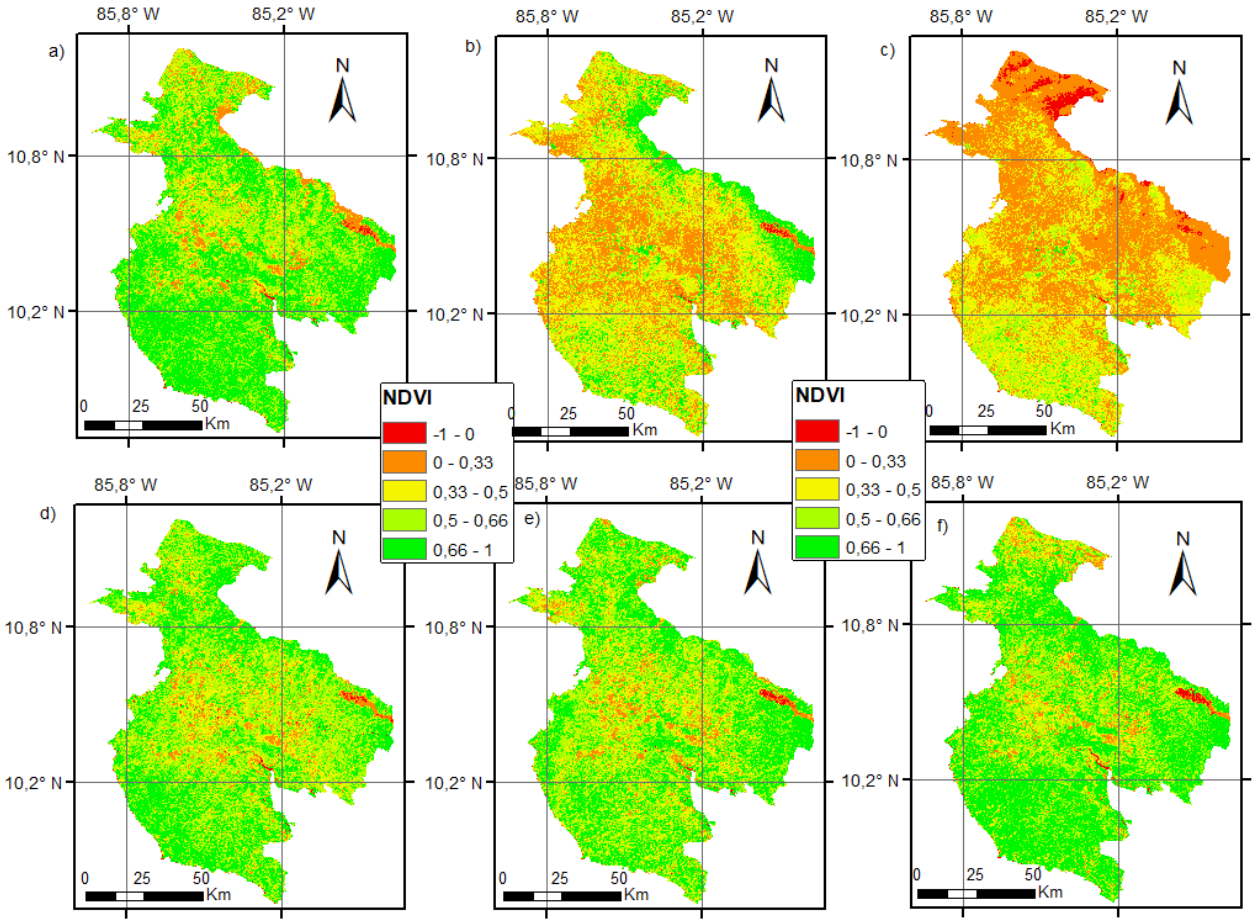

Figure 3.3. Landsat 5 dry seasons NDVI maps from 1990 to 1999. a)1990; b)1991; c)1992; d)1997; e)1998; f)1999

- For Landsat 7 (Figure 3.4), lower peaks were observed for 2002 and 2007, the 2002 low peak during the dry season is attributed to cloud interference (Figure 2.14a) but also by the damaged caused in the region by hurricane Michelle (Vallejos Vásquez et al., 2012), 2007 and 2008 saw a strong la Niña event and strong tropical storm (Vallejos Vásquez et al., 2012) which could have caused negative vegetation response. All imagery shows vegetation stress in the central part of the region, only 2002 (Figure 3.4c),

2005 (Figure 4.3f), 2007 (Figure 4.3h) and 2008 (Figure 4.3i) show a propagation of the stress to the north-west.

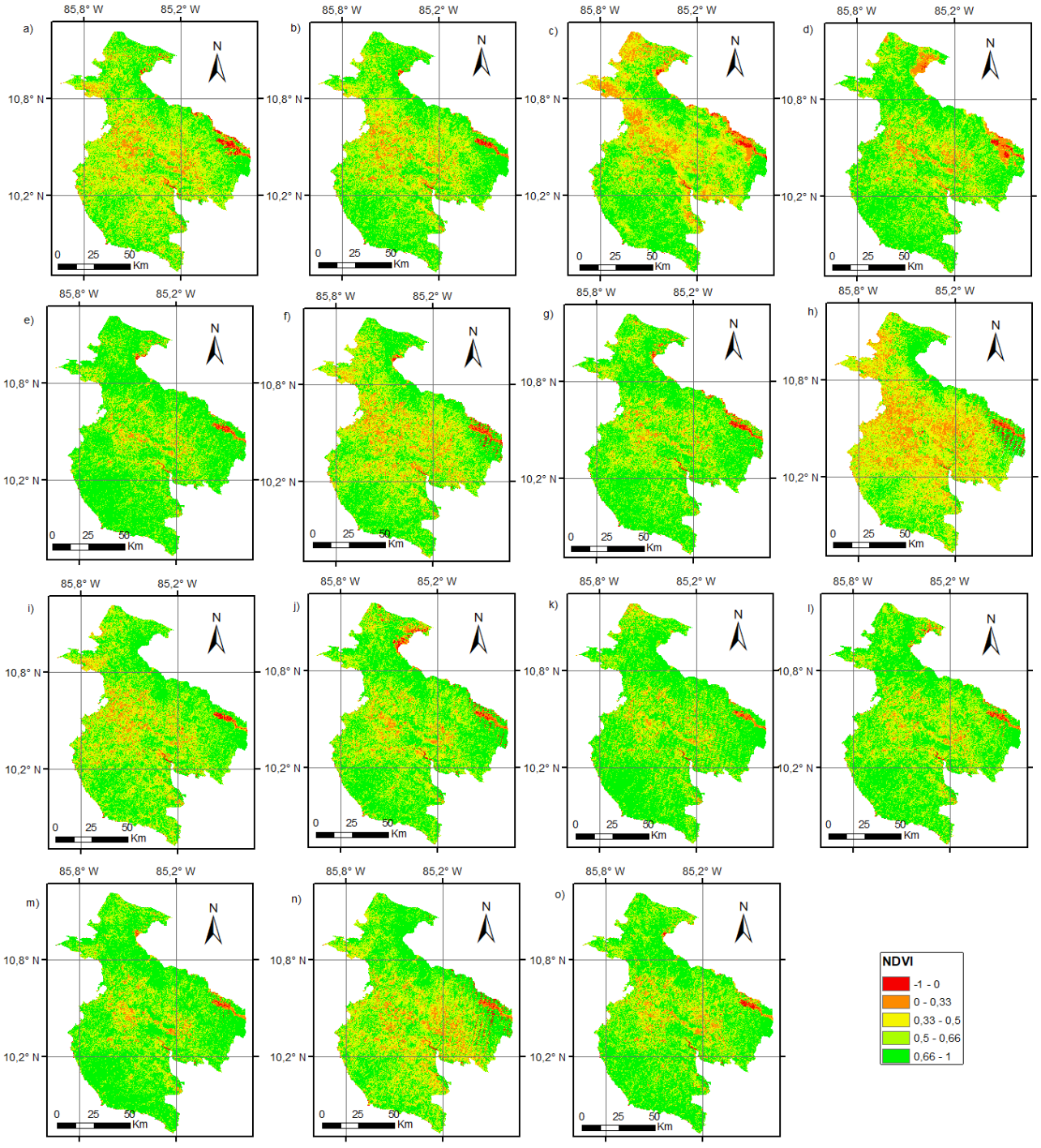

Figure 3.4. Dry season regional mean NDVI images from Landsat 7 from a)2000; b)2001; c) 2002; d) 2003; e) 2004; f) 2005; g) 2006; h) 2007; i) 2008; j)2009; k) 2010; l)2011; m) 2012; n) 2013; o) 2014

- Landsat 8 data imagery (Figure 3.5) showed clear drops of mean NDVI value from 2014 to 2017, consistent with the affectations associated to the severe El Niño event, the NDVI values drop was also observed for the dry season of 2019 in concomitance with following weaker El Niño conditions that allowed the prolongation of the of the drought conditions in the region which extended between 2015 and 2019. The reduction of the NDVI values reduction for 2019 is higher, aspect that is highlighted as can be associated with a stronger response of the vegetation which had slim chances to recover after the extended drought conditions. This aspect is relevant as it motivates further studies such as evaluations of the soil water content conditions as under the circumstances in which the 2015-2019 drought occurred, the propagation of the drought was favoured, meaning a more pronounced impact across the

hydrological cycle. All the years show a concentration of vegetation stress in the lowlands in the centre of the region.

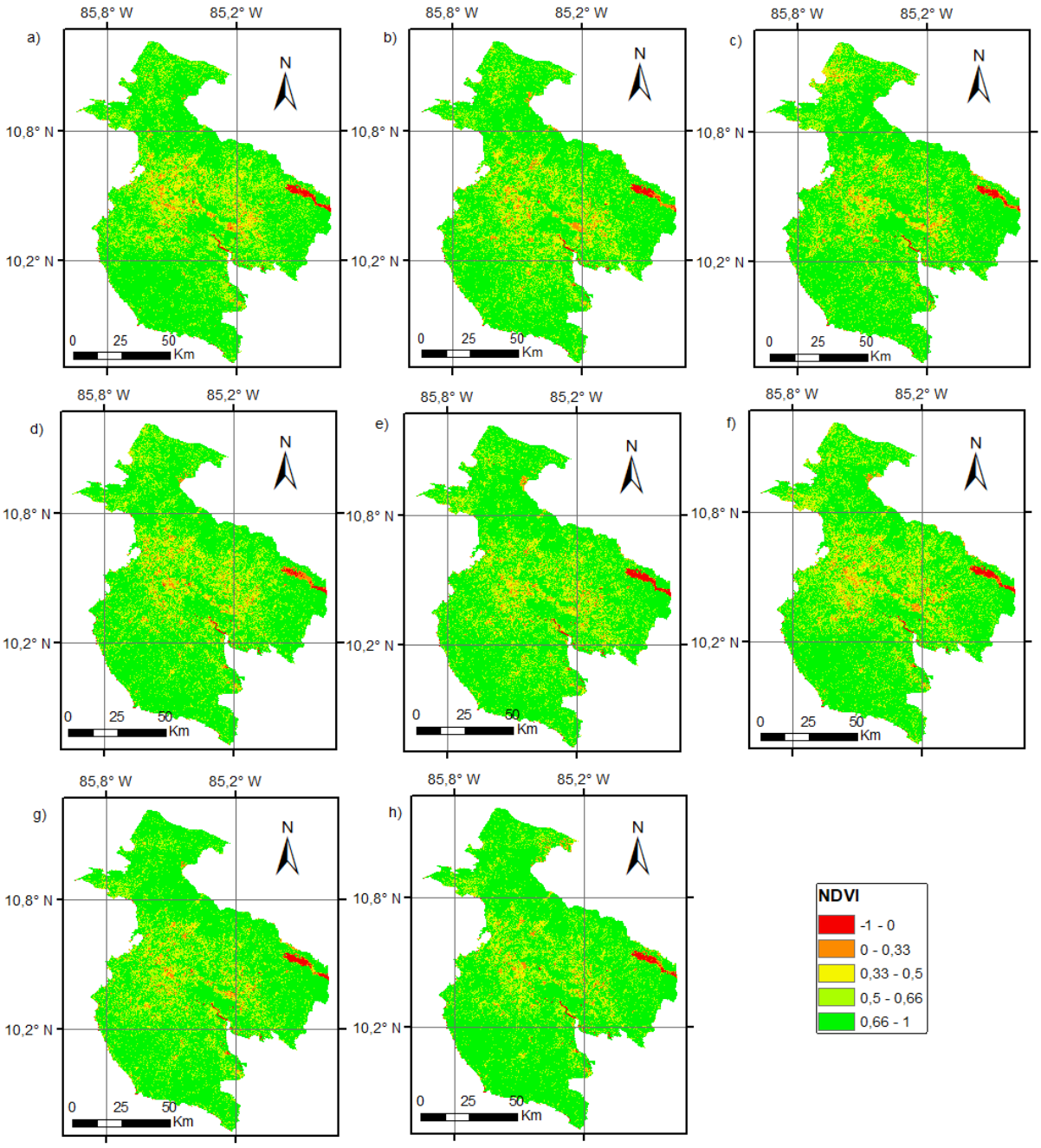

Figure 3.5. Landsat 8 dry season mean NDVI images. a) 2014; b) 2015; c) 2016; d) 2017; e) 2018; f) 2019; g) 2020; h) 2021

3.2.2. Wet season NDVI

Figure 3.6. Wet season mean NDVI charts from 1990 to 2021. a) Landsat 5; b)Landsat 7; c) Landsat 8

Mean NDVI values during the wet season (Figure 3.6) showed higher overall values compared with dry season, consistent with the abundance of rainfall typical of the wet season. For these periods the cloud masking is more common in the data because of the almost permanent cloud cover characteristic of the rainfall systems during the wet season. The slight increasing trend of the mean NDVI is statistically significant only for Landsat 5.

- Based on Landsat 5 imagery (Figure 3.7) for the wet seasons, the representation of the period between 1992 and 1995, excluding 1991 which had a consistent number of images, it was not possible because of missing, cloudy, or damaged data. During 1991, even the wet season showed a NDVI drop that can be related with the El Niño conditions of the 1991-1992 period that has spread across the entire surface of the region. In 1997 wet season mean NDVI value slightly decreases in response to the most important El Niño event, however, by looking at Figure 3.7c, it is possible to note that the drop in NDVI value is worsened by cloud presence in the northeast side of the region, the presence of cloudiness under the conditions that dominated the period for this case may have altered the surface fluxes and increased the atmospheric demand, which could potentially enhanced drought conditions due to surface water loss. According to the p-value NDVI values have a significant positive trend, which is explained by the dry years at the beginning of the series which lower initial NDVI values. All years show stress concentrated in the plains in the centre of the region, in the 1997 and 1998 images there are clouds in the northern part.

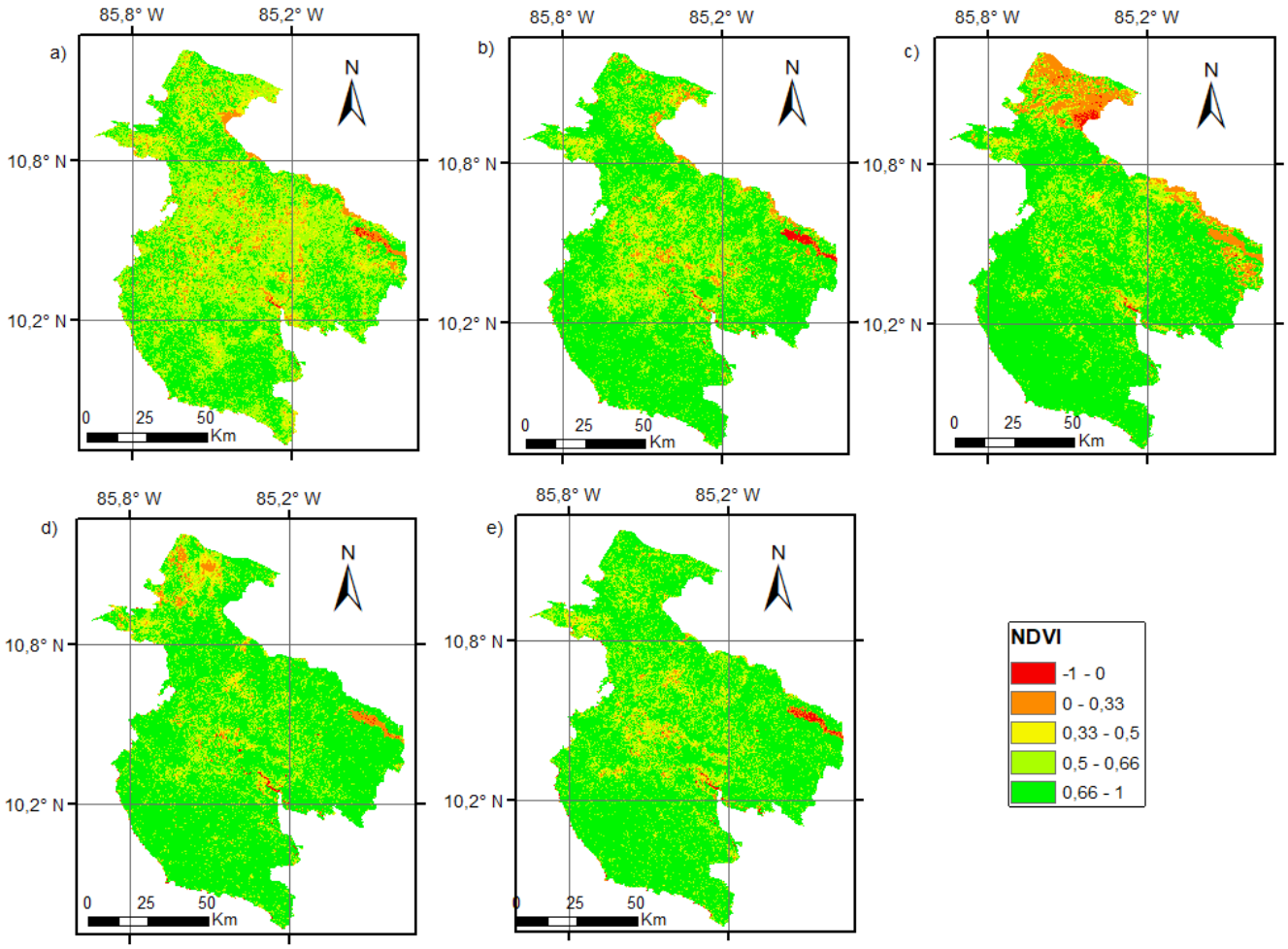

Figure 3.7. LT05 wet season regional mean NDVI. a) 1991; b)1996; c)1997; d)1998; e)1999

- From Landsat 7 imagery (Figure 3.8), a drop in 2003 is observes, in this case the drop corresponds to strong cloud disturbance, while the drop in 2007 is less pronounced than in the dry season but still visible. Information for 2008 and 2012 cannot be properly interpreted for the wet season due to high cloudiness conditions and damaged imagery (Figure 3.8i and Figure 3.8m). If we exclude the damaged and cloud-covered images usually in the east or north (the images from 2003, 2008 and 2012 being the most compromised), low NDVI values are concentrated in the central part of the region.

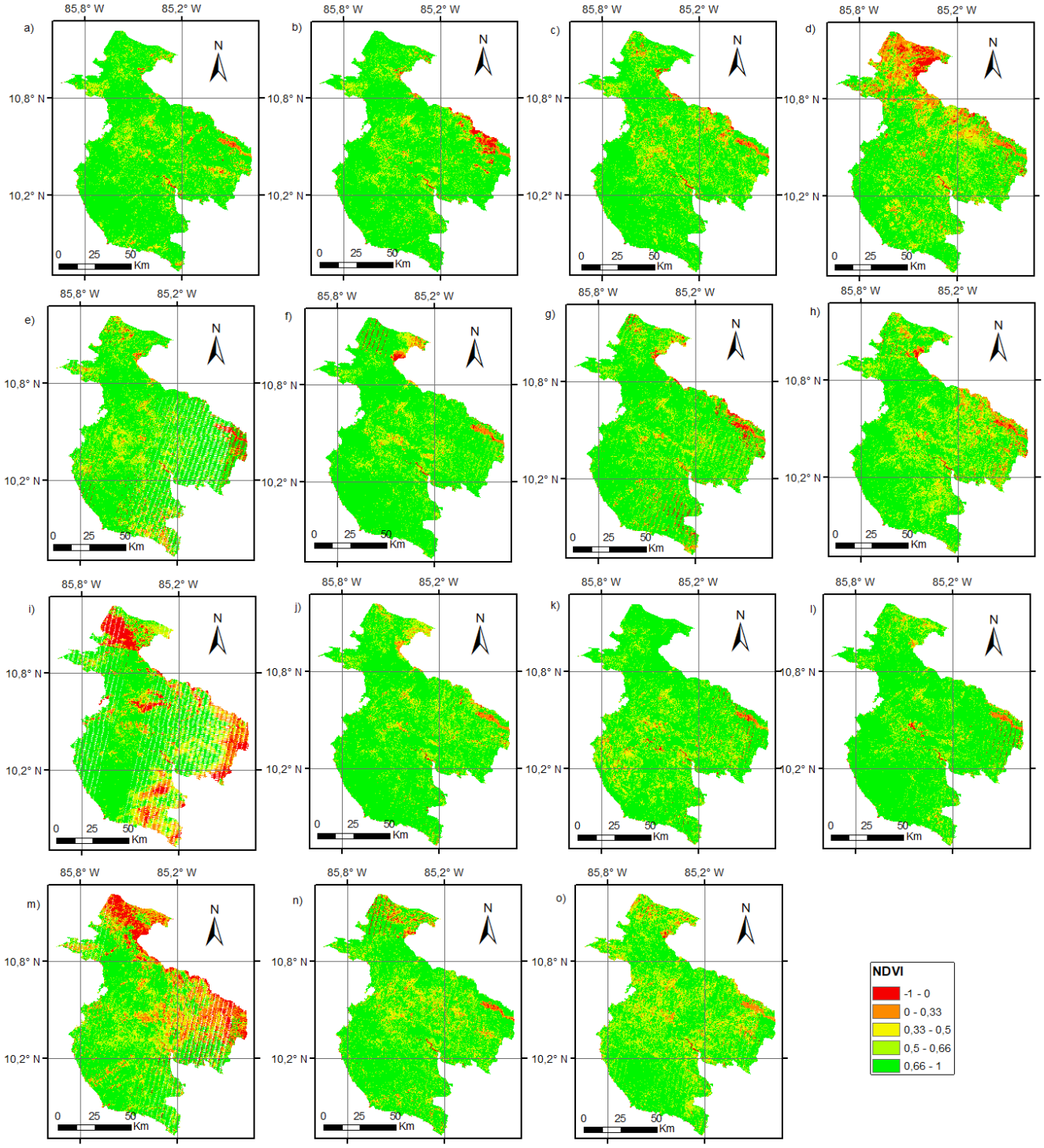

Figure 3.8. wet season mean NDVI maps from Landsat 7. a) 2000; b) 2001; c) 2002; d) 2003; e) 2004; f) 2005; g) 2006; h) 2007; i) 2008; j) 2009; k) 2010; l) 2011; m) 2012; n) 2013; o) 2014

- Mean NDVI values from Landsat 8 (Figure 3.9) suggest a marked negative impact on regional vegetation during the two events of 2015-2016 and 2018-2019 also in wet seasons. In this case, the evaluation of

the most recent drought event is relevant as the observed long-term impact on vegetation suggests further transitioning in the type of drought. As the drought evolves to hydrological drought, impacts are more severe and albeit ecosystems are also strongly affected, due to vegetation conditions the crops are less keen to show resilience in this type of conditions unless irrigation is available. Low NDVI values are observed in the central part of the region.

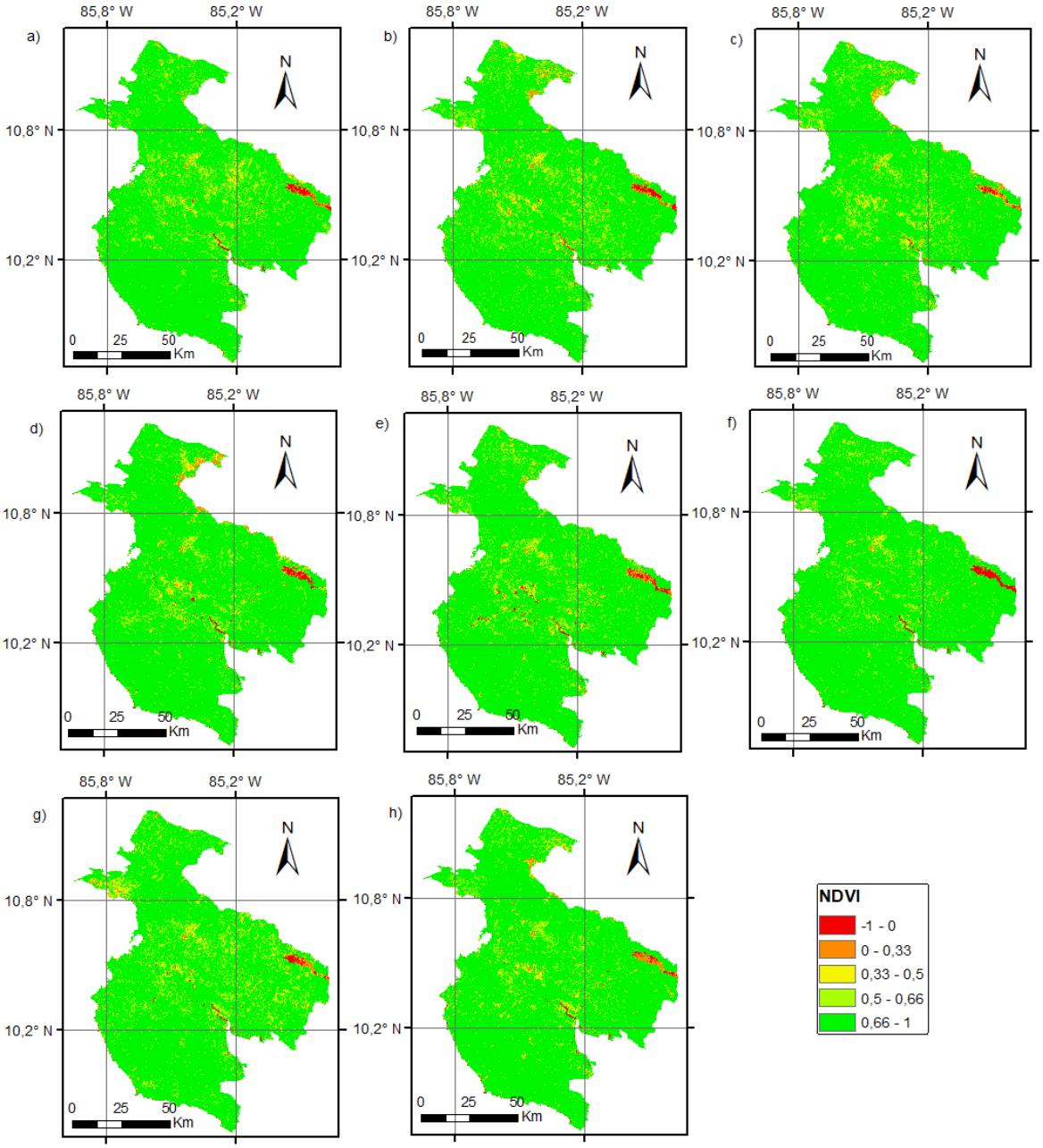

Figure 3.9. Landsat 8 mean NDVI maps from 2014 to 2021

3.2.3. Annual NDVI

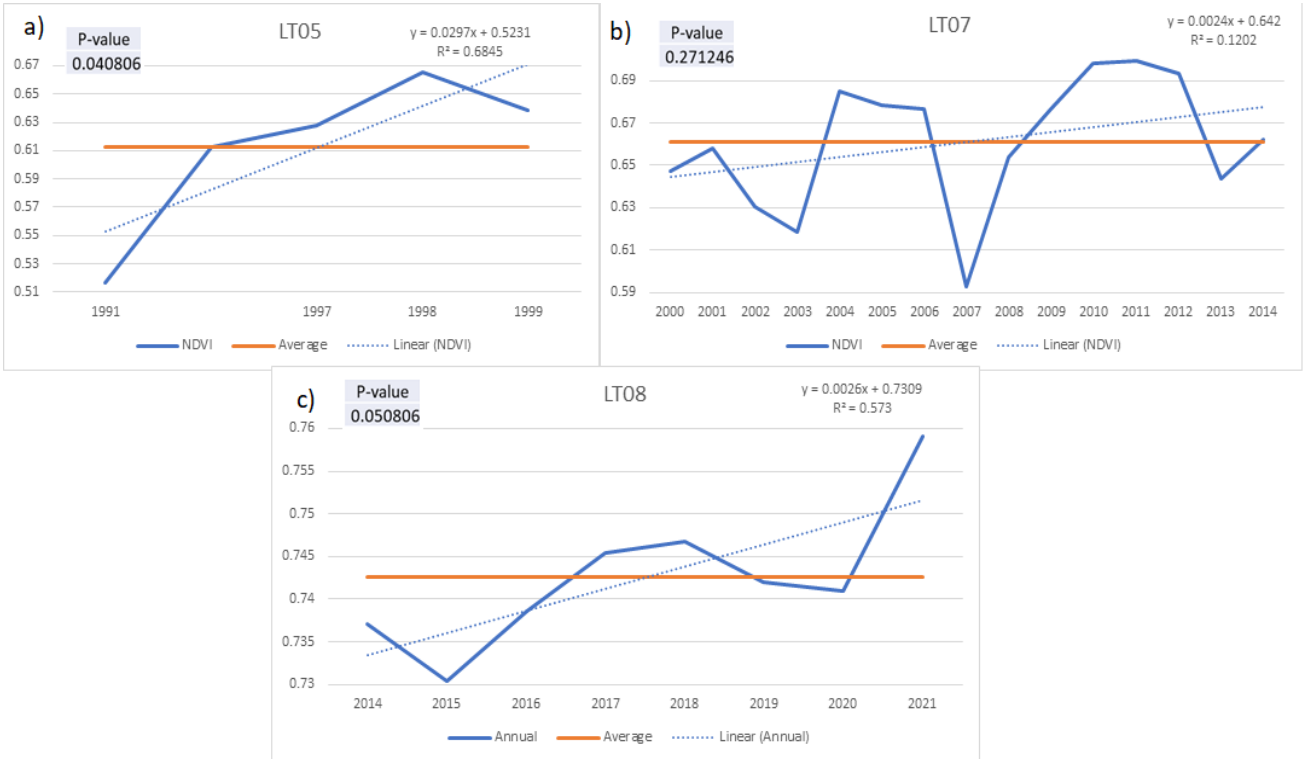

Figure 3.10 Annual mean regional NDVI. a) Landsat 5, 1991-1999; b) Landsat 7, 2000-2014; c) Landsat 8, 2014-2021

The regional annual mean NDVI (Figure 3.10) shows overall an increasing trend over the years, but statistically significant only in the case of Landsat 5. Hence, no significant trends can be defined, and long-term trends impact of drought on NDVI cannot be attributed to observed climate change. In this regard, impact of drought on NDVI are dominated by interannual variability associated to ENSO, climate change impacts on vegetation cannot be discarded as more information is needed. In the case of Landsat 5 imagery (Figure 3.11), information for 1990 was eliminated for the annual analysis because no data were available for the wet season and only the dry season was not sufficient to have an annual overview. The 1991 data were consistent only for the wet season and still mean NDVI remains very low (Figure 3.11a), likely due to the El Niño of 1991-1992. For 1992,1993, 1994, and 1995 were collected only 4 images in December and March of 1992, February 1993 1 image, and 1996 had data available only for the wet season. Therefore, 1992 to 1996 data were hided for the mean annual NDVI calculations. More complete data were available from 1997 to 1999. Overall, there was an increasing trend but not significant. The year 1997 showed low values because of El Niño. Low NDVI values are observed in the central part of the region for 1997,1998 and 1999. 1991 imagery shows high vegetation stress which covers all the region.

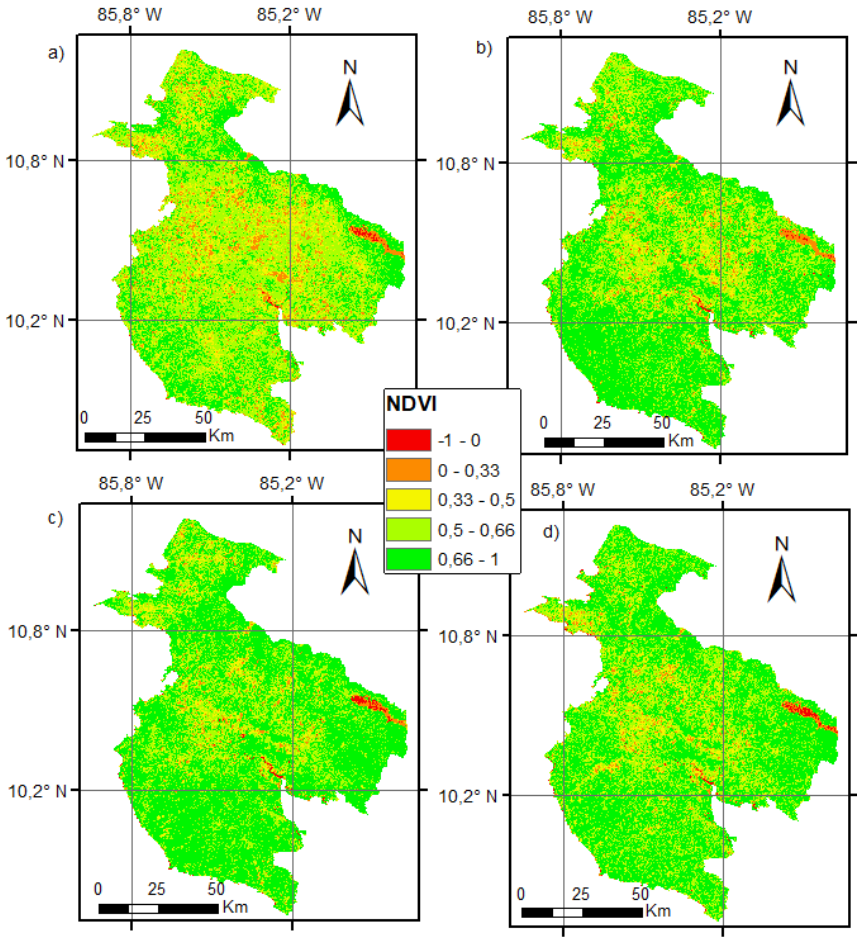

Figure 3.11. Landsat 5 annual mean NDVI. a) 1991; b) 1997; c) 1998; d) 1999

Landsat 7 had a more complete dataset (Figure 3.12), with gaps in the dry seasons of 2000 (only 4 images in January and April), 2002 (7 images in December 2001, March, and April) and 2007 (8 images in February, March and April). Drops in NDVI values can be attributed to El Niño of 2002-2003 and La Niña of 2007-2008. Trend is increasing but in a non-significant way. Low NDVI values are observed in the central part of the region for all the years.

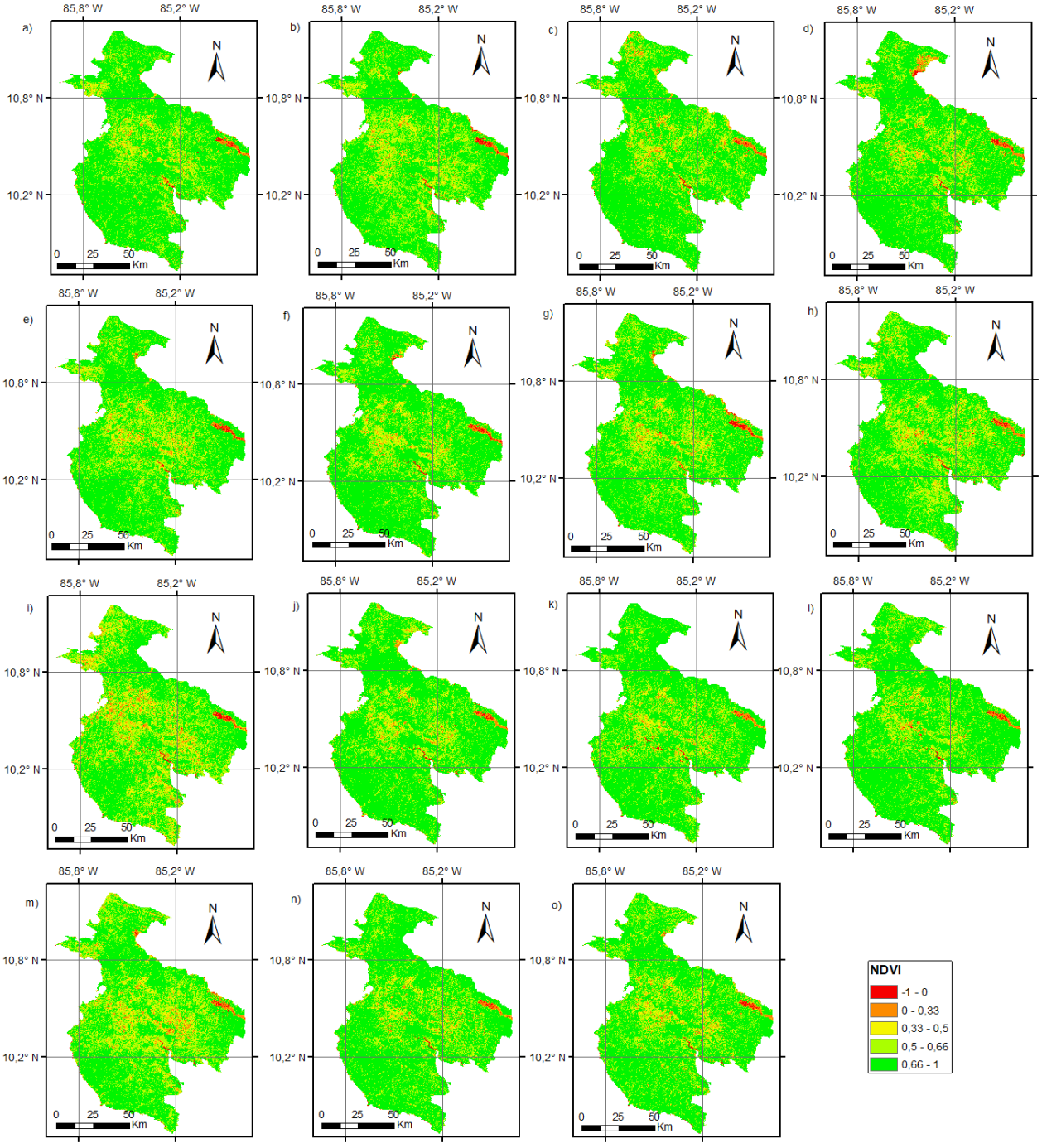

Figure 3.12. Annual mean NDVI maps from Landsat 7. a) 2000; b) 2001; c)2002; d) 2003; e) 2004; f) 2005; g) 2006; h) 2007; i) 2008; j) 2009; k) 2010; l) 2011; m) 2012; n) 2013; o) 2014.

Landsat 8 have the more complete dataset from 2014 to 2021 (Figure 3.13), values below average clearly indicates El Niño occurrence of 2015-2016. Trend is increasing over the years and in a non-significant way. Low NDVI values are observed in the central part of the region for all the years.

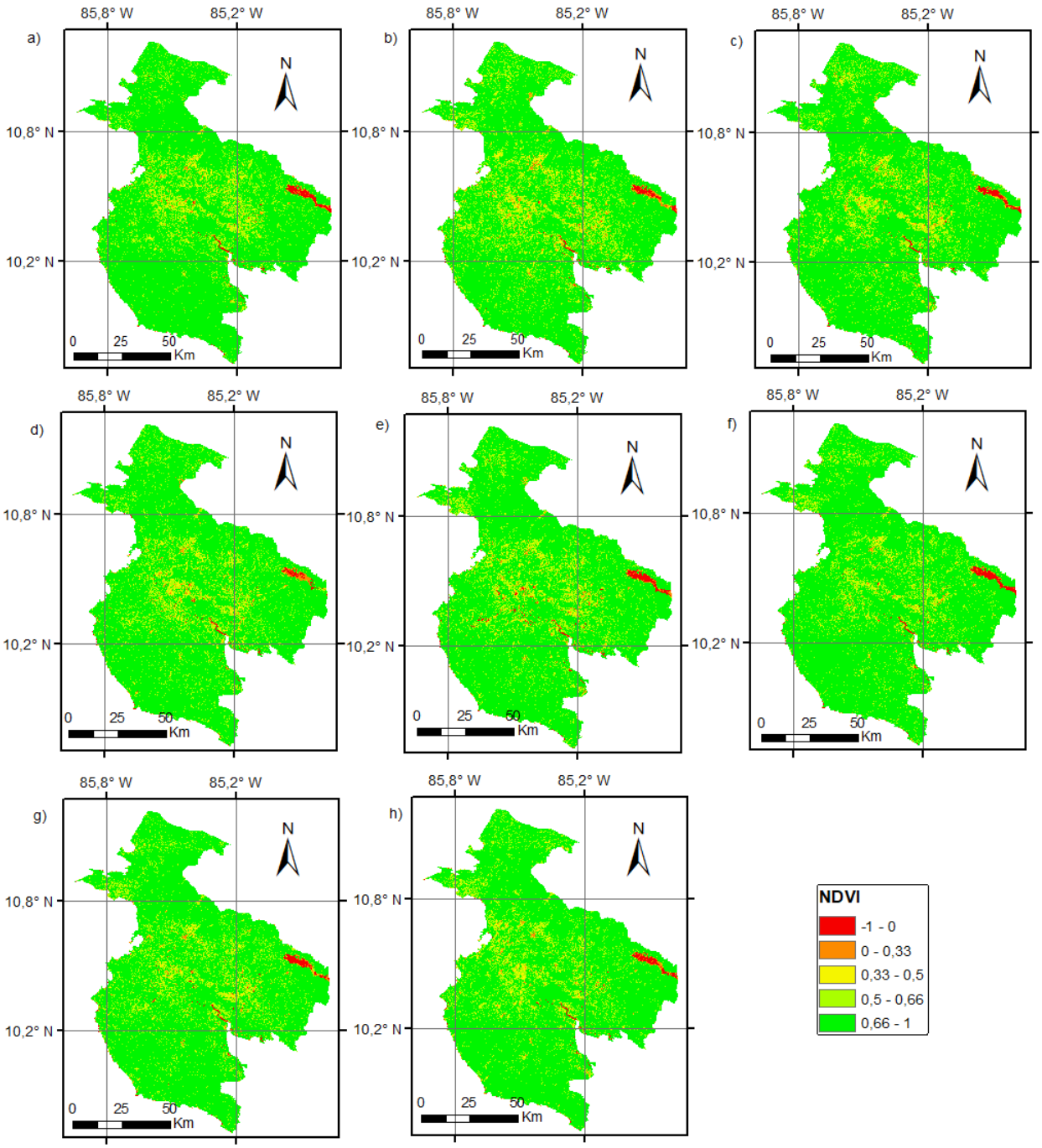

Figure 3.13. Landsat 8 annual mean NDVI maps. a) 2014; b) 2015; c) 2016; d) 2017; e) 2018; f) 2019; g) 2020; h) 2021

3.3. NDVI change

3.3.1. El Niño 1997-1998

During the El Niño event of 1997-1998, NDVI in the cropland area decreased significantly during the dry season (Figure 3.14a and Figure 3.15a) but not during the wet season (Figure 3.14b and Figure 3.15b) where overall, NDVI value increased. During dry season, irrigated crops such as sugar cane melon, and rice are grown, they will

be highly compromised by severe drought conditions induced by El Niño because concessions for water for irrigation are the first to be cut when water availability problems arise. During wet season rainfed crops such as rice and sugar cane are grown and even if there is a big reduction in precipitation, they are still abundant and they are generally enough to support production for almost all crops. Problems will arise again in the following dry season which will experience even more water deficit problem because of the lack of the normal groundwater recharge and limited flows which will inevitably reduce also eventual water storage systems to face the typical periodic dry seasons.

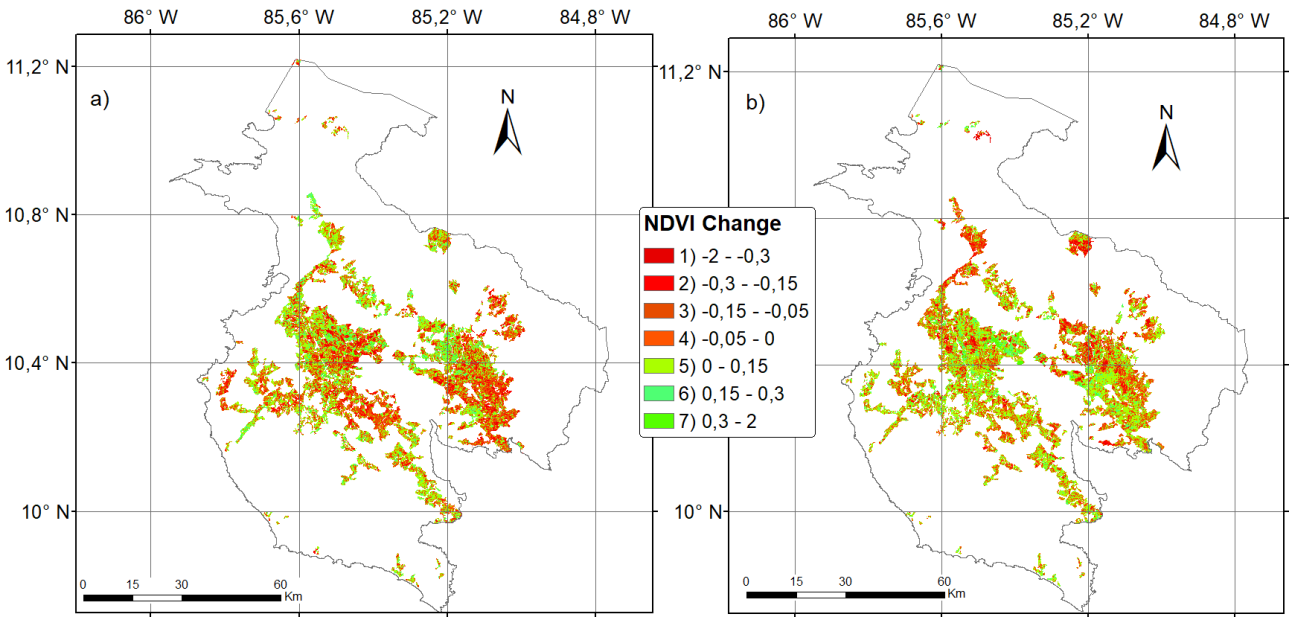

Figure 3.14. NDVI change during a) dry season of El Niño 1997-98 and b) wet season of El Niño 1997-98

Figure 3.15 shows the pixel count for every range of change of NDVI between 1997 dry and wet seasons (inside El Niño) and 1999 dry and wet seasons (outside El Niño). The dry season exhibits a larger decrease compared to the wet season, which means that irrigated crops suffered more than rainfed crops. The average NDVI change during the dry season of 1997 compared to the dry season of 1999 was of -0,008, the average NDVI change during the wet season of 1997 compared to the wet season of 1999 was of 0,034.

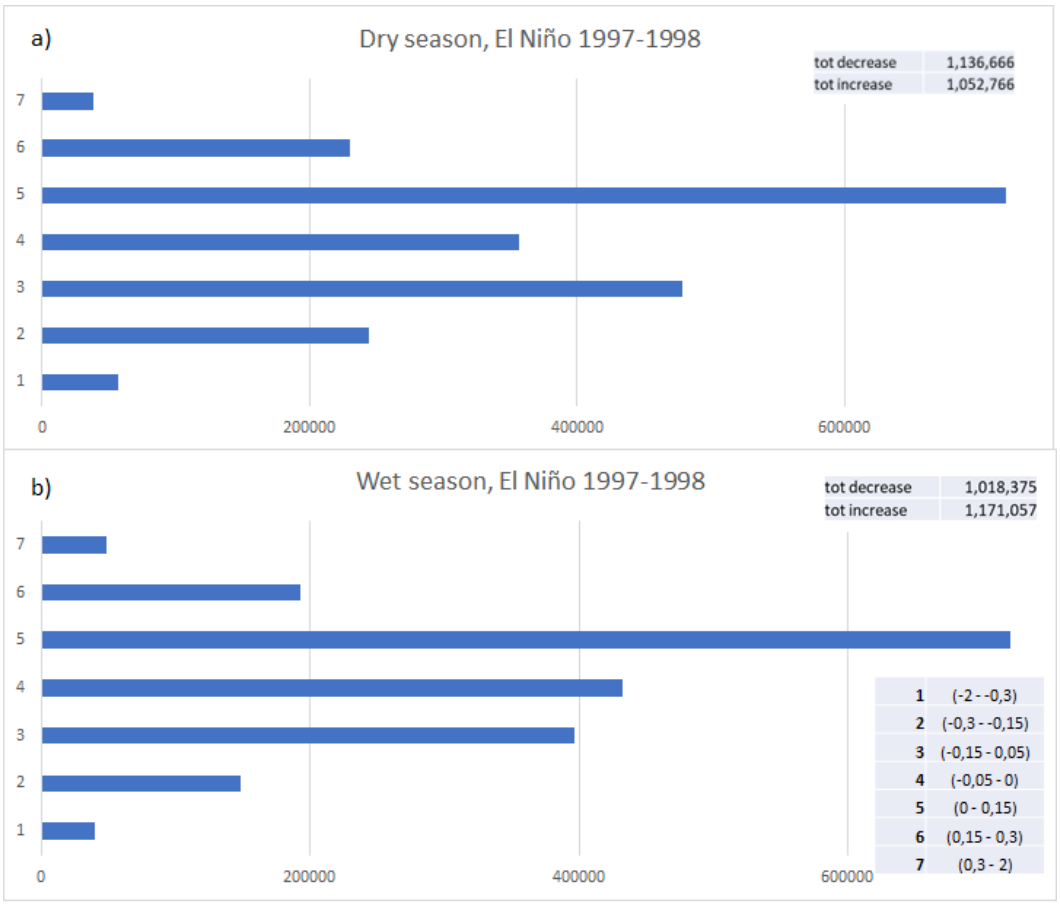

Figure 3.15. Pixel count of the NDVI change for El Niño 1997-1998 a) dry season and b) wet season

3.3.2. El Niño 2015-2016

El Niño of 2015-2016 caused a dramatic decrease of NDVI values in cropland area, comparing both dry (Figure 3.16a) and wet (Figure 3.16b) seasons of 2015 with dry and wet seasons of 2017, we observe that negative effects were higher than the previous event studied. Here, wet season of 2015 showed an even higher vegetation stress compared with 2017 than the dry season, this is due to the early beginning of this phenomenon in the middle of the wet season of 2014. The average NDVI change during the dry season of 2015 compared to the dry season of 2017 was of -0,011. The average NDVI change during the wet season of 2015 compared to the wet season of 2017 was of -0,020.

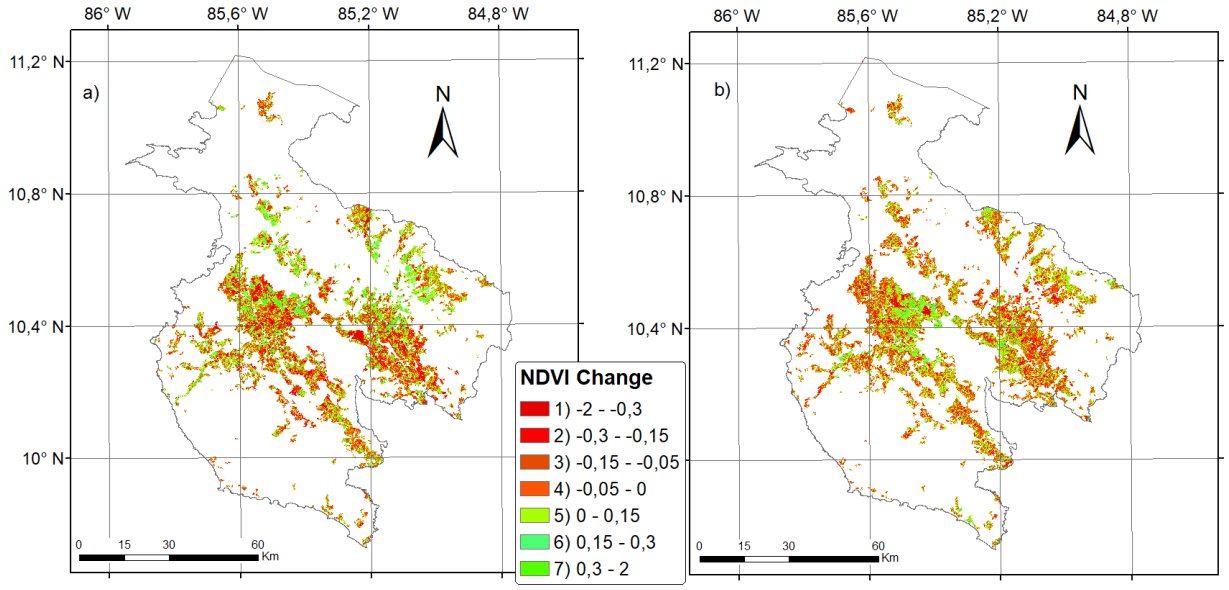

Figure 3.16. NDVI change during a) dry season of El Niño 2015-16 and b) wet season of El Niño 2015-16

Figure 3.17 shows the pixel count of each range of NDVI values change represented in Figure 3.16 and the total increase and decrease of NDVI values. Wet season for this event showed higher decrease of NDVI than dry season. The 2015-2016 event was favoured by conditions that lasted until 2019, worsening the conditions of drought and further impacts on the vegetation.

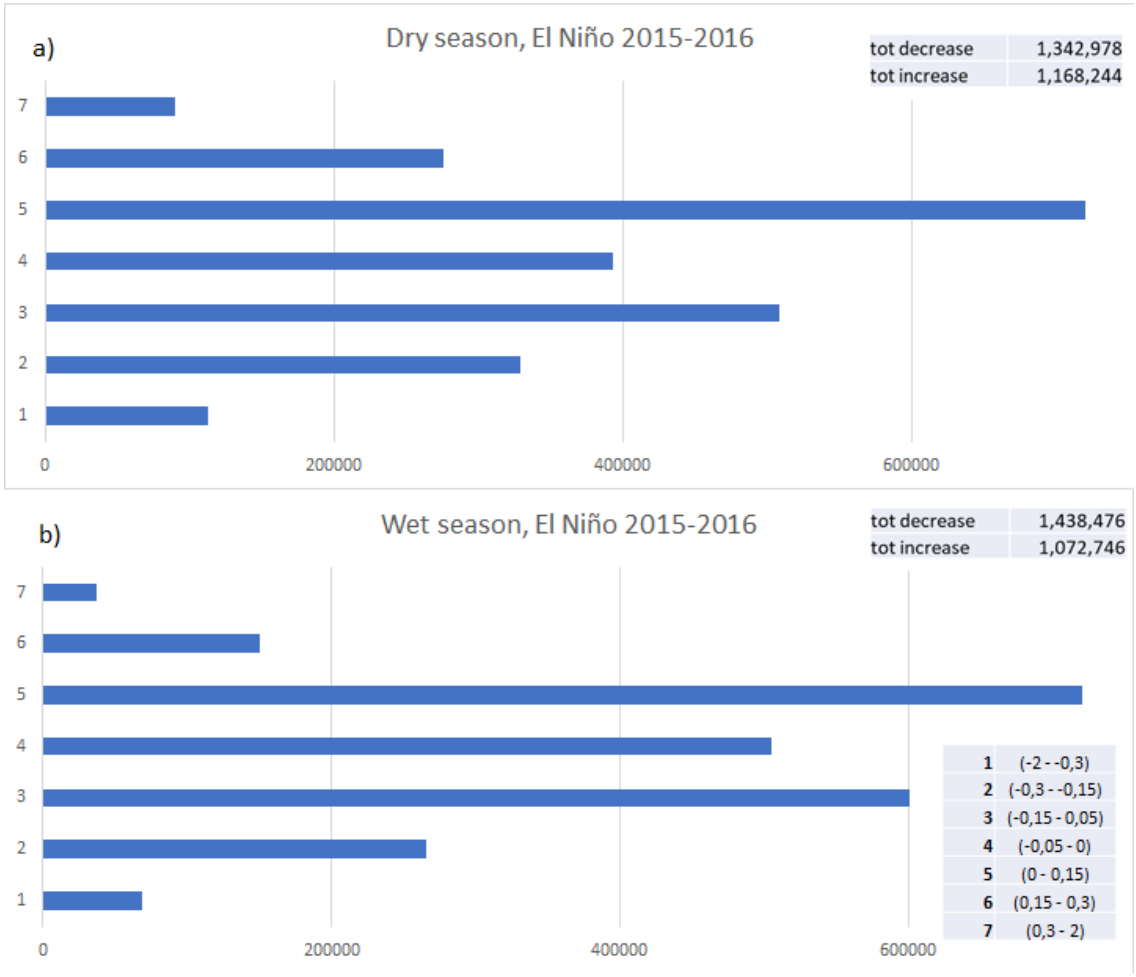

Figure 3.17. Pixel count of the NDVI change for El Niño 2015-2016 a) dry season and b) wet season

4. Discussion

4.1. Uncertainties in the analysis

Even if it has optimal spatial resolution to monitor NDVI in the Chorotega region, and the optimal temporal resolution, different issues were identified for the use of Landsat imagery. Landsat 5 has many missing years or months and for many periods analysed had very few images which do not permit the correct masking of clouds, altering inevitably the final pixel value. The missing data of Landsat 5 did not allow the characterization representation of the strong 1991-1992 event and compromised regression analysis, to create a continuous graph without gaps it was necessary to put the average value in place of missing data. In general, data from Landsat 5 showed overall missing and damaged images which inevitably compromised results and created uncertainties in the analysis.

The damaged in the images of Landsat 7 dataset after the Scan Line Corrector + failure, had the effect of lowering mean NDVI values, altering real values. Landsat 8 was the only collection providing a complete and

exhaustive dataset, but this time the problem was that it is too recent, in fact it starts in 2014, therefore covering only a short part of the analysed timeline. For the reasons explained above, it wasn't possible to a continuous timeline, values were from one satellite to the other. For example, annual mean NDVI value for Landsat 7 in 2014 is 0,661 while for Landsat 8 is 0,736.

4.2. Precipitation charts

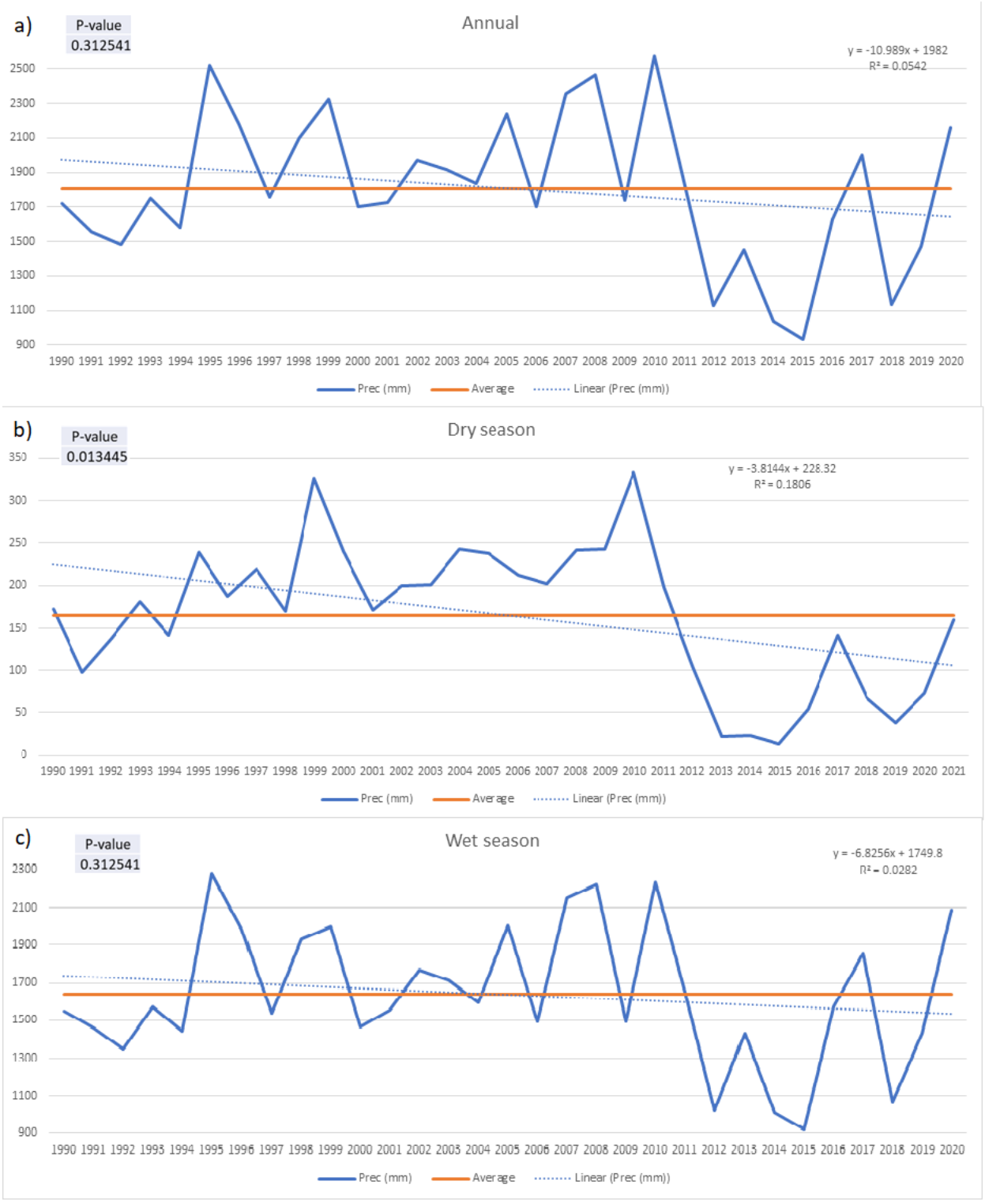

Figure 4.1. Mean regional precipitation. a) Annual mean precipitation from 1990 to 2021; b) Dry season mean precipitation from 1990 to 2021; c) Wet season mean precipitation from 1990 to 2020.

Precipitation trends from 1990 to 2021, for annual, dry and wet seasons are plotted in Figure 4.1, based on the observations anomalous decrease in precipitation was related to El Niño event.

- The annual chart (Figure 4.1a) shows a drop of precipitation under the average from 1990 to 1994, which could be associated with El Niño of 1991-1992 and a weaker event in 1993. The low peak of 1997 is due to El Niño of 1997-1998, a drop in precipitation in 2000-2001 which could represent the early beginning of the 2002-2003 event. The impact of the 2006-2007 event is reflected in precipitation drop during 2006 and the 2009-2010 event is also consistent with the observed rainfall decrease during 2009. From the end of 2011 and from 2012 until 2016 the precipitation remains dramatically below average, due to a succession of close events which have negatively affected normal annual precipitation patterns for more than 4 years. Finally, during the 2018-2019 event precipitation deficit was a characteristic of the drought conditions still present.
- The dry season precipitation chart (Figure 4.1b) starts with two low peaks in 1991 and 1995, and a slight increase above the average in 1993 that not so obvious in the annual chart. For the other events until 2012 precipitation remained above the average line although during the above-mentioned events (1997-1998, 2002-2003, 2006-2007) precipitation reduction is still clear. No significant reduction in precipitation for the dry season of 2009 during the 2009-2010 event was identified. From 2012 to 2020 precipitation remain below the seasonal average values even during years in which El Niño conditions were not present.
- Looking at the wet season precipitation chart (Figure 4.1c), first thing to notice is that every year, more than 80% of total rainfall is concentrated in this season. From 1990 to 1994 rainfall amount stays below the average, 1997-1998, 2006-2007, 2009-2010, 2012, 2015-2016 and 2018-2019 event are clearly recognizable by the peaks below the average line. Anomalous low values are present in 2000-2001, maybe due to an early lowering of precipitation before 2002-2003 event.

Anomalous reduction of rainfall below historical average during El Niño events in more marked during wet seasons than during dry seasons from 1990 to 2011-2012. After 2012, the clustering of dry years made precipitation fall under historical average also during the dry season.

The unstable behaviour of weather systems leads to uncertainty in forecasts and management decisions, under ENSO events the forecast at the seasonal scale is fundamental, mainly because the region is highly dependent on natural resources.

The significant decreasing trend in precipitation results from the concentration of dry years and El Niño events in the analysis period, this trend is not significant for annual and wet season but still is decreasing because

of the same reason. The 30-years' time series analysed in this study is not enough to describe the effects of climate change given the bias to El Niño conditions.

4.3. Land cover change

The number of pixels belonging to cropland area, forest, shrubland and grassland (which in our region mostly corresponds to pastures) were counted to observe two-decade changes and land cover dynamics (Figure 4.2.).

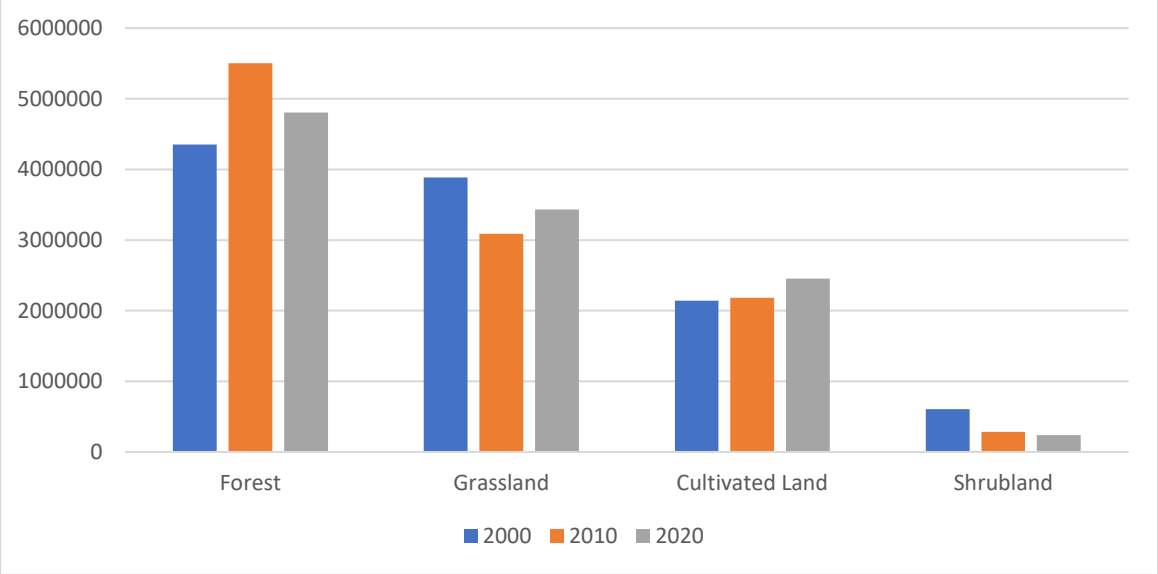

Figure 4.2. Pixel count for selected land cover classes

Land cover change maps showed a net increase of forest over the years from 2000, consistent with the efforts for forest restoration that has a longer history back to 1980. In this study, analysing regional NDVI trends, for the three satellited we have observed always an increasing trend, which seems to be strange because overall temperature are increasing and most of all precipitation is lowering. This should have a negative effect of environment and vegetation, but apparently in this region human impact had a positive effect regarding reforestation. The effort of the country in reforestation over the years have resulted in an increased resilience of the whole territory and an increased environmental health and better vegetation status.

To have a better understanding of the reasons of NDVI trends and quantify even more in detail the impact on agriculture, more detailed agricultural data such as precise land cover maps indicating the type of crops grown in each area and historical yields records would have been very helpful to develop this research. However systematic datasets for the whole are not available, similar to the case of information on irrigation in the region. Furthermore, the fragmented agricultural landscape and the scale of the farms represents a difficulty even at the resolution for which Landsat is available. However, consistent results relate a visible impact of ENSO

events on vegetation by means of the NDVI, suggesting that in the long run, satellite imagery is a useful tool to assess impacts of ENSO related precipitation anomalies on agriculture in the southernmost part of the CADC.

5. Conclusions

This study used images of Landsat 5, Landsat 7 and Landsat 8 to calculate mean regional NDVI and NDVI change during the strongest El Niño events of the last 30 years, the 1997-1998 event and the 2015-2016 event. By looking at NDVI change during strongest events it was possible to demonstrate that El Niño have a negative impact on agriculture, caused by the influence of drought in the area. The El Niño impact on reduction of vegetation health was also identified for less intense El Niño event, showing that the impact is not restricted to the intense El Niño events. To better identify impacts on specific crops, more detailed information about type of crops cultivated in the region and their exact locations would have been useful for further considerations and more detailed analysis and would allow more specific results. Albeit El Niño causes drought conditions, the development of tropical cyclones in the eastern tropical Pacific is also enhanced which contributes to heavy rainfall over that area. Hence, the vegetation response to drought in time is often hindered by this type of heavy rainfall events. This is one of the reasons why attempts like this to identify drought and NDVI links often fail.

The 30-years trend of precipitation is consistent with seasonal and interannual variability caused by the ENSO event. However, the long meteorological drought that started between 2011-2012 and lasted until 2019, highlights an increase in the frequency of Nino occurrence and the severity of dry seasons in recent years. This inevitably led to an increase in vegetation stress, which was confirmed by the negative values in the NDVI trend between 2013 and 2019 especially during the dry seasons. If this trend continues in the coming years combined with the typical effects of climate change such as increasing temperatures and frequency of extreme events, water resource management will become increasingly complicated and challenging.

Negative effects of El Niño events could be mitigated by better environmental policies focused on improve the resilience of agricultural areas to climate variability and extreme events. Water resources management must be improved by promoting hydrometeorological monitoring and sustainable agricultural practices oriented to optimize water use efficiency, avoiding wastes and improve water storage during wet periods to ensure sustainable irrigation is available for the most critic crops.

This study gives a continuous vision in time and space of the impact of this phenomenon in the Chorotega region by analysing NDVI dynamics, it is a valid tool and aid for agricultural drought management at regional scale. However, more detailed studies which could fill the gaps in the information encountered would help to complete the research and have a better understanding of the impact of the phenomenon on agriculture.

Cloudiness remains the main issue in the use of satellite imagery to identify vegetation changes during the wet season. Further analysis should include soil moisture information to better follow the propagation of the meteorological drought to hydrological drought and better understand how the intensity of ENSO may drive more prolonged droughts that limit the recovery of the soil moisture and thus strongly affect agriculture and ecosystems.

6. Annex

Annex A

Google Earth Engine complete Data Catalogue

Group	Field of application/Program	Datasets
Climate and Weather	Surface Temperature, Climate, Atmospheric, Weather	ERA 5
		GRIDMET
		TerraClimate
		MOD08_M3.061 Terra Atmosphere
		MYD08_M3.061 Aqua Atmosphere
		AG100: ASTER Global Emissivity Dataset
		FLDAS
		GLDAS
		NEX-DCP30
		NEX-GDDP
		Ocean Color SMI
		Daymet V4
		NCEP/NCAR
		NOAA CDS OISST v02r01
		NOAA CDR PATMOSX
		NOAA AVHRR
		CFSR
		RTMA
		PRISM
		WorldClim
		Sentinel-5P
		Copernicus Atmosphere Monitoring Service (CAMS)
		MACAv2-METDATA
		GCOM-C/SGLI
		GSMaP
		GPM
		NDAS-2
		GOES-16
		GOES-17
		NCEP-DOE
		PERSIANN-CDR
		TOMS and OMI
		TRMM
		CHIRPS

		Global Power Plant Database
		YCEO
		CFSV2
		GFS
		NOAA NHC HURDAT2
Imagery	Landsat	Landsat 1-5MSS
		Landsat 4 TM
		Landsat 5 TM
		Landsat 7 ETM+
		Landsat 8 OLI/TIRS
		Landsat 9 OLI-2/TIRS-2
	MODIS	MCD43A4.006
		MCD43A3.006
		MCD43A2.006
		MOD09GQ.006
		MOD10A1.006
		MOD11A1.006
		MOD09GA.006
		MODOCGA.006
		MOD14A1.006
		MCD43A1.006
	Sentinel	Sentinel-1 SAR GRD
		Sentinel-2 MSI
		Sentinel-3 OLCI EFR
		Sentinel-5P TROPOMI
	High-Resolution Imagery	Planet SkySat Public Ortho Imagery
		NAIP:National Agriculture Imagery Program
Geophysical	Terrain	AHN Netherlands
		Australian 5m DEM
		DEM-H
		DEM-S
		SRTM Digital Elevation Data
		CryoSat-2 Antarctica
		Global ALOS
		Global SRTM
		US NED
		US Lithology
		US Physiography
		HYCOM
		ALOS DSM
		GEDI L2A

		GEDI L4B
		MERIT
		AG100
		NASADEM
		ETOPO1
		Canadian Digital Elevation Model
		USGS 3DEP
		GMTED2010
		GTOPO30
		NASA SRTM
		WWF HydroSHEDS
	Land Cover	Canada AAFC
		Copernicus CORINE
		Copernicus Global Land Cover Layers
		CSP gHM
		World Settlement Footprint 2015
		FireCCI51
		GlobCover
		ESA WorldCover
		GLIMS
		Dynamic World
		Global PALSAR-2/PALSAR Forest/Non-Forest Map
		LUCAS Harmonized
		Iran Land Cover Map
		MCD12Q1.006
		Oxford MAP
		DESS China Terrace Map
		USDA NASS
		USFS Landscape Change Monitoring System
		USGS GAP
		GFSAD1000
		NLCD 2016
		NLCD 2019
	Cropland	USDA NASS
		GFSAD1000
	Other Geophysical Data	FIRMS
		GRIDMET DROUGHT
		MACAv2-METDATA
		TerraClimate
		JRC
		MCD64A1.006

		MOD44B.006
		MOD44W.006
		MOD44W.005
		Global Forest Canopy Height, 2005
		NLDAS-2
		NASA-USDA Enhanced SMAP
		Hansen Global Forest Change
		ArcticDEM
		REMA
		WHRC

Annex B

Google Earth Engine codes used to download all NDVI maps and values.

Input script with imported data:

```
var imageCollection = ee.ImageCollection("LANDSAT/LT05/C01/T1_SR"),
    geometry = ee.FeatureCollection("users/irenedellolio/Esporta_Output");
```

NDVI map calculations and download codes, in the screenshot below is shown the code to download 1990 dry season mean NDVI map and dataset from Landsat 5.

```
1
2
3   // Get the least cloudy image in 2015.
4   var dataset = ee.ImageCollection("LANDSAT/LT05/C01/T1_SR")
5     .filterBounds(geometry)
6     .filterDate('1989-12-01', '1990-04-30')
7    //   .sort('CLOUD_COVER')
8   var visParams = {
9     bands:['B3','B2','B1'],
10    min:0,
11    max:3000,
12    gamma:1.4,
13  };
14  print(dataset)
15  Map.addLayer(dataset.min(),visParams)
16
17  // Compute the Normalized Difference Vegetation Index (NDVI).
18  var image = dataset.min()
19
20  var nir = image.select('B4');
21  var red = image.select('B3');
22  var ndvi = nir.subtract(red).divide(nir.add(red)).rename('NDVI');
23
24  ndvi = ndvi.clip(geometry)
25
26  var visParams1 = {
27
28    min:-1,
29    max:1,
30     pllette:['blue','white','green'],
31  };
32
33
34  // give a normal value to the extrem value
35  ndvi = ndvi.where(ndvi.lt(-1),-1)
36  ndvi = ndvi.where(ndvi.gt(1),1)
37
38  Map.addLayer(ndvi,visParams1,'ndvi')
39
40  var histogram = ndvi.reduceRegion({
41    reducer: ee.Reducer.histogram(255, 2)
42        .combine('mean', null, true)
43        .combine('variance', null, true),
44  geometry:geometry ,
45    scale: 100,
46    bestEffort: true
47  });
48  // Chart the histogram
49  print(Chart.image.histogram(ndvi, geometry, 100));
50
51  Export.image.toDrive({
52    image:ndvi,
53    region:geometry,
54     scale:30,
55     folder:'ndvi',
56     maxPixels:1e13,
57  });
58
59
60
61
```

Figure B.1. Codes used in GEE platform to compute and download NDVI maps from Landsat imagery

Annex C

Results of the regression analysis carried out in Microsoft Excel for NDVI and precipitation data.

a) SUMMARY OUTPUT

Regression Statistics	
Multiple R	0.501993333
R Square	0.251997306
Adjusted R Sq	0.064996633
Standard Erro	0.120118563
Observations	6

ANOVA

	df	*SS*	*MS*	*F*	*Significance F*
Regression	1	0.019443435	0.019443	1.347574	0.310260484
Residual	4	0.057713877	0.014428		
Total	5	0.077157311			

	Coefficients	*Standard Error*	*t Stat*	*P-value*	*Lower 95%*	*Upper 95%*	*Lower 95.0%*	*Upper 95.0%*
Intercept	-31.06644356	27.21410286	-1.14156	0.317336	-106.624906	44.4920191	-106.62491	44.4920191
X Variable 1	0.015839287	0.013644552	1.160851	0.31026	-0.02204406	0.05372264	-0.0220441	0.053722637

b) SUMMARY OUTPUT

Regression Statistics	
Multiple R	0.3779632
R Square	0.1428562
Adjusted R Squ	0.076922
Standard Error	0.0462362
Observations	15

ANOVA

	df	*SS*	*MS*	*F*	*Significance F*
Regression	1	0.004631833	0.004632	2.166649	0.16482503
Residual	13	0.027791222	0.002138		
Total	14	0.032423055			

	Coefficients	*Standard Error*	*t Stat*	*P-value*	*Lower 95%*	*Upper 95%*	*Lower 95.0%*	*Upper 95.0%*
Intercept	-7.547734	5.545637918	-1.36102	0.196634	-19.5283563	4.4328884	-19.528356	4.43288839
X Variable 1	0.0040672	0.002763142	1.471954	0.164825	-0.00190219	0.0100366	-0.0019022	0.01003662

c) SUMMARY OUTPUT

Regression Statistics	
Multiple R	0.69224159
R Square	0.47919842
Adjusted R	0.39239816
Standard E	0.00848943
Observatic	8

ANOVA

	df	*SS*	*MS*	*F*	*Significance F*
Regressior	1	0.000397879	0.000398	5.520702	0.05708828
Residual	6	0.000432422	7.21E-05		
Total	7	0.000830301			

	Coefficients	*Standard Error*	*t Stat*	*P-value*	*Lower 95%*	*Upper 95%*	*Lower 95.0%*	*Upper 95.0%*
Intercept	-5.50224807	2.642819994	-2.08196	0.082511	-11.968996	0.9644995	-11.968996	0.96449949
X Variable	0.00307787	0.001309947	2.349618	0.057088	-0.0001275	0.0062832	-0.0001275	0.0062832

Figure C.1. Regression analysis results of dry season regional mean NDVI. a) Landsat 5; b) Landsat 7; c) Landsat 8

a) SUMMARY OUTPUT

Regression Statistics	
Multiple R	0.9419664
R Square	0.8873006
Adjusted R Square	0.8497342
Standard Error	0.0167559
Observations	5

ANOVA

	df	*SS*	*MS*	*F*	*Significance F*
Regression	1	0.00663144	0.006631	23.61949	0.01663552
Residual	3	0.000842284	0.000281		
Total	4	0.007473724			

	Coefficients	*Standard Error*	*t Stat*	*P-value*	*Lower 95%*	*Upper 95%*	*Lower 95.0%*	*Upper 95.0%*
Intercept	-25.42624	5.369789799	-4.73505	0.017857	-42.515308	-8.33717	-42.5153076	-8.3371722
X Variable 1	0.0130734	0.002690003	4.859989	0.016636	0.00451259	0.021634	0.004512594	0.02163418

b) SUMMARY OUTPUT

Regression Statistics	
Multiple R	0.3380971
R Square	0.1143096
Adjusted R	0.051046
Standard E	0.0406294
Observatic	16

ANOVA

	df	*SS*	*MS*	*F*	*Significance F*
Regressior	1	0.002982702	0.002983	1.806878	0.200261198
Residual	14	0.023110482	0.001651		
Total	15	0.026093184			

	Coefficients	*Standard Error*	*t Stat*	*P-value*	*Lower 95%*	*Upper 95%*	*Lower 95.0%*	*Upper 95.0%*
Intercept	-5.242794	4.421211972	-1.18583	0.255427	-14.72535041	4.239763	-14.72535	4.239762752
X Variable	0.0029619	0.002203439	1.344202	0.200261	-0.00176404	0.007688	-0.001764	0.007687773

c) SUMMARY OUTPUT

Regression Statistics	
Multiple R	0.47486439
R Square	0.22549619
Adjusted R Square	0.09641222
Standard Error	0.01035564
Observations	8

ANOVA

	df	*SS*	*MS*	*F*	*Significance F*
Regression	1	0.000187336	0.000187	1.746895	0.234424597
Residual	6	0.000643435	0.000107		
Total	7	0.000830771			

	Coefficients	*Standard Error*	*t Stat*	*P-value*	*Lower 95%*	*Upper 95%*	*Lower 95.0%*	*Upper 95.0%*
Intercept	-3.4831732	3.223783999	-1.08046	0.321441	-11.3714885	4.405142	-11.371489	4.40514203
X Variable 1	0.00211196	0.001597909	1.321702	0.234425	-0.00179798	0.0060219	-0.001798	0.0060219

Figure C.2. Regression analysis results of regional wet season mean NDVI trend. a) Landsat 5; b) Landsat 7; c) Landsat 8

a)

SUMMARY OUTPUT

Regression Statistics	
Multiple R	0.9605273
R Square	0.9226127
Adjusted R Square	0.8839191
Standard Error	0.022338
Observations	4

ANOVA

	df	*SS*	*MS*	*F*	*Significance F*
Regression	1	0.011897819	0.011898	23.84405	0.03947267
Residual	2	0.00099797	0.000499		
Total	3	0.012895789			

	Coefficients	*Standard Error*	*t Stat*	*P-value*	*Lower 95%*	*Upper 95%*	*Lower 95.0%*	*Upper 95.0%*
Intercept	-34.36724	7.163467376	-4.79757	0.040806	-65.189155	-3.54533	-65.189155	-3.5453297
X Variable 1	0.0175226	0.003588458	4.883037	0.039473	0.00208268	0.032962	0.00208268	0.03296246

b)

SUMMARY OUTPUT

Regression Statistics	
Multiple R	0.346748
R Square	0.120234
Adjusted R Square	0.05256
Standard Error	0.029973
Observations	15

ANOVA

	df	*SS*	*MS*	*F*	*Significance F*
Regression	1	0.001596115	0.001596	1.776655	0.20545054
Residual	13	0.011678967	0.000898		
Total	14	0.013275083			

	Coefficients	*Standard Error*	*t Stat*	*P-value*	*Lower 95%*	*Upper 95%*	*Lower 95.0%*	*Upper 95.0%*
Intercept	-4.13077	3.595008358	-1.14903	0.271246	-11.8973119	3.6357749	-11.897312	3.6357749
X Variable 1	0.002388	0.001791231	1.332912	0.205451	-0.00148217	0.0062573	-0.0014822	0.00625727

c)

SUMMARY OUTPUT

Regression Statistics	
Multiple R	0.7569782
R Square	0.573016
Adjusted R Square	0.5018519
Standard Error	0.0059265
Observations	8

ANOVA

	df	*SS*	*MS*	*F*	*Significance F*
Regression	1	0.000282811	0.000283	8.052047	0.02965974
Residual	6	0.000210737	3.51E-05		
Total	7	0.000493548			

	Coefficients	*Standard Error*	*t Stat*	*P-value*	*Lower 95%*	*Upper 95%*	*Lower 95.0%*	*Upper 95.0%*
Intercept	-4.4927107	1.844948048	-2.43514	0.050806	-9.0071359	0.021715	-9.0071359	0.02171459
X Variable 1	0.0025949	0.000914472	2.837613	0.02966	0.00035729	0.004833	0.00035729	0.00483255

Figure C.3. Results of the regression analysis of mean annual regional NDVI. a) Landsat 5; b) Landsat 7; c) Landsat 8

a)

SUMMARY OUTPUT

Regression Statistics	
Multiple R	0.2328626
R Square	0.054225
Adjusted R Square	0.021612
Standard Error	424.39659
Observations	31

ANOVA

	df	*SS*	*MS*	*F*	*Significance F*
Regression	1	299469.9888	299470	1.662683	0.20743122
Residual	29	5223261.387	180112.5		
Total	30	5522731.375			

	Coefficients	*Standard Error*	*t Stat*	*P-value*	*Lower 95%*	*Upper 95%*	*Lower 95.0%*	*Upper 95.0%*
Intercept	23838.706	17086.95748	1.39514	0.173567	-11108.046	58785.458	-11108.046	58785.4578
X Variable 1	-10.98881	8.522088511	-1.28945	0.207431	-28.4184418	6.4408143	-28.4184418	6.44081428

b)

SUMMARY OUTPUT

Regression Statistics	
Multiple R	0.4249451
R Square	0.1805784
Adjusted R Square	0.1532643
Standard Error	77.483111
Observations	32

ANOVA

	df	*SS*	*MS*	*F*	*ignificance F*
Regression	1	39691.14837	39691.15	6.611189	0.0153346
Residual	30	180108.976	6003.633		
Total	31	219800.1243			

	Coefficients	*Standard Error*	*t Stat*	*P-value*	*Lower 95%*	*Upper 95%*	*Lower 95.0%*	*Upper 95.0%*
Intercept	7815.1323	2975.172403	2.626783	0.013445	1739.0197	13891.245	1739.01969	13891.245
X Variable 1	-3.8143861	1.483490837	-2.57122	0.015335	-6.844079	-0.7846936	-6.8440786	-0.7846936

c)

SUMMARY OUTPUT

Regression Statistics	
Multiple R	0.1680062
R Square	0.0282261
Adjusted R Square	-0.005283
Standard Error	370.35845
Observations	31

ANOVA

	df	*SS*	*MS*	*F*	*Significance F*
Regression	1	115538.7388	115538.7	0.842332	0.3663012
Residual	29	3977795.96	137165.4		
Total	30	4093334.699			

	Coefficients	*Standard Error*	*t Stat*	*P-value*	*Lower 95%*	*Upper 95%*	*Lower 95.0%*	*Upper 95.0%*
Intercept	15325.828	14911.28634	1.027801	0.312541	-15171.177	45822.833	-15171.1766	45822.8331
X Variable 1	-6.825555	7.436976546	-0.91779	0.366301	-22.03588	8.3847699	-22.0358799	8.38476987

Figure C.4. Regression analysis results for precipitation trend. a) Annual; b) Dry season; c) Wet season.

7. References

Adams, R. M., Chen, C. C., McCarl, B. A., & Weiher, R. F. (1999). The economic consequences of ENSO events for agriculture. *Climate Research*, *13*(3), 165–172. https://doi.org/10.3354/CR013165

Amani, M., Ghorbanian, A., Ahmadi, S. A., Kakooei, M., Moghimi, A., Mirmazloumi, S. M., Moghaddam, S. H. A., Mahdavi, S., Ghahremanloo, M., Parsian, S., Wu, Q., & Brisco, B. (2020). Google Earth Engine Cloud Computing Platform for Remote Sensing Big Data Applications: A Comprehensive Review. *IEEE Journal of Selected Topics in Applied Earth Observations and Remote Sensing*, *13*, 5326–5350. https://doi.org/10.1109/JSTARS.2020.3021052

Anyamba, A., Chretien, J.-P., Britch, S. C., soebiyanto, R. P., small, J. L., Jepsen, R., Forshey, B. M., sanchez, J. L., smith, R. D., Harris, R., tucker, C. J., Karesh, W. B., & Linthicum, K. J. (2019). Global Disease outbreaks Associated with the 2015–2016 El Niño event. *Scientific Reports*. https://doi.org/10.1038/s41598-018-38034-z

Benavides, J., Mateos, L., García-Vila, M., & Fereres, E. (2021). Evaluating irrigation scheme performance in a tropical environment: The Guanacaste scheme, Costa Rica*. *Irrigation and Drainage*, *70*(5), 1331–1346. https://doi.org/10.1002/ird.2621

Birkel, C. (2005). *Temporal and Spatial Variability of Drought Indices in Costa Rica*. Albert-Ludwigs-Universität Freiburg i. Br.

Birkel, C., Brenes, A., & Sánchez-Murillo, R. (2017). The Tempisque-Bebedero catchment system: energy-water-food consensus in the seasonally dry tropics of northwestern Costa Rica. *Technology Arts Sciences*, 72–76. www.water-energy-food-nexus.info

Brönnimann, S. (2007). Impact of El Niño-Southern Oscillation on European climate. *Reviews of Geophysics*, *45*(3). https://doi.org/10.1029/2006RG000199

Bulgin, C. E., Merchant, C. J., & Ferreira, D. (2020). Tendencies, variability and persistence of sea surface temperature anomalies. *Scientific Reports*, *10*(1), 7986. https://doi.org/10.1038/S41598-020-64785-9

Cai, W., Wang, G., Dewitte, B., Wu, L., Santoso, A., Takahashi, K., Yang, Y., Carréric, A., & McPhaden, M. J. (2018). Increased variability of eastern Pacific El Niño under greenhouse warming. *Nature 2018 564:7735*, *564*(7735), 201–206. https://doi.org/10.1038/s41586-018-0776-9

Calvo-Alvarado, J., McLennan, B., Sánchez-Azofeifa, A., & Garvin, T. (2009). Deforestation and forest restoration in Guanacaste, Costa Rica: Putting conservation policies in context. *Forest Ecology and Management*, *258*(6), 931–940. https://doi.org/10.1016/J.FORECO.2008.10.035

Cao, R., Feng, Y., Chen, J., & Zhou, J. (2021). A Supplementary Module to Improve Accuracy of the Quality Assessment Band in Landsat Cloud Images. *Remote Sensing 2021, Vol. 13, Page 4947*, *13*(23), 4947. https://doi.org/10.3390/RS13234947

Chen, J., & Chen, J. (2018). GlobeLand30: Operational global land cover mapping and big-data analysis. *Science China Earth Sciences*, *61*, 1533–1534. https://doi.org/10.1007/s11430-018-9255-3

Durán-Quesada, A. M., Gimeno, L., & Amador, J. (2017). Role of moisture transport for Central American precipitation. *Earth System Dynamics*, *8*(1), 147–161. https://doi.org/10.5194/esd-8-147-2017

Durán-Quesada, A. M., Sorí, R., Ordoñez, P., & Gimeno, L. (2020). Climate Perspectives in the Intra–Americas Seas. *Atmosphere 2020, Vol. 11, Page 959*, *11*(9), 959. https://doi.org/10.3390/ATMOS11090959

Eduardo Quesada-Hernández, L., David Calvo-Solano, O., Hidalgo, H. G., Pé rez-Briceñ, P. M., & Alfaro, E. J. (2019). Dynamical delimitation of the Central American Dry Corridor (CADC) using drought indices and aridity values. *Progress in Physical Geography*, *3*(5), 627–642. https://doi.org/https://doi.org/10.1177/0309133319860224

Emery, W., & Camps, A. (2017). Basic Electromagnetic Concepts and Applications to Optical Sensors. In *Introduction to Satellite Remote Sensing* (pp. 43–83). Elsevier. https://doi.org/10.1016/B978-0-12-809254-5.00002-6

Erasmi, S., Propastin, P., Kappas, M., & Panferov, O. (2009). Spatial Patterns of NDVI Variation over Indonesia and Their Relationship to ENSO Warm Events during the Period 1982–2006. *Journal of Climate*, *22*(24), 6612–6623. https://doi.org/10.1175/2009JCLI2460.1

Flores Q, J. (2007). *Agrocadena de la caña de azucar para la produccion de dulce* .

Gotlieb, Y., Pérez-Briceño, P., Hidalgo, H., & Alfaro, E. (2019). *The Central American Dry Corridor: a consensus statement and its background*.

Harvey, W. J., Petrokofsky, G., Stansell, N., Nogué, S., Petrokofsky, L., Willis, K. J., & Martin, T. A. (2021). *Forests, Water, and Land Use Change across the Central American Isthmus: Mapping the Evidence Base for Terrestrial Holocene Palaeoenvironmental Proxies*. *12*, 1057. https://doi.org/10.3390/f12081057

Hoell, A., & Funk, C. (2013). The ENSO-Related West Pacific Sea Surface Temperature Gradient. *Journal of Climate*, *26*(23), 9545–9562. https://doi.org/10.1175/JCLI-D-12-00344.1

Hoell, A., Hoerling, M., Eischeid, J., Wolter, K., Dole, R., Perlwitz, J., Xu, T., & Cheng, L. (2016). Does El Niño intensity matter for California precipitation? *Geophysical Research Letters*, *43*(2), 819–825. https://doi.org/10.1002/2015GL067102

Huang, P. Q., Lu, Y. Z., & Zhou, S. Q. (2018). An Objective Method for Determining Ocean Mixed Layer Depth with Applications to WOCE Data. *Journal of Atmospheric and Oceanic Technology*, *35*(3), 441–458. https://doi.org/10.1175/JTECH-D-17-0104.1

Huang, S., Tang, L., Hupy, J. P., Wang, Y., & Shao, G. (2021). A commentary review on the use of normalized difference vegetation index (NDVI) in the era of popular remote sensing. *Journal of Forestry Research*, *32*(1), 1–6. https://doi.org/10.1007/S11676-020-01155-1/FIGURES/2

Huete, A. R. (2004). Remote sensing for environmental monitoring. *Environmental Monitoring and Characterization*, 183–206. https://doi.org/10.1016/B978-012064477-3/50013-8

Hund, S. v., Allen, D. M., Morillas, L., & Johnson, M. S. (2018). Groundwater recharge indicator as tool for decision makers to increase socio-hydrological resilience to seasonal drought. *Journal of Hydrology*, *563*, 1119–1134. https://doi.org/10.1016/j.jhydrol.2018.05.069

IICA. (2001). *Desastres en Centroamérica: perspectiva sectorial agropecuaria*. IICA Biblioteca Venezuela. https://books.google.co.cr/books?id=Yb4qAAAAYAAJ

Imbach, P., Beardsley, M., Bouroncle, C., Medellin, C., Läderach, P., Hidalgo, H., Alfaro, E., van Etten, J., Allan, R., Hemming, D., Stone, R., Hannah, L., & Donatti, C. I. (2017). *Climate change, ecosystems and smallholder agriculture in Central America: an introduction to the special issue*. https://doi.org/10.1007/s10584-017-1920-5

IMN. (n.d.). *EL ENOS OCEÁNICO-ATMOSFÉRICO COMO EVENTO PERIÓDICO*.

Jiménez, M., Otero Justo, M. R., Salazar, E., Witkowski, K., & Chavarría Miranda, H. (2016). El fenómeno de El Niño en la agricultura de las Américas. *El Fenómeno de El Niño En La Agricultura de Las Américas. Boletín Técnico*.

Kane, R. P. (1999). Some characteristics and precipitation effects of the El Niño of 1997–1998. *Journal of Atmospheric and Solar-Terrestrial Physics*, *61*(18), 1325–1346. https://doi.org/10.1016/S1364-6826(99)00087-5

Lizano, O. (2014). Las mareas extraordinarias de 1997 en la costa Pacífica de Costa Rica. *Tópicos Meteorológicos y Oceanográficos*, *4*(2), 169–179. https://www.researchgate.net/publication/239699516

Lizano S, J. R. (1991). Aspectos tecnicos sobre cuarenta y cinco cultivos agricolas de Costa Rica. In *Ministerio de Agricultura y Ganaderia*.

Lyon, B. (2004). The strength of El Niño and the spatial extent of tropical drought. *Geophysical Research Letters*, *31*(21), 21204. https://doi.org/10.1029/2004GL020901

Magaña, V., Amador, J. A., & Medina, S. (1999). The Midsummer Drought over Mexico and Central America. *Journal of Climate*, *12*(6), 1577–1588. https://doi.org/10.1175/1520-0442(1999)012<1577:TMDOMA>2.0.CO;2

Magaña, V. O., Pérez, J. B., Vázquez, J. L., & Pérez, J. L. (2003). Impact of El Niño on precipitation in Mexico. *Geofísica Internacional*, *42*(3), 313–330. https://www.redalyc.org/articulo.oa?id=56842304

Markham, B. L., Storey, J. C., Williams, D. L., & Irons, J. R. (2004). Landsat sensor performance: History and current status. *IEEE Transactions on Geoscience and Remote Sensing*, *42*(12), 2691–2694. https://doi.org/10.1109/TGRS.2004.840720

McGregor, G. R., & Ebi, K. (2018). *El Niño Southern Oscillation (ENSO) and Health: An Overview for Climate and Health Researchers*. https://doi.org/10.3390/atmos9070282

McPhaden, M. J., Santoso, A., & Cai, W. (2020). *Introduction to El Niño Southern Oscillation in a Changing Climate*. 1–19. https://doi.org/10.1002/9781119548164.CH1

Moraga Peralta, J. C. (2010). Evaluacion del riesgo ante incendios forestales en la cuenca del Rio Tempisque, Costa Rica. *Revista Geográfica de América Central*, *2*(45), 33–64. https://www.redalyc.org/articulo.oa?id=451744669002

Morillas, L., Hund, S. v., & Johnson, M. S. (2019). Water Use Dynamics in Double Cropping of Rainfed Upland Rice and Irrigated Melons Produced Under Drought-Prone Tropical Conditions. *Water Resources Research*, *55*(5), 4110–4127. https://doi.org/10.1029/2018WR023757

NASA. (2016). *El Niño: 1997-1998 vs. 2015-2016*. https://sealevel.jpl.nasa.gov/data/el-nino-la-nina-watch-and-pdo/el-nino-2015/

Pascale, S., Kapnick, S. B., Delworth, T. L., Hidalgo, H. G., & Cooke, W. F. (2021). Natural variability vs forced signal in the 2015–2019 Central American drought. *Climatic Change*, *168*(3–4), 1–21. https://doi.org/10.1007/S10584-021-03228-4/FIGURES/9

Rembold, F., … H. K.-J. R., & 2016, undefined. (2016). Impact of El Niño on agriculture in Southern Africa for the 2015/2016 main season. *Publications.Jrc.Ec.Europa.Eu*. https://doi.org/10.2788/9743

Retana, J. A. (1999). Posibles efectos de la fase calida de El Niño Oscilacion Sur (ENOS) en la agricultura de Costa Rica. Un analis cualitativo de las estadisticas de produccion agropecuarias. *CNE (Comision Nacional de Emergencias)*.

Retana, J., Solera, M., Solano, J., & Alvarez, H. (1999). Efecto de la variabilidad climatica sobre la fluctuacion poblacional de la rata cañera (Sigmodon hispidus) en Cañas, Guanacaste. *IMN*. https://www.imn.ac.cr/documents/10179/20917/Variabilidad+clim%C3%A1tica+y+ratas+en+Costa+Rica.pdf

Scaramuzza, P., & Barsi, J. (2005). Landsat 7 scan line corrector-off gap-filled product development. *Proceeding of Pecora*, *16*, 23–27.

Schmid, J. N. (2017). *Using Google Earth Engine for Landsat NDVI time series analysis to indicate the present status of forest stands*. https://doi.org/10.13140/RG.2.2.34134.14402/6

Slyunyaev, N. N., Ilin, N. v., Mareev, E. A., & Price, C. G. (2021). The global electric circuit land–ocean response to the El Niño—Southern Oscillation. *Atmospheric Research*, *260*. https://doi.org/10.1016/J.ATMOSRES.2021.105626

Stan, K., & Sanchez-Azofeifa, A. (2019). Deforestation and secondary growth in Costa Rica along the path of development. *Regional Environmental Change*, *19*(2), 587–597. https://doi.org/10.1007/S10113-018-1432-5/FIGURES/7

Tapia Arenas, C. A. (2016). *Análisis del cambio de cobertura forestal 2005-2015 en Guanacaste, Costa Rica*. Instituto Tecnologico de Costa Rica.

Timmermann, A., An, S.-I., Kug, J.-S., Jin, F.-F., Cai, W., Capotondi, A., Cobb, K. M., Lengaigne, M., Mcphaden, M. J., Stuecker, M. F., Stein, K., Wittenberg, A. T., Yun, K.-S., Bayr, T., Chen, H.-C., Chikamoto, Y., Dewitte, B., Dommenget, D., Grothe, P., … Zhang, X. (2018). *El Niño-Southern Oscillation complexity*. https://doi.org/10.1038/s41586-018-0252-6

United Nations. (1998). *El Fenómeno El Niño en Costa Rica durante 1997-1998*.

Vallejos Vásquez, S., Esquivel Valverde, L., & Hidalgo Madrigal, M. (2012). Historico de desastres en Costa Rica (Febrero 1723 - Septiembre 2012). *CNE*.

Waylen, P. R., Quesada, M. E., & Caviedes, C. N. (1996). Temporal and spatial variability of precipitation in Costa Rica anf the Southern Oscillation. *International Journal of Climatology*, *16*(2), 173–193. https://doi.org/https://doi.org/10.1002/(SICI)1097-0088(199602)16:2<173::AID-JOC12>3.0.CO;2-R

Weiss, M., Jacob, F., & Duveiller, G. (2020). Remote sensing for agricultural applications: A meta-review. *Remote Sensing of Environment*, *236*, 111402. https://doi.org/10.1016/J.RSE.2019.111402

Wen, N., Li, L., & Luo, J. J. (2020). Direct impacts of different types of El Niño in developing summer on East Asian precipitation. *Climate Dynamics*, *55*(5–6), 1087–1104. https://doi.org/10.1007/S00382-020-05315-1/FIGURES/8

Wulder, M. A., Loveland, T. R., Roy, D. P., Crawford, C. J., Masek, J. G., Woodcock, C. E., Allen, R. G., Anderson, M. C., Belward, A. S., Cohen, W. B., Dwyer, J., Erb, A., Gao, F., Griffiths, P., Helder, D., Hermosilla, T., Hipple, J. D., Hostert, P., Hughes, M. J., … Zhu, Z. (2019). Current status of Landsat program, science, and applications. *Remote Sensing of Environment*, *225*, 127–147. https://doi.org/10.1016/J.RSE.2019.02.015

Yang, S., Li, Z., Yu, J. Y., Hu, X., Dong, W., & He, S. (2018). El Niño–Southern Oscillation and its impact in the changing climate. *National Science Review*, *5*(6), 840–857. https://doi.org/10.1093/NSR/NWY046

Yu, J. Y., & Kim, S. T. (2013). Identifying the types of major El Niño events since 1870. *International Journal of Climatology*, *33*(8), 2105–2112. https://doi.org/10.1002/JOC.3575